Experimental investigation of microchannel flow boiling heat transfer with non-uniform circumferential heat flux at various gravitational orientations

Marius Vermaak

UP student number: u13047541

Study Leaders:

Prof Jaco Dirker, Prof Josua P. Meyer and Prof Khellil Sefiane

Submitted to fulfil the requirements for the degree

MASTER OF ENGINEERING

in the

Department of Mechanical and Aeronautical Engineering

Faculty of Engineering, Built Environment and Information Technology

University of Pretoria

December 2020

UNIVERSITEIT VAN PRETORIA
UNIVERSITY OF PRETORIA
YUNIBESITHI YA PRETORIA

Acknowledgements

This project received funding from the European Union's Horizon 2020 research and innovation program under the Marie Skłodowska-Curie grant agreement No. 778104. A big thank you must be given to Prof Meyer for offering me the opportunity to conduct my experimental research at the University of Edinburgh for many months.

Dr Valluri and Prof Sefiane gave me the all the support I needed during my time in the experimental laboratory at the University of Edinburgh helping to make the experience one worth remembering.

Prof Dirker, thank you for all the patient support which ensured that I would complete research at the highest level. It would not have been possible without you.

Abstract

Flow boiling of Perfluorohexane (FC-72) in rectangular microchannels with one-sided uniform heating was studied experimentally at different rotations (θ). Various rotational orientations were investigated ranging from θ = 0° (bottom-heating) to 90° (side-heating) in increments of 30° as well as 180° (top-heating).

The channels had a relatively high aspect ratio of 10 (5 mm x 0.5 mm), a hydraulic diameter of 909 μm and a heated length of approximately 78 mm. Mass fluxes of 10 kg/m^{2}s, 20 kg/m^{2}s and 40 kg/m^{2}s were considered at several heat flux values at a saturation temperature of 56°C. For these conditions, in-channel flow visualisations and heated surface temperature distributions were recorded; fluid temperature and pressure readings were taken, and heat transfer coefficients were determined from subcooled conditions, through the onset of nucleate boiling, to near dryout conditions within the channel.

A channel at a rotation of θ = 0° produced the optimal results. θ = 0° had the highest heat transfer coefficient at all mass flux and heat flux combinations tested and had the lowest cross-sectional temperature variation of all rotations, minimizing the probability of warping electronic components. θ = 0° was nucleate boiling dominated resulting in an improved heat transfer performance with an increase in heat flux. θ = 180° experienced heat transfer coefficients that were greater than θ = 30°, 60° and 90° at various qualities up to χ = 0.3 where the vapour slug became confined the heat transfer coefficient decreased rapidly. θ = 90° had the lowest heat transfer coefficients at most mass flux and heat flux test cases. θ = 0° had the highest pressure drop while θ = 180° had the lowest pressure drop.

Contents

List of figures

List of tables

Nomenclature

Symbol	Description	SI Unit
A	Area	m^2
A_c	Cross sectional area	M^2
AR	Aspect ratio	Dimensionless
b_i	Bias of measurement equipment	Dimensionless
Bi	Biot number	Dimensionless
Bd	Bond number	Dimensionless
c_p	Specific heat capacity	J/kgK
Co	Confinement number	Dimensionless
C	Coefficient	
d_h	Hydraulic diameter	m
g	Gravity	m/s
G	Mass flux	kg/m^2s
h_{fg}	Latent heat of vaporisation	J/kg
H	Height of flow passage	m
I	Electric current	A (ampere)
k	Thermal conductivity	W/mK
l	Length of microchannel	m
l_h	Heated length of microchannel	m
l_{cap}	Capillary length	Dimensionless
$\dot{m}$	Mass flow rate	Kg/s
m	Exponential coefficient	
n	Exponential coefficient	
p_i	Random variability in measurement equipment	Dimensionless
$\dot{q}$	Heat flux	W/m^2
$\dot{Q}$	Heat input rate	W
t_w	Wall thickness	m
t	Time parameter	s
T	Temperature	°C
U	Voltage	Volts
$\dot{V}$	Volumetric flow rate	m^3/s
W	Width of flow passage	m
x	Location on the x axis	m

Greek letters

Symbols	Description	SI Unit
α	Heat transfer coefficient	W/m^2K
β_{th}	Coefficient of thermal expansion	K^{-1}
δx_i	Total error of measurement equipment	Dimensionless
ϵ_i	Absolute error of measurement i	Variable
θ	Rotational angle	degrees
μ	Dynamic viscosity	kg/ms
ρ	Density	kg/m^3
σ	Surface tension	N/m
σ_i	Relative error of measurement i	Variable
χ	Thermodynamic vapour quality	dimensionless

Subscripts

Subscripts	Description
ap	applied
ave	average
b	Bulk fluid condition
crit	critical
env	Environmental
in	inlet
IR	Infrared measurement
out	outlet
lenient	Lenient condition
l	Liquid-phase
loss	Leaving the system
m	Measured parameter
max	Maximum
min	Minimum
net	Net total amount
s	Surface
sat	Saturation condition
strict	Strict condition
v	Vapour-phase
z	Distance from inlet to current position

1. Introduction

Flow boiling is an important heat transfer technique in several applications for thermal cooling or heat absorption. Fluid undergoing phase change with bulk fluid motion is called flow boiling. Flow boiling is associated with high convective heat transfer coefficients, defined as the surface heat flux per temperature difference between the surface and the passing fluid. When a boiling fluid is chemically pure, flow boiling occurs at an almost constant temperature called a saturated temperature. A constant saturation temperature and high heat transfer coefficients render flow boiling an attractive cooling method at various length scales. For instance, at small length scales, it is useful for the thermal management of high power-density micro-electronic components, especially when utilised with microchannels. At larger length scales, the high latent heat of vaporisation renders flow boiling important in thermodynamic power and refrigeration cycles.

Efficient heat transfer is crucial at all length scales from small to large length. Improved heat transfer allows for further miniaturisation of electronic circuitry, while enhanced heat transfer sustains efficient thermodynamic conversion systems. Microchannel use offers the advantage of increased heat transfer surface area per flow passage cross-sectional area in addition to better matching geometric scales for electronic cooling. Microchannels are a structure with a hollow core through which fluid flows, typically constructed of metal for industrial applications and borosilicate for experimental investigations. The hollow core of a microchannel has a small cross-sectional area which results in peculiar influences on the flow boiling process because of the interaction between the passing liquid and vapour fluid states with a stationary wall.

The distribution of the vapour and liquid-phases within a channel directly impact the heat transfer mechanism. For instance, in the liquid regions, convection and/or conduction heat transfer are prevalent, whereas in the vapour regions, convection heat transfer is prevalent. The dynamic distribution of the phases and velocity fields also strongly affect fluid mixing and the resulting local ability of the fluid to absorb heat. The phase distribution is generally described with the aid of flow patterns, which qualitatively categorise the visual appearance of the flow into different regimes. For microchannels, these regimes include (for instance):

- bubbly flow, where small amounts of vapour are evenly dispersed or suspended in the liquid
- slug flow, where the vapour has a bullet profile as it passes through the flow channel
- churn flow, where large vapour columns collapse with portions of turbulent flow interaction between the liquid and vapour

- annular flow, where the vapour is present only at the inner regions of the channel and a liquid layer is present at the periphery.

Optimal convective heat transfer occurs when the wall of the channel, that acts as the heat transfer surface, is in contact with liquid. Dryout is associated with operating conditions where all the liquid in a particular region of the channel has been evaporated. Dryout is not attractive due to a substantial reduction of the local heat transfer coefficient and the accompanying large temperature difference between the wall and the heat transfer fluid. In addition, heat transfer is no longer sustained at the relatively constant saturation temperature. In the case of electronic cooling, this results in local over-heating to significantly above the saturation temperature, depending on the local heat flux and heat transfer coefficient. In the case of thermodynamic cycles, unless superheating of the fluid into a gas is required, this operating state is also unattractive because of the associated relatively poor heat transfer coefficient.

Heat flux is defined as the total amount of heat absorbed by the fluid per unit area. It directly affects the heat transfer coefficient in some channels. Channels with many small bubbles moving away from the point at which they form (the nucleation site) can increase in size faster at higher heat fluxes, producing relatively large secondary vapour motion, which can directly increase the heat transfer coefficient. Secondary flow effects are well documented in large-scale channels but are less understood in small-scale channels due to confinement effects. This gap in knowledge is knowing which orientation best leverages secondary fluid motion for increased heat transfer performance.

The gravitational orientation of the channel also strongly affects the steady state settling position of the vapour-phase in a two-phase fluid. The orientation can alter the thickness of the liquid layer at the channel circumference, which may result in early localised dryout in the vapour-phase and improved heat transfer in the liquid-phase. This buoyancy-driven affect can be leveraged to improve heat transfer by removing vapour – which generally has a lower heat transfer coefficient than liquid – from the heated surface and replacing it with liquid.

Channels with small-length scales typically have bubble-wall interactions, known as confinement effects, that directly affect the heat transfer performance of the fluid. Channel orientation can allow the vapour to move to portions of the channel where it is less likely to cause dryout. For instance, bottom-heated channels have vapour located on the top wall of the channel, and the vapour only

affects the heated wall when the proportion of vapour in the channel is large. Small-length scales also experience temporal variability in the steady state vapour location.

Optimally orientated systems would be associated with flow conditions that are relatively constant in time or have predictable and favourable temporal instability. In general, temporal instability can exhibit as pressure and density wave oscillations that change the operating flow state from its steady condition; this in turn may temporarily reduce or improve the heat transfer performance.

Gravitational orientation can be altered by rotating the channel about the flow direction. This is particularly interesting when the aspect ratio (width-to-height ratio) of a channel is large and the channel has non-uniform circumferential heating. However, little is known about extent to which high-aspect ratio channels have their heat transfer coefficients impacted by rotation about the flow direction, especially between heating from above and below.

Microelectronics often experience one-sided heating as they are directly attached to the heated surface. The width of the channel is the width of the electronic component while (to save space) the height is minimised. Studies investigating the difference between microchannels orientated horizontally and heated from above or below have shown that buoyancy effects in the channel can produce increases in the local heat transfer coefficient.

Channels at low mass flow rates heated on one side are often investigated in isolated orientations, such as horizontal or vertical. Liquid vapour interactions could be leveraged to increase the heat transfer coefficient by using the buoyancy of the heated liquid and vapour to create secondary fluid motion through the colder fluid. High aspect ratio rectangular channels could also be used to increase the buoyancy effects by allowing the vapour to move farther in the cross-sectional direction than circular or square channels allow. FC-72 is a refrigerant with a saturation temperature below the operating temperature of many electronic components. Little data exists on heat transfer coefficient of FC-72 in low mass flow rate, high aspect ratio microchannels that are heated from one-sided.

1.1 Problem statement

Few experimental investigations have considered the effects of gravitational orientation on the heat transfer coefficient in a non-uniformly heated high aspect ratio microchannel. Rotational effects allow for vapour motion in the cross-sectional direction. In a few studies, the analysis of heat transfer

coefficients to define optimal channel orientation have considered rotations such as top and bottom heated. This study focuses on closing the gap in knowledge regarding a high aspect ratio channel that is heated from one side at various gravitational orientations about the flow direction (rotations).

1.2 Aims and objectives

1. Modify an existing experimental flow boiling test facility at the University of Edinburgh. The purpose here is to enable testing at different rotational orientations.
2. Conduct experiments at varying test-section rotational orientations. The purpose is to find the orientation that produces the optimal heat transfer performance at different combinations of mass flux and heat flux.
3. Analyse the data and
4. Calculate heat transfer coefficients
5. Interpret the surface temperature results
6. Determine which channel rotation optimizes cooling

1.3 Dissertation outline

Chapter 2 contains a literature review of flow boiling and experimental studies of heat transfer and pressure drop in microchannels.

Chapter 3 details the experimental setup used in this study; the focus is on investigating the rotational effects during flow boiling.

Chapter 4 describes the sensor calibration procedures, test matrix and the experimental procedure.

Chapter 5 provides details about the data reduction method for the heat transfer coefficient and pressure drop calculations.

Chapter 6 presents heat transfer coefficient results indicating the effect of channel rotation, heat flux and mass flux.

Finally, Chapter 7 concludes the study.

2. Literature review

This chapter reviews the prior research on flow boiling. The use of flow boiling in microelectronic cooling applications is described. Typical bubble behaviours observed during flow boiling used for electronic cooling applications are discussed. The standard terms are defined, and the concepts of microchannel, minichannel and microchannel transition criteria are described. Flow boiling is discussed in relation to typical flow patterns, and their impact on heat transfer is presented. Methods of enhancing the heat transfer in microchannels are considered. Orientational changes in terms of channel rotation and inclination are described, and the choice of fluids used in experimental studies is discussed. Flow instability is briefly discussed due to its impact on the time averaged heat transfer coefficients presented later in this study. The chapter concludes with the gap in the literature highlighted and the focus of the study defined.

2.1 Flow boiling in electronic cooling

Subcooled flow boiling is the process by which liquid in motion is heated from a single-phase to a two-phase state. While in the single-phase state, the fluid is referred to as being subcooled, with the liquid's temperature below the saturation temperature (T_{sat}). As the fluid is heated, its temperature increases until it reaches saturation temperature, where it remains until all the liquid has turned to vapour.

Flow boiling is observed to have begun once bubbles start to form, known as the onset of nucleate boiling [1]. Nucleate boiling has two distinct regions, namely partially developed boiling and fully developed boiling [1]. During partially developed boiling, vapour bubbles collapse because of the significant sub-saturation temperature of the surrounding liquid. During fully developed boiling, the surrounding liquid temperature has increased sufficiently (due to convective heat transfer and mixing) to sustain stable bubble growth. Once bubbles start to coalesce, saturated boiling has commenced.

Flow boiling is used extensively in cooling applications because the fluid can continue to absorb energy while the liquid in the channel evaporates yet remains at the saturation temperature. Electronic components are small-scale applications where flow boiling is used as a cooling mechanism. Electronic components utilise constant saturation temperatures during saturated boiling to stay below optimal operating temperatures [2].

The need for fast computing has led to the development of electronic components that are both small and produce substantial heat, which in turn necessitates removing high power densities from the heated surface [3-8]. This cooling challenge has been met utilising single- or multiple-channel systems in conjunction with flow boiling [2]. Single-channel systems benefit from minimal flow maldistributions issues and low total pressure drop, whereas multi-channel systems benefit from larger fluid-to-heated-surface area ratios, helping to increase the heat transfer rate.

Multi-channel systems are generally referred to as a heat sink. These systems utilise single-phase cooling [9-12], micro-jet cooling [13], multi-phase cooling [14], thermo-electric cooling [15], phase-change materials [8], electro-osmotic flow [16] and nanofluids [17-19] to increase heat transfer, depending on the application. Nanofluids, for example, can increase the heat transfer by up to 40% [20].

Refrigerants utilise low saturation temperatures to maintain electronic components at their optimal operating temperature, which is often below 100°C [21, 22]. Refrigerants are needed because water cannot utilise the benefits of flow boiling at temperatures below 100°C without significant pressure controls to decrease the saturation temperature.

A second challenge facing electronic cooling is that electronics often produce a non-uniform heat flux distribution on the heated surface, resulting in hotspots [2]. Hotspots can have heat fluxes of up to eight times higher than other locations on the heated surface [23, 24]. These hotspots result from integrated circuits created for multi-core processors [8]. Multi-channel systems are more susceptible than single-channel systems to experience dangerously high surface temperatures because of hotspots, as heat cannot be transferred as effectively in the cross-sectional direction.

2.2 Terminology

A channel can be defined as a hollow flow passage surrounded by a solid wall. To enable the comparison of flow passages which have different geometries, the fluid mass flow rate ($\dot{m}$) passing through the channel with a particular cross-sectional flow area (A_c) can be rewritten as a mass flux ($G = \dot{m}/A_c$). Single-phase flow can be categorised according to the flow regime, with the velocity profiles typically used to describe the type of flow regime.

The flow regime experienced is often predicted using a non-dimensional number known as the Reynolds number (Re) which is a ratio of inertial forces to viscous forces. The Reynolds number considers the fluid's properties such as density, velocity, and viscosity as well as the geometry of the flow passage. Reynolds number ranges have been created from experimental investigations which correspond to the flow regime that can be expected.

A circular channel can be used as an example. Here, a velocity profile with a maximum in the centre of the channel and a minimum at the wall, with a parabolic profile in a cross-section, is known as laminar flow. Laminar flow is typically found at mass flow rates resulting from lower Reynolds numbers (Re below 2300). At high mass flow rates (Reynolds numbers above 4000), the flow profile is chaotic, with a relatively flat velocity profile with large flow velocities in the tangential flow direction; this flow regime is turbulent flow. Between Reynolds number of 2300 and 4000, the flow alternates between uniform and chaotic velocity profiles at the same mass flow rate; this is a transitional flow regime.

Heating the channel results in a temperature profile in a flow cross-section that is the same as for velocity at each regime discussed above. The rate at which the heat is transferred is referred to as the heat transfer rate ($\dot{Q}$). This rate is often converted to heat flux ($\dot{q} = \dot{Q}/A_s$), which utilises the total heated surface area across which heating occurs (A_s) to allow for comparison between surfaces irrespective of their shape or size. In systems which lose heat to the environment, the heat transfer rate and heat flux referred to are typically the net heat transfer (after heat loss has been considered).

Internal forced convection is a heat transfer mechanism which produces a temperature profile in a fluid's internal cross-section. Single-phase laminar flows have temperature gradients starting at the heated wall because of the uniform velocity profile and heat transfer between the liquid layers. Turbulent single-phase flows as well as two-phase flows sometimes have heat transfer between fluid layers as well as mass transfer due to buoyant fluid rising through cooler and less buoyant fluid which can act to enhance the heat transfer rate ad decrease the thermal gradient. A more even temperature profile is found in the cross-sectional direction.

The rate at which this heat transfer occurs is calculated as a heat transfer coefficient (α), defined as the heat flux per degree difference between the diabatic (heat transfer) wall temperature and the reference fluid temperature. The thermodynamic bulk fluid temperature is commonly defined as the average fluid temperature in a cross section. The magnitude of the heat transfer coefficient depends

on several features or aspects; these features include the channel geometry, the fluid properties, flow regime and heat flux.

Internal forced convection has two main flow boiling mechanisms that directly affect the heat transfer coefficient: nucleate boiling and forced convection with evaporation. Nucleate boiling is a boiling mechanism in which the surface temperature is above the saturation temperature, but a large portion of the heated wall has liquid in contact with it. Nucleate boiling typically sees the formation of bubbly flow from the nucleation site. Forced convection with evaporation normally lacks small bubbles that form from a nucleation site but rather displays a vapour column with a liquid film surrounding the vapour.

Two-phase flow occurs once the bulk fluid temperature has reached saturation conditions and a combination of vapour and liquid is found in a cross-section. Subcooled flow boiling refers to boiling that starts below the saturation temperature. During flow boiling, the ratio of liquid to vapour in a cross-section directly affects the heat transfer rate and flow regime.

Thermodynamic vapour quality (χ) is the mass ratio of liquid and vapour in a cross-section. A vapour quality below 0 (negative) indicates that the system is subcooled. Vapour qualities between 0 and 1 indicate that the fluid has reached the saturation temperature and some of the liquid has changed phase from liquid to vapour. Vapour qualities above 1 indicate that all the liquid has become vapour and the bulk vapour temperature is above the saturation temperature; this is called super-heated vapour. The void fraction is the volume ratio of liquid to vapour in a cross-section. This value is often used in conjunction with thermodynamic vapour quality.

Vapour quality is often determined analytically using a homogenous equilibrium model [25], in which the amount of heat applied and lost to the environment is used to calculate the amount of energy absorbed [26]. This is a mathematical approximation which employs an energy balance with negligible losses ignored. Void fraction is more difficult to predict analytically. It requires the use of correlations based on experimental techniques which can have a mean absolute error as low as 1.8% [27]. The correlations are applicable only to a narrow band of cases [28-31]; hence, void fraction is typically measured directly instead. The experimental methods include gamma ray attenuation [32, 33], valves to instantly isolate the vapour-liquid mixture in a test section [34] and planar laser-induced fluorescence analysis [35]. However, these approaches are difficult to implement. Vapour quality is thus the preferred measure of the liquid-to-vapour ratio in the two-phase region.

During flow boiling, the liquid/vapour interactions can vary greatly depending on mass flux, heat flux, the fluid and channel passage geometry. These interactions result in the distribution of liquid and vapour changing and forming observable patterns of interaction, called flow patterns.

2.3 Flow patterns

Flow patterns or flow regimes describe the interactions of the different layers, phases, and fluids during motion. Each interaction affects the velocity and temperature profile of the fluid in a cross-section. In the single-phase region, the flow regime is directly affected by the mass flow rate. In a circular channel, for example, the velocity profile of a single-phase fluid entering a channel changes depending on the mass flow rate. Cases of low mass flow produce parabolic velocity profiles with rapidly moving fluid in the centre of the channel and the slowest fluid movement at the wall; this pattern is called laminar flow. High mass flow rates produce velocity profiles that are more uniform, with severe mixing due to severe movement of the fluid with large tangential flow velocities. This pattern is called turbulent flow.

The hydrodynamic entrance region is the section of the channel in which the velocity profile changes from uniform to its final form. In the hydrodynamic entrance region, the fluid is developing. The fluid is said to be developed once its velocity profile reaches the parabolic shape or when semi-steady mixing fluid is deemed to have occurred.

The temperature profile in the circular channel example also develops due to heating. A thermal boundary layer forms with the fluid's temperature increasing from the wall to the centre of the channel. Once the boundary layer is so thick that it spans from the heated wall to the centre of the channel, a uniform cross-sectional temperature is found, and the flow is fully developed.

Two-phase flow regimes are more numerous than single-phase flow patterns. The dispersal of the vapour and volume of the vapour greatly affects the heat transfer. The diameter and geometry of a channel can allow other flow patterns to form or prohibit this.

Bubbly flow is characterised by relatively few discrete bubbles distributed over the flow cross-section [36]. Bubbly flow has two forms: dispersed and vigorous. Dispersed bubbly flow is generally found at low vapour qualities when bubbles are relatively distant from each other and are evenly distributed across the entire cross-section. Vigorous bubbly flow occurs when heating is rapid, resulting in many

bubbles forming throughout a cross-section [36]. These bubbles move towards the centre of the channel, increasing the vapour quality and resulting in the formation of a single large bubble, called a slug.

Slug or plug flow develop when the bubbles become confined within the channel. This causes coalescence into large bubbles that almost fill the entire flow passage [29]. The large singular bubbles that span almost the entire length of the channel form the slug. Liquid can penetrate through the slug, breaking it into smaller pockets of vapour, called plugs. As a slug or plug becomes heated, it grows both downstream and upstream in the shape of a bullet, with a curved front and flat rear [37]. At the rear of a slug, the bubble displays small sinusoidal wave shapes in contact with the wall, breaking the thermal and velocity gradients at the wall. The flow pattern typically has a layer of liquid between the vapour and the circumferential walls, which is known as a liquid film.

Churn flow occurs at vapour qualities higher than those at which slug flow occurs. Churn flow displays severe interaction between the liquid and vapour slugs, causing the formation of plugs and bubbly flow. This flow pattern normally occurs at high vapour qualities, mass fluxes and heat fluxes [38]. The flow pattern typically has violent interactions between the liquid film and the internal vapour bubble, with a high degree of mixing.

Stratified flows are typically found in large channels where gravity has a substantial effect on the flow behaviour, particularly when the mass flux is low [39]. In horizontal channels, the liquid pools at the bottom of the channel with the vapour above it. When the shear force on the liquid vapour interface is low, the interface face is horizontal. At low viscosities and high shear forces, the interface can become wavelike in the flow direction, which causes a stratified wavy flow pattern.

Stratified annular flow occurs when the entire perimeter is in contact with liquid (wetted). Although the film thickness might be uniform around the local perimeter, the thickness changes along the axial flow direction with a wavelike profile [40].

Mist flow occurs at high vapour qualities when the liquid film is no longer present and the liquid is transported by the vapour in the form of small bubbles [26]. This flow pattern is associated with extensive dryout on all circumferential wall positions.

As the heating increases, fully annular flow develops, characterised by a liquid film on the entire wetted perimeter of equal thickness in the axial direction. The inner region of the channel carries a jet of superheated vapour with a few entrained droplets [41]. At low mass fluxes, annular flow generally develops from stratified flows, whereas at high mass fluxes it generally develops from churn flows. Typically, annular flow is present in channels that have aspect ratios close to 1, large hydraulic diameters, high mass fluxes and high heat fluxes [42].

Dispersed flow occurs when the liquid surrounding the vapour in annular flow has almost completely disappeared and the system's vapour quality is close to 1, with a few liquid droplets entrained in the vapour [41]. This is followed by complete dryout of the channel.

In channels with large internal diameters, less-dense liquid rises due to heating while dense cold liquid falls because of buoyancy effects. The motion due to density discrepancies is called buoyancy-driven flow. Vapour produced during flow boiling experiences considerable buoyancy-driven motion. The buoyancy force can be so strong that the vapour bounces off the top of the flow passage back into the flow before it settles at the top of the channel. This heat transfer mechanism is known as mixed convection. That is, forced convection occurs due to the enforced bulk fluid motion, whereas free convection occurs due to the buoyancy of the fluid. Buoyancy-driven motion or buoyancy assisted flow is an important consideration for larger channels, but their affects can be negligible is small channels, as is discussed in 2.4.

Mixed convection can occur at various mass fluxes and heat fluxes. It is prevalent at low mass flux and high heat flux combinations when the buoyancy force is stronger than the bulk fluid motion. Mixed convection can occur in single-phase [43] and two-phase flow [44]. Single-phase mixed convections involve the motion of warm liquid through cooler liquid. Two-phase mixed convection results from the motion of vapour moving through the liquid due to a nucleation site below the liquid's surface i.e., at the bottom of a channel.

As mentioned earlier, two-phase flow patterns or flow regimes are affected by various factors. These include mass flux, vapour quality, pressure, channel geometry and the working fluid's properties. Each factor can influence the transition point between flow patterns and which flow patterns are experienced [45].

Flow patterns are grouped into flow pattern maps which depend on the previously mentioned factors. These can be used to predict the type of flow pattern that will be experienced by a fluid at a specified saturation pressure, mass flux and channel geometry for various heat fluxes and thermodynamic vapour quality [46]. These maps are drawn from experimentally obtained flow visualisation during complete flow boiling (χ from 0 to 1) at various mass flux values, while keeping the saturation pressure constant [36, 46-48].

The governing flow pattern greatly affects the heat transfer and pressure-drop characteristics of the fluid flow. Hence, much of the experimental research has focused on identifying the transition points between flow patterns [46, 49, 50]. Many studies have focused on one transition boundary, with the intention of increasing the available data by investigating diverse pressures, mass fluxes and channel geometries [49, 51-53].

2.4 Channel classification

Fluid behaviour in a channel is directly affected by the size of the internal passage. The channel is classified according to three categories: macrochannel, minichannel and microchannel. These are defined by the type of physics a fluid predominately experiences during adiabatic and/or diabatic flow. Macrochannels have an internal flow passage diameter large enough to result in the fluid's behaviour during boiling being dominated by buoyancy effects. Minichannels have smaller flow passages, with the fluid's behaviour being caused by a combination of surface tension and buoyancy effects. Microchannels have the smallest internal flow passage, with the fluid's behaviour during boiling being dominated by surface tension. Small flow passages often are too small for the buoyant heated fluid to move far enough to impact flow behaviour. Heat flux can affect buoyancy effects with low heat flux cases resulting in the heated fluid lacking sufficient force to move through the colder fluid when surface tension is high.

Microchannel physics differ from macrochannel physics in that microchannels experience wall confinement effects that significantly impact bubble behaviour. Confinement effects alter bubble behaviour at the nucleation site, the growth of bubbles, bubble motion after departure and the coalescence of bubbles. Microscale channels have more intense internal fluid and fluid-wall interactions, such as surface tension and capillary forces, which disrupt the formation of thermal stratification [54]. Macrochannels have larger volumes with fewer fluid-wall interactions, allowing for thermal stratification to occur in the fluid. Macrochannels experience bubble confinement at larger

vapour qualities than microscale channels; the vapour slugs, for example, rarely become confined by the channel walls. Macrochannels can experience greater mixed convection due to the larger flow-passage liquid and vapour buoyancy associated with thermal stratification.

The challenge of differentiating between macrochannels, minichannels and microchannels is so poorly defined that often researchers do not consider minichannels as a category. The focus tends to be entirely on determining when buoyancy alone is dominant or when only surface tension is dominant. An elementary method for categorising the channels uses the internal flow diameter. A first-order approximation considers an internal flow passage diameter of less than 1 mm to be the transition point at which macro-scale physics no longer dominate and micro-scale physics start to dominate, in circular horizontal channels [55, 56].

Non-circular channels have an added complication, namely the effect of their cross-sectional shape. The hydraulic diameter (d_h) is defined as the ratio of four times the cross-sectional area to the wetted perimeter. Non-dimensionless numbers (such as the Reynolds number) cannot consider channels with a non-circular geometry directly; hence, the hydraulic diameter creates a diameter for the non-circular channel as if it were circular.

Kandlikar [57] defined the channel categories in terms of hydraulic diameter. A microchannel was defined as $d_h < 0.2\ mm$, a minichannel as $0.2\ mm < d_h < 3\ mm$ and a macrochannel as $3\ mm < d_h$. Many authors have investigated this transition in hydraulic diameters larger than 3 mm, showing that the mass flux [58], saturation pressure [59] and heat flux [60, 61] all play a role.

The hydraulic diameter does not, however, consider the working fluid's properties. Fluids with different surface tensions, for example, could have high buoyancy forces at low hydraulic diameters. Surface tension and buoyancy forces are considered more completely using an array of non-dimensional numbers including the confinement number, capillary length, bond number and Eötvös number.

Kew, et al. [62] developed a non-dimensional number known as the confinement number (Co), shown in equation (1-1). The confinement number is used to determine a ratio of surface tension to buoyancy-driven forces, considering the flow passage geometry as well as fluid properties. This non-dimensional number is used in cases where the fluid is directly heated from the channel's wall [63].

$$Co = \frac{1}{d_h}\sqrt{\frac{\sigma}{g(\rho_l - \rho_v)}} \tag{1-1}$$

The confinement number uses the hydraulic diameter directly in conjunction with surface tension (σ), gravity (g), liquid density (ρ_l) and vapour density (ρ_v). The threshold value for the confinement number is 0.5 [62], with $Co > 0.5$ indicating that microchannel physics are dominant and $Co < 0.5$ indicating that macrochannel physics are dominant. No minichannel region is defined.

Tibiriçá, et al. [64] defined the transition criteria by comparing a channel's hydraulic diameter to a capillary length (l_{cap}), known as a Laplace constant. Equation (1-2) shows that the only difference between the capillary length and confinement number is that the hydraulic diameter is not used in the calculation.

$$l_{cap} = \sqrt{\frac{\sigma}{g(\rho_l - \rho_v)}} \tag{1-2}$$

Li, et al. [65] experimentally investigated the hydraulic diameter that would indicate the dominance of gravitational effects and surface tension effects using the capillary length. A threshold hydraulic diameter ($1.75l_{cap}$) and a critical hydraulic diameter ($0.224l_{cap}$) were used to define the transition diameters. They found that microchannel physics dominated when $d_h/l_{cap} < 0.224$, with surface tension forces dominating the flow behaviour ($Co > 4.46$). Minichannel physics dominated when $1.75 < d_h/l_{cap} < 0.224$ where buoyancy and surface tension forces competed to dominate the flow behaviour ($0.57 < Co < 4.46$). Macrochannel physics dominated when $d_h/l_{cap} > 1.75$, where buoyancy forces dominated ($Co < 0.57$).

The Capillary number is a dimensionless quantity which considers the viscous drag forces and surface tension forces of two immiscible liquid across an interfacial boundary. The Capillary number approach allowed for minichannel physics to be identified, suggesting it may be more useful than the confinement number when two immiscible liquid are present. These two numbers do not tally well with the macrochannel transition criteria, differing by 14% and the microchannel criteria differing by an order of magnitude. Much of the discrepancy might be reduced if the confinement number also categorised minichannels.

Another method for classifying a channel is to use the Bond number (Bo) [66]. Here, the relative importance of buoyancy to surface tension forces is considered [67]:

$$Bo = \left(\frac{d_h}{l_{cap}}\right)^2 = \left(\frac{1}{Co}\right)^2 = \frac{g(\rho_l - \rho_v)d_h^2}{\sigma} \tag{1-3}$$

The bond number indicates expected microchannel behaviour when $Bo < 0.05$ and macrochannel behaviour when $Bo > 3.0$ [68]. Minichannel behaviour is expected when $0.05 < Bd < 3.0$. However, some researchers have suggested that the channel is a microchannel only if $Bo > 4.0$ [62].

Barnea, et al. [69] suggested that a critical bond number (Bo_{crit}) should be based purely on the fluid properties rather than the channel geometry. The bond number could then be compared to the critical value.

$$Bo_{crit} = \left(\frac{p_l}{p_l - p_v} - \frac{\pi}{4}\right)^{-1} \tag{1-4}$$

The critical bond number was determined to be Bo_{crit} = 4.49 for FC-72 at saturation conditions with an atmospheric pressure of 101 kPa. Bond numbers greater than the critical bond number would indicate macrochannel physics and smaller numbers would indicate microchannel physics.

Brauner, et al. [70] suggested yet another criterion to define the transition called the $Eötvös$ number ($Eö$). Often the bond number and Eötvös number can used interchangeably. In some applications the definition may differ slightly. The Eötvös number was specifically developed for adiabatic flow pattern transition in a single channel by comparing the buoyancy forces and surface tension forces. According to this approach, surface tension dominates when $Eö > 1$ [71, 72].

$$Eö = \frac{(2\pi)^2 \sigma}{(\rho_l - \rho_v)\, {d_h}^2 g} \tag{1-5}$$

There is little consensus about when a channel should be defined as a microchannel, minichannel or microchannel, with the first-order approximation of hydraulic diameter being widely used. Channel geometry and fluid properties have been used to define non-dimensionless numbers to create a more accurate approach to the transition between channel physics, but these also lack agreement regarding an exact transition point. The non-dimensional numbers are notably less useful for the minichannel

physics range but can be used to indicate when micro or macro physics would be clear dominating factors.

The heat transfer mechanism is generally considered to be similar among the categories. In this regard, smaller diameter channels experience the same physics as macrochannels, with the added complexity of confinement and surface tension effects.

2.5 Effective heat flux calculations

This study relies on single-phase tests to determine the rate at which heat is lost to the environment as a function of the temperature difference between the heated surface and the environment. This is necessary in the calculation of the effective heat flux, which is the amount of heat absorbed by the fluid per unit area. The effective heat flux is used to calculate the two-phase heat transfer coefficients, and vapour qualities as will be discussed later.

The amount of heat supplied to an experimental setup is often not the amount of heat that reaches the fluid at the interfacial boundary. This is because in experimental investigations some of the heat supplies to the experimental setup is lost the environment.

Surfaces exposed to the environment are subject to heat losses through primarily convection but also radiation and conduction. Natural convection losses are caused by the temperature difference between the exposed heated surface and environmental temperature. The rate is affected by the geometry of the test section and heating components. Radiation losses similarly occur from the exposed heated surfaces to the environment. These losses are affected primarily by the exposed surfaces temperature and emissivity as well as the temperature of the objects in the environment around the heated surface. Conduction losses are typically to other parts of the experimental facility. Conduction and radiation losses are typically considered negligible compared to convection losses.

Experiments using a heating block and cartridge heaters determine the heat losses without the use of empirical correlations [73-77]. With complex geometric setups the test section is cleared of all fluid and heated with various constant heat inputs. The heating is kept at a constant input for as long as an hour so that steady-state temperatures are achieved [78]. Once the temperature of heating block stabilised these temperature measurements as well as the ambient temperature, wall surface

temperature and heat input's voltage and current readings are used to calculate the amount of heat lost.

This heat loss is typically expressed as a function of the wall temperature and the ambient temperature. The form this equation takes varies but is often a linear relationship between the amount of heat lost in watts ($\dot{Q}_{loss}$) and difference between the heating block's temperature (T_s) and the ambient air temperature (T_∞):

$$\dot{Q}_{loss} = 0.1451(T_s - T_\infty) \tag{1-6}$$

Polynomial relationships can also be found [77]. Alternatively, the experimental facility can be insulated to minimize the amount of heat lost to the environment [79]. The thermal insulation cannot often be used in microchannel or heat sink studies as the bubble dynamics are of interest and need to be recorded through a viewing panel with a high-speed camera.

Alternative experimental setups do not use large cartridge heaters to supply heating but rather use a thin layer of metal like indium tin oxide (ITO) or tantalum (Ta) with a voltage potential across the metal. These experimental setups cannot have tests conducted without the use of a fluid running through the test section as the metal layers can burn out.

Heat losses can sometimes be predicted using empirical correlations to predict the heat losses from the heated surface. This possible when the geometries are standard and the boundary condition is either a uniform heat flux or isothermal surface temperature [80, 81]. Heat transfer textbooks often have summarised empirically derived equations for these calculations. The natural convection Nusselt numbers can be obtained from test sections that have circular, elliptical, triangular, square and rectangular cross-sectional shapes [82]. The Nusselt number for natural convection is typically represented in the following form:

$$Nu = CRa^m \tag{1-7}$$

The Nusselt number (Nu) is typically represented as a function of the Rayleigh number (Ra) with the coefficients "C" and "m" dependent on a number of different parameters [83]. The Rayleigh number is a dimensionless number calculated from the Grashof number (Gr) and the Prandtl number (Pr). The Grashof number is the ratio of the fluid's buoyancy and viscosity while the Prandtl number is a

ratio of the momentum and thermal diffusivity of the fluid. All three these non-dimensional numbers are presented below:

$$Ra = Gr \cdot Pr \tag{1-8}$$

$$Gr = \frac{g\beta(T_s - T_\infty)L_c^3}{v^2} \tag{1-9}$$

$$Pr = \frac{v}{\alpha} = \frac{c_p \mu}{k} \tag{1-10}$$

The Grashof number in equation (1-9) is calculated using gravity (g), coefficient of thermal expansion (β), the surface temperature (T_s), the atmospheric temperature (T_∞), a characteristic length (L_c) and the kinematic viscosity (v). The Prandtl number is calculated the kinematic viscosity and the thermal diffusivity (α) or alternatively using the specific heat (c_p), the absolute viscosity (μ) and thermal conductivity (k).

The Nusselt number is thus affected by the fluid properties of the fluid through which natural convection occurs. In many natural convection, heat loss cases, this is air. Nusselt numbers are categorised broadly by the heating boundary condition, namely a specified heat flux or specified surface temperature. Nusselt number correlations are only applicable if several criteria are met. These criteria include the heated surface's geometry, uniform versus non-uniform heating, the heated surface's orientation relative to gravity, the Prandtl number at the heated surface, and the Grashof number at the heated surface [84, 85].

Channel geometry can affect the heat transfer due to surface area available for heat transfer as well as the ease with which heat can leave a heated surface. A heat sink typically has a much higher surface area for heat transfer but may have a lower Nusselt number due to the proximity of the heated fins distance from each other [82].

The orientation of a surface can have a substantial effect on the rate at which heat is transferred away from the surface. This is typically due to how easily heat can move away from the surface. A horizontal plate heated from below often has the problem where the heated more buoyant air cannot move away from the heated surface as a horizontal heated from above plate. These orientations are investigated separately in experimental investigations with Nusselt numbers created for each case [82].

Nusselt number is only applicable to a range of Prandtl number and the Grashof number values which are either specified individually or through a Rayleigh number range. The Rayleigh number can be used to determine the flow regime on the heated surface with an increase in the Rayleigh number typically resulting in an increase in the Nusselt number and the use of a different correlation [84]. Each Rayleigh number case typically results in different coefficients being chosen "C" and "m" [85].

Natural convection Nusselt numbers typically consider uniform boundary conditions such a uniform heat flux or isothermal temperature on the entire surface. This is because most real-world applications have uniform boundary conditions. Non-uniform conditions are typically investigated at constant surface temperature with the assumption that all heating from other surfaces is either negligible or can be calculated separated and then added together. An example would be a flat plate at an isothermal condition heated from below or above. The resultant total Nusselt number would be calculated using the bottom heated case and top heated case's Nusselt number.

$$Nu_{total} = 0.27Ra^{\frac{1}{4}} + 0.59Ra^{\frac{1}{4}} \quad (1\text{-}11)$$

The total Nusselt number in equation (1-11) is calculated using the Nusselt number for a bottom heated and top heated isothermal plate, which is applicable at Rayleigh numbers ranging from 10^5-10^{11} and 10^4-10^7 respectively [82].

Inclined plates similarly have Nusselt numbers available for isothermal plates at an angle from 0° to 60°. In this calculation the Grashof number is calculated at the inclination by replacing the gravity term "g" with "$gcos\theta$" where "θ" is the angle between the horizontal position and the inclined position.

Using these Nusselt numbers to calculate the total heat transfer from the test section, several assumptions are required. The most important one to consider is that the Nusselt number only accounts for losses under the specified conditions previously mentioned. Secondly, the Nusselt number is correct despite reviews of Nusselt numbers suggesting errors as high as 40.25% is possible[86]. Thirdly, other losses due to conduction and radiation may need to be considered to find the total heat loss from the surface.

Non-uniform heating is an important consideration when choosing a Nusselt as at a range of Rayleigh numbers the Nusselt number can differ by up to 20% [87]. Non-uniform heating conditions are very rarely investigated for flat plates. When non-uniform conditions are investigated it is typically for non-

uniform surface temperature due to heating pipes at various position underneath a cover plate rather than a non-uniform heat flux.

2.6 Single-phase heat transfer coefficient

In the absence of an appropriate empirical heat loss correlation the single-phase results could be verified using empirical internal forced convection Nusselt numbers. Internal forced convection occurs inside a heated enclosure due bulk fluid motion in contact with a heated surface. The average Nusselt number used for internal forced convection generally comes in the form shown in equation (1-12) although a modified version is shown in equation (1-13).

$$Nu = CRe^{m}Pr^{n} \quad (1\text{-}12)$$

$$Nu = f \cdot CRe^{m}Pr^{n} \quad (1\text{-}13)$$

Equation (1-12) represents the Nusselt number as a function of the Reynolds number, Prandtl number with two exponential coefficients “m” and “n” as well as the coefficient “C” [88]. In some studies, this Nusselt number calculation also considers the friction factor (f) [89]. Friction factors is an important consideration as it is Reynolds number dependent and can be used to identify a change from laminar to transitional flow and transitional flow to turbulent flow. It will not be further discussed as most correlations do not explicitly account for the friction factor separately from the coefficient “C”.

The flow regime is associated with the Reynolds number is an important factor to consider when selecting an appropriate Nusselt number equation. It is widely expected that developed laminar flow Nusselt number remains approximately constant in the laminar flow regime [90]. Vertical circular pipes typically have a Nusselt number of 4.36 when a uniform heat flux is applied to the outside of the pipe with water moving through it [91]. The typically used value of 4.36 can be effected by the Grashof with an increase resulting in an increase the Nusselt number [92]. This increase is attributed to mixed convection effects resulting in buoyancy driven motion.

Laminar flow in channels must develop before it reaches the fully developed flow value. This region between the inlet and the point at which the flow is developed is called the developing region. The Nusselt number is typically higher in the developing region than in the developed region [91]. The entry length for hydrodynamically and thermally developing flow is typically calculated as function of the Reynolds number, Prandtl number and the diameter of the circular channel. This correlation used

is Reynolds number dependent with Durst, et al. [93] suggesting that at a Reynolds number between 1 and 100 the following equation should be used for a uniformly heated vertical circular channel:

$$L = (0.619^{1.6} + (0.0567Re)^{1.6})^{\frac{1}{1.6}}D \quad (1\text{-}14)$$

The entry length in this case did not consider the Prandtl number. The authorities in the field typically incorporate the Prandtl number in the calculation [94]. The applicability of these entrance length can vary greatly dependent on the Rayleigh number as well as the heating condition [95]. The change in Nusselt number can be so extensive that Shah, et al. [94] presented three Nusselt number correlations based on various non-dimensional lengths in the developing flow region.

Fully developed laminar flow was investigated by Everts, et al. [96] in circular channels experiencing a uniform heat flux with upwards and downwards flow to determine the Nusselt number at Reynolds numbers below 300 and 650, respectively. Heat fluxes investigated ranged from 1 to 2 kW/m^2. The study found that widely used 4.36 for was not appropriate at these very low Reynolds numbers as the Nusselt number decreases as the Reynolds number decreases. The Nusselt number rapidly increases from zero to a constant value in the laminar flow regime as the Reynolds number increased [96]. This is an important finding as the experiments in this study were conducted as Reynolds numbers from 14 to 57, as will be presented later.

Wang, et al. [97] investigated a trapezoidal microchannel with a hydraulic diameter of 155 μm undergoing heating from below on only one wall. The laminar flow through the channel of deionised water at mass fluxes from 150 to 3850 kg/m^{2}s. The developed laminar flow Nusselt number in this study was found to be exactly 4. The main finding from the study, however, stemmed from the mass flux investigation where it was shown that the flow becomes fully developed once the flow has travelled a non-dimensional length of 0.15. It was also shown that as the mass flux decreases the distance between the inlet and the axial location where the laminar flow becomes fully developed decreases. This means that lower mass flux cases reach a constant Nusselt number closer to the inlet making the effect of the high Nusselt number in the developing region less impactful on the average Nusselt number. The Nusselt number up to 75 diameters downstream of the inlet can increase at Reynolds numbers above 1670 [98]. This constant Nusselt number under the uniform heating case is important as increases downstream could result in an under prediction of the true Nusselt number.

Mehta, et al. [99] investigated a square channel with a cross section of 5 mm by 5 mm with two different boundary conditions: a uniform heat flux and isothermal heated surface. The working fluid

was water with a Reynolds number from 100 to 850. It was found that as the mass flux decreased the distance between the inlet and the point at which the laminar flow became developed decreased. In this study it was found that the fully developed laminar Nusselt number was 3.556 and 3.018 for the uniform heat flux and isothermal cases respectively.

The type of heating applied to the outside of a channel clearly affects the laminar flow Nusselt number. A circular pipe with a uniform heat flux will have a higher Nusselt number than a channel with a isothermal wall temperature at 4.36 and 3.66, respectively [89].

Rectangular channels have a different set of heat transfer characteristics than circular channel. A rectangular channel with a uniform heat flux applied at with an aspect ratio of 6 has a Nusselt number of 6.49 and as the aspect ratio approaches infinity the Nusselt number increases to 8.23 [100]. A square channel with hydraulic diameter of 2 mm with uniform heat flux boundary condition gives a constant single-phase Nusselt number of 3.09 using deionised water at Reynolds number ranges from 25 to 100 [101].

Sun, et al. [86] deemed aspect ratio so important to the Nusselt number calculation in high aspect ratio channels that correlations were developed for rectangular channels with aspect ratios between 20 and 30. The correlation used the Graetz number which incorporates the Rayleigh number as well as the hydraulic diameter and heated length of the channel.

Lee, et al. [102] summarised the result from two thesis's by Wibulswas [103] and Philips [104] investigating the effect of microchannel aspect ratio on the Nusselt number. The authors showed that like heating type, the aspect ratio of rectangular channels substantially affect the developed laminar flow Nusselt number. An increase in the height of the channel relative to the width of the channel resulted in the Nusselt number increasing. These investigations typically categorise the laminar flow regime as having a constant Nusselt number at all Reynolds number below 2300, in the case of deionised water [100].

A widely used Nusselt number correlation for rectangular channels with various aspect ratios and a uniform heat flux applied in the develop laminar flow region is shown in equation (1-15) [105, 106].

$$Nu = 8.235\left(1 - \frac{2.0421}{AR} + \frac{3.0853}{AR^2} - \frac{2.4765}{AR^3} + \frac{1.0578}{AR^4} - \frac{0.1861}{AR^5}\right) \quad (1\text{-}15)$$

From equation (1-15), the Nusselt number is shown to be a function of the aspect ratio (AR) in the form of a polynomial. The aspect ratio for this equation is defined as the ratio of the height of the channel to the width of the channel rather than the traditional width to height ratio. Heat sinks are typically higher than they are wide resulting in an aspect ratio greater than 1.

A modified version of this equation accounts for a uniform heat flux applied to three sides of the high aspect ratio microchannel. The aspect ratio in this equation similarly is calculated as the ratio of the height of the channel to the width of the channel.

$$Nu = 8.235\left(1 - \frac{1.883}{AR} + \frac{3.767}{AR^2} - \frac{5.814}{AR^3} + \frac{5.361}{AR^4} - \frac{2}{AR^5}\right) \quad (1\text{-}16)$$

In equation (1-16) a modified version of equation (1-15) is presented for a three-sided heating case rather than a four-sided heating case.

Su, et al. [107] investigated channels that were wider than they were high. The numerical study looked at channels that were up to 20 times wider than they were high at Reynolds numbers of 51 and 510. The channels in the study were uniformly heated with the fully developed laminar flow Nusselt number investigated. It was found that increasing the width to height ratio had a similar effect to increasing the height to width ratio. The Nusselt number correlation from this study was applicable to aspect ratios from 1 to 20 (width to height) and Reynolds numbers from 25 to 2000.

$$Nu = \frac{1}{x^*}(0.054 - 0.0038AR + 0.00011AR^2 + 13.9Re^{-1.31}) + 7.541 - \frac{4.54 + 0.56AR}{1 + 0.116AR^{1.67}} \quad (1\text{-}17)$$

This correlation is the most appropriate correlation for this study although the uniform heating on all sides is not appropriate. The correlation predicted all data within a range of $\pm$ 13%. The non-dimensional length is a ratio of the distance from the inlet and the hydraulic diameter of the channel.

$$x^* = \frac{x}{D_h} \quad (6)$$

Lee, et al. [105] investigated the effect of increasing the height of a microchannel while keeping the width of the channel constant. This aspect ratio results in hydraulic diameters ranging from 200 μm to 364 μm with deionised water and an axial heat flux of 50 W/cm^2. The study found that increasing

the height to width ratio resulted in an increase in the Nusselt number experienced during developed laminar flow but has no effect on the distance from the inlet required to reach developed flow.

The working fluid can have a substantial effect on the Nusselt number calculated. Osman, et al. [108] investigated the effect of the addition of a nanofluid on the Nusselt number in a rectangular channel with a width of 8mm and height of 5 mm. The experiments used water combined with a nanofluid at concentrations of 0.3, 0.5 and 1% at Reynolds numbers from 200 to 7000. The study found that the Nusselt number was enhanced by as much as 50% through the addition of a nanofluid.

Binary fluid mixtures can similarly require different Nusselt number equations for accurate heat transfer rate predictions [109]. A water-ethanol mixture was investigated in conjunction with FC-72 to determine which of the fluids resulted in the highest heat transfer coefficient in a rectangular microchannels. The experimental investigation found that similar mass fluxes, heat fluxes and testing arrangement, the binary fluid had a heat transfer coefficient that was up to 100% higher than FC-72. Similarly, Abdollahi, et al. [101], found that by adding hexadecane to water that the heat transfer rate could be increased by up to 700% over deionised water at Reynolds numbers between 25 and 100.

Fluids such as ethylene glycol has a Prandtl number of around 100 compared to water's 7. The higher Prandtl number results in less free convection which typically enhances the Nusselt number of a fluid. This is an important consideration as it means that when choosing an appropriate Nusselt number equation the Nusselt number should ideally be for a system with the same fluid or a fluid with a similar Prandtl number so that free convection effects can be adequately accounted for [92].

From these investigations it is clearly shown that the Nusselt number is dependent on the fluid used and under the same testing conditions a different Nusselt number may result. This is problematic, as most studies consider deionised water due to its ease of use, availability, relatively high heat capacity, and its wide spread use in industry [110].

Heat flux effects can be less substantial than some of the other factors discussed. When the heat transfer is only forced convection driven the Nusselt number between heat flux cases is approximately the same [111]. In mixed convection cases heat flux can result in Nusselt numbers that are up to 50% higher at the same Reynolds number, channel geometry, orientation and heating type [112].

Channel orientation can also substantially affect the Nusselt number in fully developed laminar flow. Meyer, et al. [112] investigated the effect of changing the inclination of a circular pipe with an internal diameter of 5.1 mm and length of 4.6 m from vertical up to vertical down. The tests were conducted at Reynolds numbers of 1000 to 6000 which accounted for laminar and transitional flows. It was found that in the laminar flow portion of the Reynolds number ranges that a horizontal channel had a higher Nusselt number than a vertical channel. This was attributed to enhanced buoyancy effects in a horizontal circular pipe than the vertical upward or vertical downward flow cases.

It has been shown that the fluid used can have a substantial effect on the Nusselt number measured in the laminar flow region. The most commonly investigated fluids are water and refrigerants like R134a [102]. It has also been shown that non-uniformly heated channels are rarely investigated and that this can have a substantial effect on the Nusselt number measured. Furthermore, the aspect ratio of the channel can have a substantial effect on the Nusselt number. Low Reynolds number cases are also rarely investigated and the Nusselt number can decrease to below the expected laminar flow Nusselt number. From this literature investigation it can be concluded that if the Nusselt number's criteria are not precisely met that the effect of the above-mentioned factors can differ substantially for the true Nusselt number.

2.7 Two-phase heat transfer characteristics

Heat transfer is directly affected by flow patterns, mass fluxes and heat fluxes tested, as well as the fluid properties of the refrigerants used in two-phase flow boiling. This section investigates how each of these factors influences the heat transfer coefficient and the boiling mechanism which dominates.

Heat transfer coefficients have been used to identify two boiling mechanisms. The mechanisms for heat transfer in channels are either nucleate boiling, forced convection with evaporation or a combination of the two [1, 113]. Nucleate boiling has small bubbles that coalesce and form slugs, whereas convective boiling has large vapour columns like those seen during annular flow [79, 114, 115]. The heat transfer coefficient in nucleate boiling dominated two-phase flow is promoted when heat flux and saturation pressure are decreased. The heat transfer coefficient in forced convective boiling tends to increase with an increase in the mass flux. Vapour quality typically results in an initial rise in the heat transfer coefficient followed by a subsequent decline as dry out conditions start to present [113, 116-120].

Flow pattern significantly affects the heat transfer coefficient, with varying bubble interactions directly affecting the heated wall's surface temperature [55, 56, 120-122]. Each flow pattern has a unique heat transfer coefficient and pressure drop characteristic due to the flow structure and amount of vapour present in the channel [47].

Slug flow is nucleate boiling dominated. The slugs moving through the channel tend to result in small increases in the heat transfer coefficient with increases in vapour quality [123]. More vigorous evaporation of the liquid film occurs when the heat flux is increased; this is also typical of nucleation-dominated boiling [113, 123].

Churn flow has many interactions between the liquid and vapour, which leads to the mechanisms of heat transfer being distributed between nucleate boiling and forced convection boiling [123]. Churn flow does result in the suppression of bubble nucleation resulting in a drop in the heat transfer coefficient around the nucleation site, typical of forced convection boiling [123].

Annular flow has a high rate of heat transfer compared with other flow patterns and is desired in many heat transfer applications [124]. Heat transfer in this flow pattern occurs through the vaporisation of liquid film that thins out as the vapour core grows in the centre of the flow passage [125].

Dryout occurs when sufficient heating is applied to a system and all the liquid in the channel changes phase to vapour. This can be dangerous because the heat transfer coefficient can drop substantially at this point, causing localised super-heated spots on the wall of the channel, known as hotspots [126]. Complete dryout indicates that an entire cross-section has no liquid in contact with it.

Li, et al. [42] conducted experiments on a set of 20 horizontal parallel rectangular channels, each having a hydraulic diameter of 0.5 mm. Four flow patterns were observed: bubbly flow, slug flow, churn flow and annular flow. The study covered a wide range of mass fluxes from 164 kg/m^{2}s to 573 kg/m^{2}s and heat fluxes of up 200 kW/m^2. In all cases it was found that nucleate boiling was the dominant heat transfer mechanism due to the low pressure during the experiment (62.4 kPa). It was found that the transition from nucleate boiling-dominated heat transfer to forced convection dominated heat transfer occurred once the flow pattern changed to churn flow.

Park, et al. [121] similarly found that when the pressure of the R410A and R22 was reduced, the heat transfer mechanism was dominated by nucleate flow boiling. In their experiments, mass fluxes of

100 kg/m^{2}s to 400 kg/m^{2}s were considered, at heat fluxes from 5 kW/m^2 to 15 kW/m^2, in a horizontal smooth circular channel with a diameter of 6.1 mm. The results indicated that heat transfer performance was closely linked to heat flux, with mass flux and vapour quality having less of an effect. This phenomenon occurred at all channels sizes, from microchannel to macrochannel [122].

Tran, et al. [127] experimented with a horizontal circular tube and a rectangular channel with an inner diameter and hydraulic diameter respectively of 2.46 mm at a heat flux of 3.6–129 kW/m^2 and mass flux from 44 kg/m^{2}s to 832 kg/m^{2}s. In these ranges, minimal difference was observed in the heat transfer between two cross-sectional shapes. This finding suggests that the flow pattern was more important in heat transfer coefficient prediction than was the cross-sectional profile [128].
Surface tension has been shown to have a significant impact on the magnitude of the heat transfer coefficient in microscale channels [129]. Greco, et al. [130] showed that a horizontal smooth circular channel (internal diameter 6 mm, mass flux of 290–110 kg/m^{2}s and heat flux of 11–39 kW/m^2) displayed more vigorous boiling and higher heat transfer coefficients when fluids with lower latent heat of vaporisation and surface tensions were chosen.

Low viscosity can promote buoyancy effects; this characteristic is beneficial in experiments where the heating is one-sided [131]. Li, et al. [44] examined non-uniform heating of deionised water in a microchannel with a width-to-height ratio of 10 and a hydraulic diameter of 0.94 mm. The water experienced relatively higher average heat transfer coefficients when heated from below than heated from above, due to buoyancy effects. The channel was tested as follows: horizontal heated from below, horizontal heated form above, vertical upward flow and vertical downward flow. When fluids with a low surface tension were used, the buoyancy forces led to fast vertical motion due to low resistance from the surrounding fluid.

Fluids often used are deionised water, ethanol and a mixture of the two [132]. Water is useful due its abundance, high heat capacity, low environmental impact in case of spillage and its chemical stability. Adding 5% ethanol to the deionised water have been shown to yield heat transfer coefficients that were more than double those calculated for only deionised water or pure ethanol [133]. Ethanol can cause the point of nucleation to move closer to the inlet; in some instances, this is beneficial.

R134a is a refrigerant which has been used extensively in experimental work due to its desired properties. However, environmentally friendly alternatives – in the form of R1234yf and R1234ze (E) – have been used to replace it [134]. R404A is a fluid with a saturation temperature of -46.45°C, but it

has such a negative environmental impact that it has been banned in Europe, with R448A replacing it [135].

This replacement of conventional fluids with environmentally friendly fluids creates the need for new research having the same breadth and depth of detail that is available for traditional fluids. Due to new fluids being produced, and the wide range of mass fluxes and heat fluxes at which they can be used, research effort is required to investigate these fluids. Such research needs to produce boiling curves, flow pattern maps, instability analyses and heat transfer coefficients for the types of heating that can be expected [125, 136-141].

FC-72 is a refrigerant that is thermally and chemically stable; it is compatible with sensitive materials, is non-flammable and non-toxic and leaves no residue upon evaporation [142]. It has a low saturation temperature and surface tension, making it applicable in electronic cooling applications. In these applications, the heating is often one-sided and is best cooled with a high aspect ratio microchannel.

2.8 Influence of channel orientation

The orientation of a channel can be described in terms of the channel's relative rotational (azimuth) orientation (θ). When a flow passage is significantly non-circular, and/or when it experiences circumferential non-uniform heating, and/or when buoyancy-driven flow effects are significant, the rotational orientation indicates whether heating predominantly occurs from below, above or the side.

Flow boiling has been studied extensively in both uniform [143-145] and non-uniform heat fluxes [43, 146-149]. Rotating a channel normally occurs with a non-uniform circumferential heat flux and a channel with an aspect ratio not equal to 1, with the goal of such study being to determine how buoyancy affects the bubble dynamics.

Table 1 shows experimental studies in which the channel orientation was varied. All studies that considered orientations other than horizontal and vertical only considered the effect of changing the inclination of the channel. No studies considered the effect of rotating the channel between horizontal heated from below and horizontal heated form above. The channel geometries used in the study were mostly rectangular with aspect ratios up to 40 being investigated. A wide array of fluids have been investigated including the dielectric fluid FC-72. Mass flux experimental investigated were varied ranging from 156 to 2030 kg/m^{2}s.

Table 1: Flow boiling experimental studies with uniform and non-uniform heating methods

Reference	Internal size width x height (mm)	Orientation	Fluid	Heating type	Mass flux (kg/m^2s)
[44]	5 x 0.5	Horizontal heating from below and above, vertical upward and downward	Deionised water	Single-sided, uniform heat flux	200-500
[71]	1 (circular)	Horizontal, vertical upward and downward	R-134a	Uniform heat flux	250-820
[150]	20 x 0.22	Horizontal heating from below and above, vertical upward and downward	Deionised water	Single-sided, uniform heat flux	193-911
[151]	0.305 x 0.29	Horizontal heating from below and above, vertical upward and downward	Deionised water	Single-sided, uniform heat flux	156-470
[152]	2.5 x 5	Horizontal, vertical upward and downward	FC-72	Uniform heat flux, top wall, bottom wall or top and bottom wall	183.5-2030.3
[153]	40 x 1	Inclined: 0°, 45°, 90°, 130° and 180°	FC-72	Single-sided, uniform heat flux	211
[154]	16 x 1.7	Inclined: 0°, 30°, 60°, 90°, 120°, 150° and 180°	FC-72, HFE-1700, HFE-7000	Single-sided, uniform heat flux	401-518

Inclination effects have been investigated extensively in macrochannels. This is partly because of their importance in nuclear and other industries in which horizontal and vertical flow passages are commonly found [155]. For macrochannels, rotational effects have also been investigated because of their importance in horizontal flow boiling – for instance, in direct steam generation processes in the solar power industry, where parabolic trough or Fresnel solar receivers [115] are utilised.

The heated surface temperature is necessary in the calculation of the heat transfer coefficient between the heated wall and the fluid. This surface temperature can be measured in different ways, depending on whether the heating was uniform or non-uniform circumferentially. When the heating is uniform, the temperature can be measured using a set of thermocouples placed close to the wall's surface. The heating is normally provided through a heating wire wrapped around the channel; after a specified period of heating, an array of thermocouples are placed around the circumference of the tube – sometimes as many as eight. This array provided the average wall temperature value around the entire circumference [115, 156-158].

Non-uniform heat fluxes in microchannels have been implemented using an array of cartridge heaters below the surface of the channel [44, 159]. This arrangement is most often used in experiments with multiple channels but has also been used for single-channel experiments. By exposing a portion of the channel to the metal that encapsulates the cartridge heaters, a non-uniform heat flux can be created [6, 123, 146]. The surface temperature in these arrangements are measured using a thermocouple placed just below the channel in the metal encapsulating the cartridge heaters.

Heating with cartridge heaters require some approximation of the surface temperature at the locations being measured. Sputtering is a technique in which a 20–200 nm thin layer of a metal, such as indium tin oxide or tantalum, is added to the surface that requires heating. A voltage is then applied at either end to facilitating ohmic heating. Heated surface temperature measurements are then recorded using an infrared camera [30, 45, 54, 133, 144, 160-164]. This technique has three main benefits. First, a temperature profile can be created across the entire heated surface, allowing for two-dimensional transient temperature variations to be measured. Second, the heater is a few nanometers thick, which helps to decrease the overall size of the experimental setup. Lastly, the metal can be sputtered thinly enough to make it optically transparent, allowing for flow visualisation with a high-speed camera.

Another challenge in experimental testing at various orientations is measuring the orientation directly [150, 151, 165]. In experiments where the inclination of channels is varied incrementally, the main method of changing the position is by using a stepper motor [7, 166]. This allows measurable and repeatable changes in the position to be produced. Rotational positions are harder to measure and often require mounting a test section on a horizontal platform, from which the orientation can be measured. Lokhat, et al. [167] examined a heat sink, which needed to be inclined at several different angles, but they were unable to use a stepper motor to vary the orientation due to the weight of the

experimental setup. Instead, the orientation was fixed in position by designing a special tilted wooden cradle, which was attached to the mechanical structures in which the setup was held.

Strąk, et al. [154] experimented with a minichannel which had a width of 180 mm and depth of 4 mm, and conducted flow-boiling with FC-72, HFR-7100 and HFR-7000. Inclinations were changed between bottom-heated and top-heated in 30° increments. It was found that an inclination angle of 90° gave the highest local heat transfer coefficient for FC-72, whereas HFE-700 had the highest heat transfer coefficient at 120° in the saturated boiling region.

Mingchen, et al. [168] experimentally showed that channel inclination and rotation of a heat sink operated with R134a at mass fluxes of 370 kg/m^{2}s to 1250 kg/m^{2}s significantly affected the heat transfer coefficient. It was found that heating a set of square horizontal parallel microchannels (0.5 mm) from below rather than from above would yield a heat transfer coefficient that was up to 14% higher at low heat fluxes and 10% higher at high heat fluxes.

Li, et al. [44] reported similar trends in their study of a non-uniformly heated microchannel (width 5 mm; depth 0.5 mm) at mass fluxes of 200 kg/m^{2}s to 500 kg/m^{2}s of deionised water, with heat fluxes between 4 kW/m^2 and 25 kW/m^2. The study considered vertical upward and downward flows as well as horizontal flow with heating from above and below. Li et al. found that when the microchannels were heated from below, the heat transfer coefficient was up to 20% higher than when they were heated from above. For upward flow, the coefficient was 25% higher than for downward flow. These influences were magnified at low mass fluxes and high heat fluxes. At higher mass fluxes, orientation did not influence the heat transfer as strongly.

Ajith Krishnan, et al. [151] conducted a study with 31 parallel microchannels (width 305 µm; depth 290 µm) at heat fluxes between 441 kW/m^2 and 993 kW/m^2 and mass fluxes from 300 kg/m^{2}s to 900 kg/m^{2}s of deionised water. It was found that under these test conditions, the channel's rotational position had little influence on the heat transfer performance of buoyancy-driven secondary flows. In another related study by some of the same authors [150], flow boiling was considered in vertical upward and downward flows as well as horizontal flow, with separate heating from above and below, in a single microchannel (a microgap of width 20 mm and height 0.2 mm) and mass fluxes of 303 kg/m^{2}s, 610 kg/m^{2}s and 911 kg/m^{2}s. Again, channel orientation had little influence on the heat transfer coefficient. In both cases the relatively high mass fluxes were attributed to the minimal change in the heat transfer coefficient due to insignificant bubble-wall interactions.

Inclination and rotation can have a significant influence on the heat transfer coefficient of a channel at various hydraulic diameters. Mass flux and heat flux can also affect the prevalence of nucleate boiling and forced convection with evaporation heat transfer mechanisms. Rotation of one-side heated horizontal channels have been investigated only when heated from below and above, with intermediary rotations largely ignored. FC-72 has been used in prior heat transfer studies, with uniform heated channels being investigated.

Manned and unmanned aircraft have electronics that require active cooling due to high thermal loads. The cooling orientation changes relative to gravity as the aircraft rotates to turns or the pitch of the aircraft changes (inclination). These types of applications require the cooling associated with each orientation to be known to avoid electronic components from failing. The accelerations and decelerations on aircraft can be considerable but are often combatted by increasing refrigerant mass flow rates [169]. Microscale channels have flow dominated by surface tension rather than buoyancy forces making the heat transfer behaviour less susceptible to transient aircraft motion making their use more appropriate for cooling of aircraft electronics [170]. Little research has considered the effect of gravitational orientation in microscale channels, thus more research is required in this field [171].

2.9 Flow instability

Flow instability can be defined as the occurrence of fluid motion which differs from a quasi-steady state condition. Flow instability research is important because of the danger this phenomenon can pose to instruments due to pressure fluctuations but also resulting surface temperature effects (such as premature dryout). Furthermore, the depth of analysis required to predict the flow behaviour renders such studies necessary. Problems associated with flow instability include mechanical vibrations, which can damage components and produce noise in control sensors [172]. In addition, flow instabilities can lead to dryout conditions prior to compete flow boiling occurring. This is known as premature reaching of the critical heat flux [173]. Ineffective heat transfer can result from elevated surface temperatures and serious damage can result to the system being cooled, such as burn out [174].

Boure, et al. [175] identified two categories of instability: static and dynamic instabilities. A sudden change in the baseline steady state flow dynamics is referred to as static instability, whereas changes that occur transiently due to vapour–liquid interactions are referred to as dynamic instability. In

general, dynamic instabilities tend to be short-period oscillations. Static instabilities tend to last several minutes, with the changing parameter phenomenon manifesting as Ledinegg instability [176].

Parallel channels have an additional instability mechanism in the form of flow maldistribution. This means unequal mass flow rates between channels which can produce reverse flows purely due to flow distributions [172, 177]. Long-period instabilities associated with multi-channel systems can be corrected by better controlling inlet flow distribution to obtain a more symmetrical flow distribution. This is achieved by adjusting the inlet plenum's geometry prior to the multi-channels' inlets [178].

Dynamic instabilities occur in both single- and multi-channel arrays. The magnitude and frequency of the instability can be affected by the fluid pressure and the mass flux [68]. The impact of the instabilities can be evident in pressure oscillations, density wave oscillations and thermal oscillations [175, 179]. Some of these may result in periodic dryout, flow regime changes and reverse flow [180].

The criteria to define the transition between stable and unstable boiling are generally defined through visual inspection, thermocouple data or pressure data. Three of the most widely used approaches are as follows:

- Brutin, et al. [181] suggested that a stable flow can be said to occur when there are no pressure-drop fluctuations of more than 1 kPa above the mean pressure.
- Celata, et al. [182] suggested that visual inspection is the best approach. In this approach, observable reverse flow would indicate whether there was instability in the system. For this purpose, reverse flow is defined as any vapour bubble motion in the upstream direction [177].
- Lv, et al. [183] suggested that temperature and pressure fluctuations greater than 0.5°C or 0.5 kPa at the inlet or outlet would indicate that the flow behaviour was unstable.

The above methods are often used to quantify the flow instability, focusing on one or a combination of the criteria [144]. Instability in flow boiling is important when considering the operational conditions of microchannels because the bubble-volume-to-channel-volume ratio is relatively large at this length scale [184]. Achieving stable flow behaviour during two-phase boiling allows for accurate and transiently consistent pressure drop and heat transfer coefficient values to be determined.

Researchers conducting experiments have consistently reported that the most unstable region of boiling occurs at the onset of nucleate boiling [44, 183]. One of the most common ways of reporting the instability is by analysing pressure fluctuations in terms of time and magnitude [183, 185, 186].

Often, the oscillations from the pressure drop and temperature are found to occur in phase with one another and can be grouped into short-period oscillations and long-period oscillations [186].

Short-period oscillations are generally the result of vapour expansion and last roughly 2 s [187]. The intensity of these oscillations increases as the wall temperature increases, because the rapid expansion of liquid to form vapour becomes increasingly vigorous as the wall temperatures rises [188]. Increases in heat flux decrease short-period oscillations [186]. Reverse flow is an example of a short-period oscillation and is normally observed using high-speed cameras [177].

Long-period oscillations are generally due to flow pattern effects, such as those created by annular and mist flows, and are typically in the order of 120 s to 600 s [187]. Long-period fluctuations create more intense wall temperature and pressure oscillations because the wall has longer to store the elevated temperature before initiating an instability [189].

Pressure instability analysis has been conducted at different inclinations, with the goal of producing stability maps and providing a parametric study of the factors which influence the system's stability [190]. Mishra, et al. [191] studied three parallel channels with a hydraulic diameter of 14.2 mm, which were inclined to 0°, +30°, +45°, +60° and +90° at a fixed operating pressure with a uniform heat flux. Stability maps were created by analysing the density wave oscillations with linear and non-linear stability models. The researchers found that by increasing the inlet pressure, they could increase the system's stability. By contrast, increasing the outlet pressure had the opposite effect, destabilising the system [190].

Microchannels experience short-period fluctuations in flow regimes due to vapour backflow or reverse flow. This situation requires transient analysis of the flow regime and the development of transient flow regime maps and dryout maps [1]. These maps group unstable and stable regions by a phase-change number and a subcooling number [192]. The phase change number is defined as the ratio of the total input energy to the total energy required for complete boiling. The subcooled number is a ratio of the total heat added to the system to yield saturation conditions and the latent heat of evaporation.

Instability in microchannels can result in premature dryout on the heated surface, resulting in surface temperatures above the operating temperature of electronic components. The presence of instability is transiently monitored using high-speed visual inspection of the liquid–vapour interaction, inlet and

outlet thermocouple data or the inlet and outlet pressure transducer data. Stability maps and the effect of flow instability on the heat transfer in single microchannels depend on the fluid studied as well as the mass flux and heat flux tested. Minimal data on instability is available for FC-72 in a single microchannel.

Hong, et al. [193] investigated flow instability using independent pressure transducers, a differential pressure transducer and thermocouples on the heated surface. In the study, a low frequency high amplitude instability were identified in a microchannel heat sink. Deionised water was boiled at mass fluxes from 12 kg/m^{2}s to 110.5 kg/m^{2}s at heat fluxes from 79.6 kW/m^2 to 176.4 kW/m^2. The independent pressure transducers were used to independently determine the frequency and magnitude of the instability events that occurred. From this data it was found that pressure drop oscillation was the main flow instability. It was also found that slug flow and annular flow had different instability frequencies ranging from 0.47 Hz to 0.55 Hz. Dryout was attributed to instability events. Instability events were deemed to be both undesirable and dangerous.

Chang, et al. [194] used differential pressure transducers to distinguish between stable and unstable flow boiling. The goal of the study was to determine which mass flux and heat flux combinations produced unstable flow behaviour. Reverse flow was identified using the magnitude of the pressure drop. The test section was a heat sink with 15 parallel microchannels with a hydraulic diameter of 86.3 μm. Deionised water was boiling the heat sink at a heat flux of 7.91 kW/m^{2}s and mass flux of 22 kg/m^{2}s. A total pressure drop was defined as the maximum instantaneous pressure drop minus the minimum instantaneous pressure drop at any point in an experiment. If this total pressure drop was more than 6 kPa the system was defined as being unstable. The analysis identified changes in bubble length during unstable boiling. Vapour motion towards the inlet and outlet was observed. These vapour motions were not directly correlated with inlet and outlet pressure transducer data.

Chen, et al. [195] investigated the surface temperature response from flow instability. 60 parallel microchannels each with a width of 100 μm and depth of 389 μm was used with FC-77 at mass flow rates of 20 ml/min to 80 ml/min and heat fluxes of 30.5 W/cm^2 to 62.3 W/cm^2. The study found that that around the nucleation stie in the centre of the channel little change in the heat transfer coefficient was observed. Heat transfer was found to be enhanced by instability events upstream and downstream of the nucleation site. The improved heat transfer performance was attributed to changes in flow pattern. The flow instability was not directly correlated with inlet and outlet pressure transducer data.

2.10 Summary

Flow boiling is used in the cooling of microelectronics, mainly because of its ability to remove heat during the evaporation of the liquid-phase in a channel while remaining at a constant saturation temperature. Mass flux, heat flux, fluid properties, channel geometry and channel orientation affect the flow patterns observed. Flow patterns influence the heat transfer coefficient; for example, premature dryout results in decreased heat transfer performance whereas flow patterns with liquid films result in improved heat transfer performance.

Non-uniformly heated horizontal channels have been investigated mainly at a top-heated and bottom-heated rotation, with intermediary rotations not yet investigated. Multi-channel systems are more susceptible than single-channel systems to experience dangerously high surface temperatures because of hotspots, as heat cannot be transferred as effectively in the cross-sectional direction. Relatively low mass fluxes result in improved heat transfer performance when fluid like FC-72 are used which have relatively low surface tensions. Channels heated from below have been found to have better heat transfer coefficients than top-heated channels with the effect of intermediary rotations so far not studied.

3. Experimental setup

This chapter describes the experimental setup that was used in this study. The discussion includes the test facility, microchannel test section, orientation adjustment system and the properties of the working fluid. Special attention is given to the orientation of the microchannel and how it was adjusted.

3.1 Test facility

Figure 1 presents a schematic representation of the experimental facility, which was located at the University of Edinburgh. It enabled single-pass motion of FC-72 (C_6F_{14}) for heating and flow boiling, within an electrically heated microchannel test section at various rotations (θ).

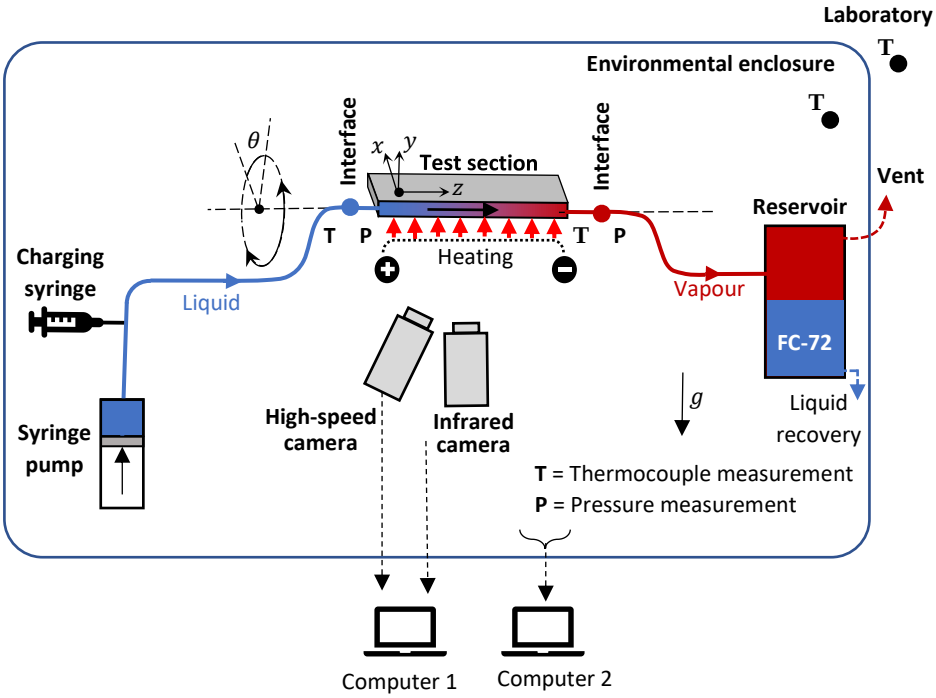

Figure 1: Schematic representation of the experimental setup

The same facility was used in several previous studies [45, 54, 160-163, 196]. A few modifications were made to allow adjustment of the test section's inclination to facilitate purging of air from the flow loop. The decommissioned experimental facility had to be reassembled with the main modifications being mounting the test section as well as the inlet and outlet interfaces onto a rotary stage. All other pieces of equipment were already present from the previous studies in a decommissioned state. The test section, discussed later, was designed, and constructed for this study, as is presented in 3.2.

The flow path consisted of the following items, shown approximately from left to right in Figure 1: a syringe pump, a charging syringe, rigid tubing and flexible hosing, an inlet interface to the test section (containing pressure and temperature sensors), a transparent test section, an outlet interface (also containing pressure and temperature sensors), rigid tubing and flexible hosing, and a fluid collection reservoir. A high-speed camera and an infrared camera were used to enable flow visualisation and heated surface temperature observations. The flow path and the cameras were located within an acrylic-glass enclosure to shield the experiment from possible thermal variations in the laboratory. The data acquisition systems and a direct current (DC) power supply were located outside the enclosure.

FC-72 was pushed through the flow path with a KDS 100 syringe piston pump (KD Scientific) with a Vernier calliper used to measure the internal diameter of the glass syringe, which was 34.2 mm (± 0.02 mm) and maximum enclosed volume of 100 ml. The internal diameter was measured with a Vernier Calliper. The piston was moved via a screw-thread mechanism connected to an electric motor. The motor speed was adjustable to sustain a constant volumetric flow rate of between 0.1 μL/h and 506 mL/h, with an accuracy of 1%. The suitably sized charging syringe was used to fill the system with fluid and to purge air from the passages.

The syringe pump's outlet was connected to the test section inlet interface by means of flexible tubing with a total length of roughly 500 mm and internal diameter of approximately 3 mm. This was attached to rigid tubing, which was about 20 mm long, with an internal diameter of 5 mm. This interface was connected to the test section interface shown in Figure 2.

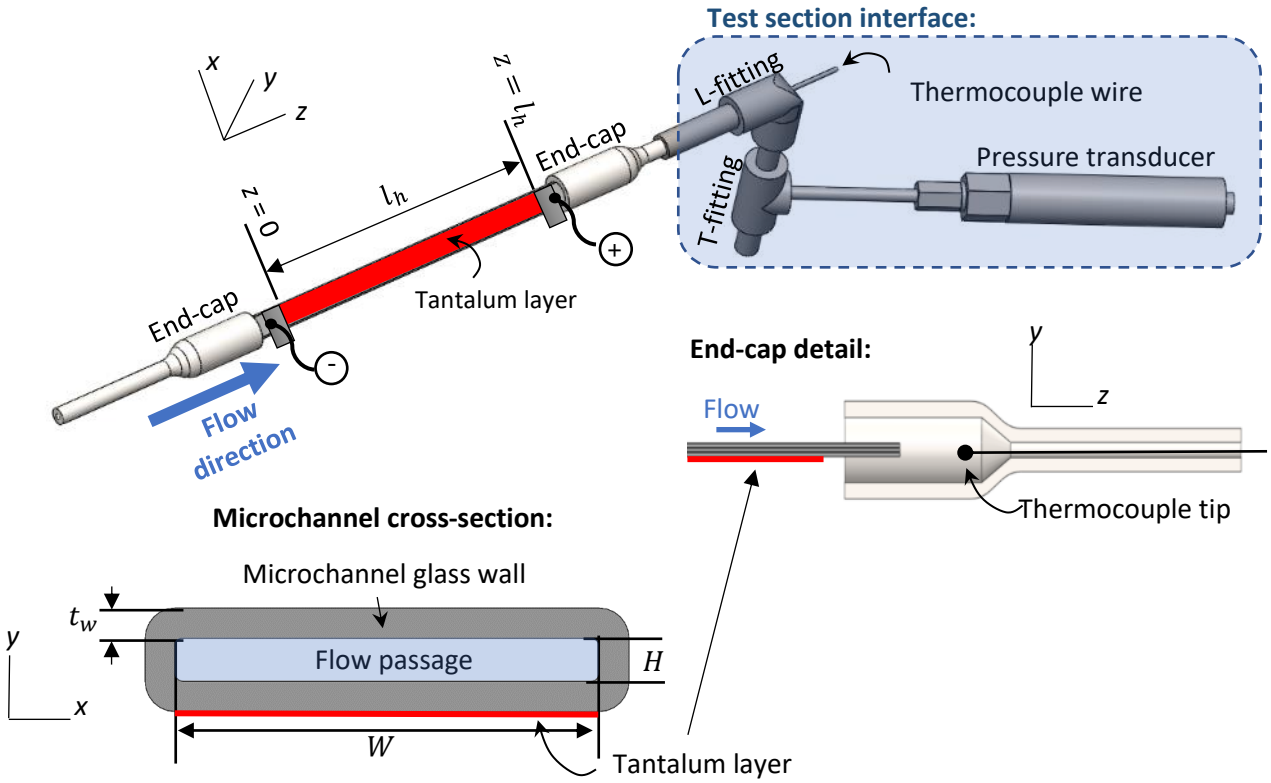

Figure 2: Inlet interface: Solidworks drawing of components

The inlet interface was used both as a fluid delivery system to the test section from the syringe pump and as a method of monitoring the inlet temperature and pressure. A PXM219 gauge pressure transducer (Omega®) was linked to the T-fitting push-pull connection and was used to measure the pressure directly upstream from the test section. It had a maximum measuring range of 0 kPa to 250 kPa, with an accuracy of 0.025% of the full-scale range, and a response time of approximately 2 ms. The full-scale range used in this experimental setup was 0 kPa to 200 kPa. The calculation of the pressure measurement uncertainty is discussed in section 5.5. The experimental had an atmospheric pressure of 101 kPa.

An L-fitting push-pull connector (John Guest®, part number PEM0310W) was the final component in the interface which linked the inlet interface to the test section. This connector had a 1.5-mm diameter hole drilled into it, allowing a thermocouple to be placed inside. A K-type thermocouple (with a measuring-tip diameter of approximately 1 mm) was positioned directly in the flow and was used to measure the inlet fluid temperature to the test section. The hole through which the thermocouple lead entered the L-fitting was resealed with Araldite® Rapid epoxy.

A mounting block was connected to the rigid tubing entering the T-fitting, allowing the inlet interface to be attached to an orientation adjustment system. The orientation adjustment system consisted of a side-mounted rotary table (Axminster®) and an extruded aluminium frame, onto which the inlet and outlet interface assemblies were bolted. The inclination of the channel was adjustable via the rotary table so that air could be purged from the flow path. The rotation of the system was adjusted within the L-fitting as is discussed in section 3.3.

The test section is described in detail in section 3.2. The test section had a channel which was placed between two endcaps which in turn were connected to the inlet and outlet interface. The channel's main features were as follows: transparent walls; one-sided heating via a visually transparent metal coating; and the test section's ability to be set at different rotational orientations.

An outlet interface was attached to the outlet of the test section with the same configuration as the inlet interface in reverse order. The temperature and pressure at the outlet were measured in the same way as at the inlet, using a PXM219 gauge pressure transducer (Omega®) and K-type thermocouple. A section of flexible tubing connected the outlet interface to the fluid collection reservoir.

A glass reservoir with a volume of approximately 350 mL was used to collect the FC-72 from the outlet of the test section via a combination of flexible hosing and rigid tubing, similar to that at the inlet. The tubing, hosing and the reservoir were not thermally insulated, which facilitated condensation cooling of the FC-72. The reservoir had a drain to recover the liquid and a vent to the outside of the laboratory to maintain the system at atmospheric pressure (approximately 101 kPa).

A high-speed camera (Basler® acA800-510um CCD) with a 12-mm fixed lens was used to record the flow visualisations inside the test section. The camera had a resolution of 800 x 600 pixels, and a maximum frame rate was 511 frames per second (fps). The camera's position was altered according to the test section orientation. The camera was placed perpendicular to the heated-wall side of the channel, with a backlight located at the opposite side of the channel, illuminating the channel.

An infrared camera (FLIR® A645) with thermal sensitivity of 20 mK, resolution of 640 x 480 pixels, and maximum frame rate of 25 fps was used to record the external surface temperature of the heated wall of the test section. Care was taken with its viewing angle to prevent self-generated heat

reflections known as aberrations. The camera was orientated at a slight orthogonal offset of less than 5° relative to the test section's heated surface.

As mentioned, the flow path and the cameras were housed in an acrylic-glass enclosure, which had a door that could be locked shut on the three non-hinge sides. It measured 1 m x 1 m x 1 m and its internal temperature was recorded by a K-type thermocouple. Another K-type thermocouple recorded the ambient laboratory temperature. The enclosure prevented any infrared reflection from laboratory equipment from affecting the heated surface temperature measurements from the test section. Furthermore, the environmental temperature around the test section remained approximately constant, which was important for heat loss calculations (section 5.1), because the enclosure stopped free circulation of air around the test section.

The test section was electrically heated by a dial-operated 240-V alternating current VARIAC transformer (Clairtronic®) connected to a DC rectifier. The DC supply current and voltage were measured with two multimeters (MASTECH® MS8239), which had measuring accuracies of 1%+10 for the current (mA) and 0.5%+2 for the voltage (V) readings. The resolution of the current reading was to two decimal places and the voltage reading was to one decimal place. A typical current measurement was in the order of 10s of mA and a typical voltage measurement was in the 10s to 100s of V. The VARIAC and rectifier were located outside the environmental enclosure and the rest of the equipment was inside the enclosure.

Two computers were used to measure the various sensory equipment. An Asus Zenbook laptop, storing the infrared and high-speed images, was used; it ran a 64-bit Windows 10 system. The second was a Dell laptop running a 32-bit Windows 7 system; here, the thermocouple and pressure transducer data was collected and stored. Two systems were required due to the operating system versions requirement.

The software ResearchIR provided the interface with the infrared camera, capturing the surface temperature on the heated side of the channel in the form of an infrared video. The video was later converted to a set of infrared images. The software allowed for several settings to be changed, including the atmospheric temperature, reflected temperature, optics temperature, distance from the object and the emissivity of the channel. These aspects all affected the measured surface temperatures. The chosen parameters are discussed in section 4.1.3.

Pylon Viewer by Basler AG was the software used to capture the high-speed images. The software allowed the frame rate, length of video, frame size and several other exposure parameters to be controlled with the chosen parameters discussed in section 4.3.3.

LabVIEW™ was run on the Dell computer which recorded the thermocouple data and pressure transducer data. Thermocouples were attached to a data card, National Instruments (NI) SCX1-1303, which slotted into a chassis, NI SCXI-100. This equipment enabled recording of the inlet and outlet temperatures of the FC-72, air temperature inside the enclosure and the laboratory air temperature. Data was sampled at 100 Hz.

Pressure was recorded using an NI USB-6008 standalone data acquisition system connected to the LabVIEW™ program on the Dell computer. The pressure data was sampled at the same rate as the thermocouples, namely 100 Hz. The time delay of readings from different channels was approximately 200 μs.

Current and voltage remained stable during the experiment once quasi-steady state was reached in the test section. The multimeter readings of voltage and current were manually recorded using a text document that was produced for every experiment. Further information in this file included the date, orientation, working fluid, start time of infrared videos, start time of pressure transducer and thermocouple readings, high-speed camera frame rate, the channel's heated length and distance between infrared camera and channel.

Data synchronisation was performed using a MATLAB program, which obtained input times from the infrared camera as well as the thermocouple and pressure transducer data; this approached allowed the data to be directly compared at the same time step. Infrared images were captured by ResearchIR for 60 s, with the start time manually recorded in the text file. The start time of the pressure transducer or thermocouple was recorded automatically by the LabVIEW™ program. Time synchronisation between the two computers was performed by connecting both computers to the internet and automatically syncing their times.

Degassing is the process of boiling a working fluid to remove any dissolved gasses such as oxygen from the working fluid. The FC-72 used in this study arrived in the lab degassed by the manufacture and was stored in an airtight enclosure. With the advice from the laboratory staff the decision was made to only degas the FC-72 if degassed FC-72 from the supplier was not available. All two-phase

experiments used fresh unboiled FC-72 from the airtight container. Single-phase experiment were done using the boiled FC-72 as it was assumed that the dissolved gasses would have a negligible effect on the single-phase results.

3.2 Test section

Figure 2 (a few pages above) provides a schematic representation of the test section design in isometric view and cross-sectional view. The test section consisted of a hollow circular borosilicate glass endcap at its inlet, a rectangular extruded borosilicate glass channel and another hollow borosilicate glass endcap at the outlet. The test sections used in this study was specifically designed and fabricated for this study using the learning from previous investigations and an iterative design approach.

A set of 15 identical microchannels were procured (VirtoCom™) to allow for possible breakage. Each had an axial length (l) of 100 mm ± 0.02 mm in the z direction, an inner width (W) of 5 mm ± 0.02 mm in the x direction and an inner channel depth (H) of 0.5 mm ±0.02 mm in the y direction. The wall thickness (t_w = 0.35 mm ± 0.02 mm) was uniform along the length of the microchannel. The flow passage had a hydraulic diameter (d_h) of 909 µm and an aspect ratio of 10. A portion of the length was electrically heated (l_h = 75 to 80 mm ± 0.02 mm) via an electric current that was passed through a tantalum (Ta) metal layer, which was sputtered on one of the external surfaces of the microchannel. These cross-sectional dimensions are shown in Figure 3 and the channel classification using the non-dimensional numbers is shown in Table 2.

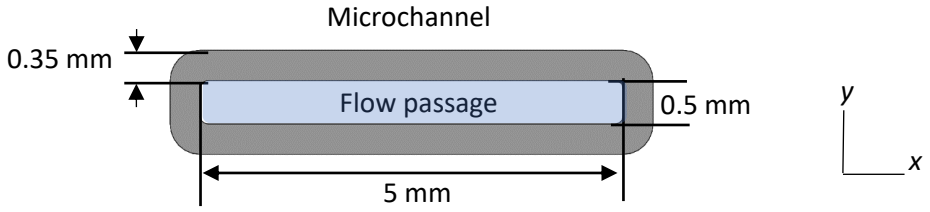

Figure 3: Cross-sectional view of microchannel with dimensions

Microchannel physics are said to be present at confinement numbers larger than 0.5. The confinement number calculated for this channel with FC-72 was 0.797, suggesting microchannel physics would dominate the flow behaviour. The capillary number and bond number both have a critical value, which was used as the transitional criterion between macrochannel and microchannel physics. Several studies have tried to define this point, with the resulting definitions varying greatly. Despite the

inconsistent transition criteria, the capillary length (724 μm) suggested minichannel physics would dominate and the bond number (1.58) suggested that microchannel physics would dominate the flow behaviour. The transition criteria were calculated for FC-72, which has a surface tension that is relatively low compared to other fluids (such as ethanol and water).

Table 2: Non-dimensional numbers for chosen microchannel

Non-dimensional number	Value	Comments
Confinement number	$Co = 0.797$ $Co_{crit} = 0.5$	$Co > Co_{crit}$ which defines the channel as a microchannel
Capillary length	$l_{cap} \approx 724\ \mu m$ $d_h = 909\ \mu m$	$d_h/l_{cap} < 1.26$ which suggests a combination of microchannel and macrochannel physics will be observed
Bond number	$Bo \approx 1.58$ $Bo_{crit,strict} = 3$ $Bo_{crit,lenient} = 4$ $Bo_{crit} \approx 4.49$ [69]	$Bo < Bo_{crit,strict} < Bo_{crit,lenient}$ These bond numbers suggest microchannel physics dominate

Tantalum was sputtered on one side of all the microchannels in a class 10 cleanroom at the Scottish Microelectronics Centre located at the University of Edinburgh. To enable one-sided heating of the channels, the metal was deposited to one side of the microchannel only in the x-z plane. Before sputtering, the channels were prepared by cleaning them in a Piranha solution (a combination of sulfuric acid and 30% hydrogen peroxide at a ratio of 3:1) for 30 min. This process removed impurities and biological agents from all microchannel surfaces. Once cleaned, the microchannels were flushed with deionised water and dried on a 150°C heated surface.

To ensure even and consistent coating, all the microchannels underwent sputtering simultaneously, using a Plasmalab System400 from Oxford Instruments. The final tantalum thickness of 22.5 nm resulted in a metal layer that was transparent in the visible spectrum and had an electrical resistance of 56 kΩ/m.

After the sputtering process, the end-caps (which were produced by a glass blower at the University of Edinburgh) were attached to the microchannel, as shown in Figure 4. The joints were produced by using Araldite® Rapid epoxy, which does not react with FC-72 and has a melting temperature of 80°C

(34°C higher than FC-72's saturation temperature). This resulted in air-tight seals and prevented FC-72 or air from leaking out of or into the test section. The endcaps had an inner diameter of 6 mm and outer diameter of 10 mm at the microchannel end. The large diameter section was approximately 30 mm long and the thinner section was approximately the same length. The thinner section had an outer diameter of 5 mm and an inner diameter of 3 mm.

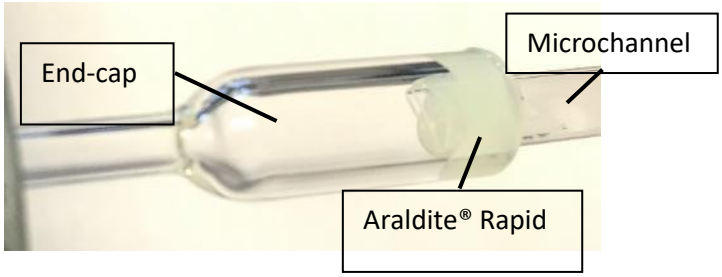

Figure 4: End-cap and microchannel assembly

During the experiments, the electric heating circuit was completed by clamping the positive and negative electrodes of the DC power supply to the tantalum-treated test section. The clamping positions were well defined by wrapping electrically conductive aluminium foil around the channel. This also ensured an even electric connection across the width of the microchannel surface, as shown in Figure 5.

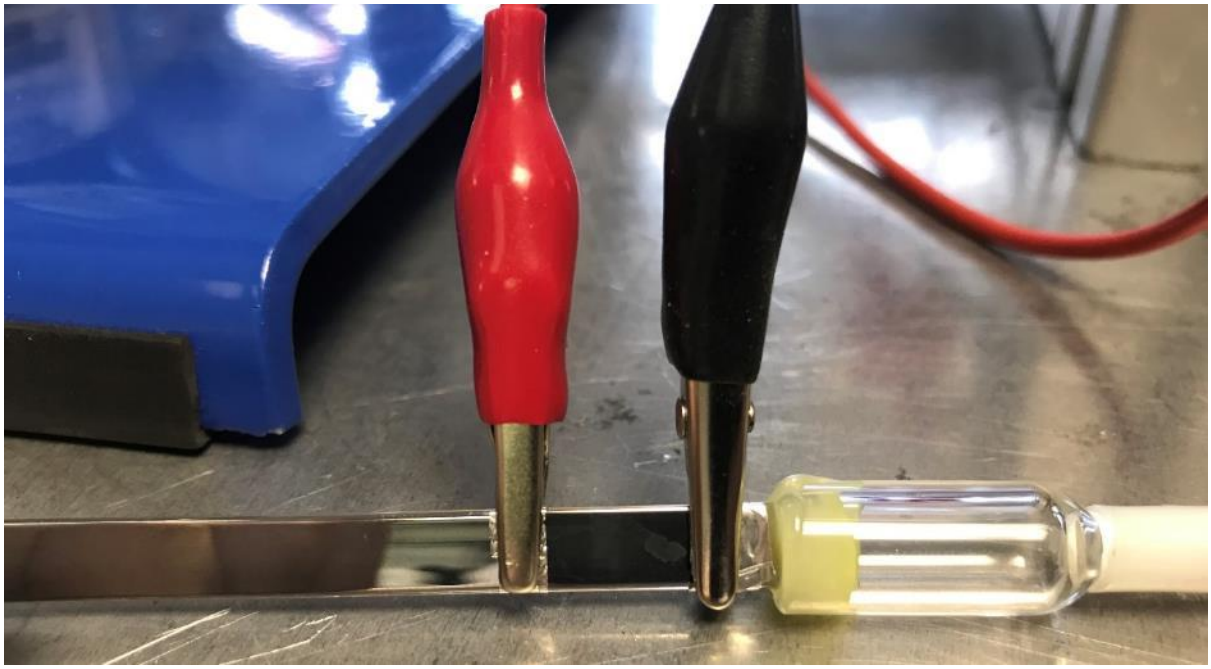

Figure 5: Crocodile clamps attached to the channel to measure its resistance

The linearity of the coating along the length of the heated wall was tested by placing the clamps different distances apart and measuring the electrical resistance. The shortest distance tested is shown in Figure 5. The coating was found to be consistent, producing a linear relationship between the distance between the clamps and the resistance measured. A second goal was to determine where heating began, which was determined by investigating the x-axis location where a resistance of zero was recorded. This was important as it was used to determine whether the system was heated on the portion of the channel observed by the infrared camera or if heating started underneath the aluminium foil. The X-axis location showed that the heating began between the innermost points of the aluminium foil rather than underneath the foil.

3.3 Orientation adjustment system

Rotation (θ) was defined as an angle from horizontal heated-from-below position at a rotation of θ = 0°. The channel was rotated about the flow direction, with θ = 90° referring to heating from the side and θ = 180° referring to heating from above (see Figure 6). The rotational positions tested were θ = 0°, 30°, 60°, 90° and 180° as is shown in Figure 6

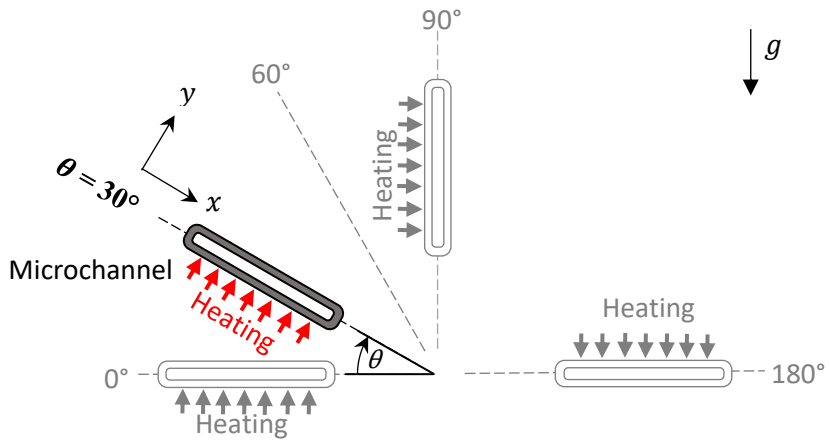

Figure 6: Heating at different rotational orientations

The rotational position was measured using two 180° protractors attached to one of the end-caps, as shown in Figure 7. Here, the test section is at a rotation of θ = 60°. Two protractors are visible, and a vertical guide was placed on the L-fitting of the outlet test section interface as a visual guide.

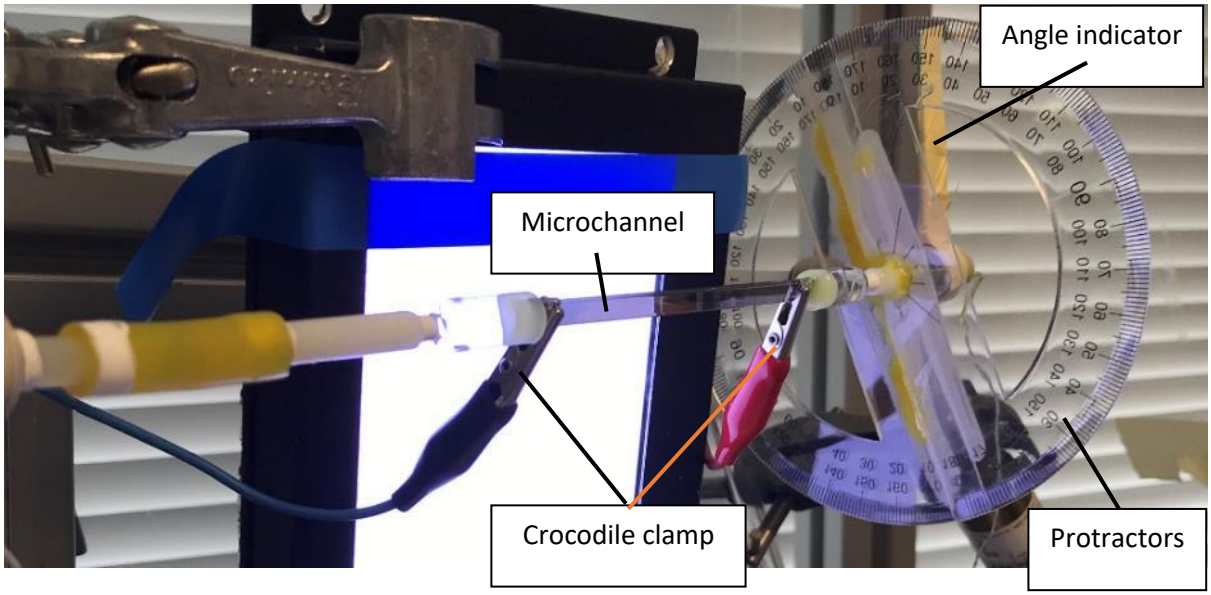

Figure 7: Test section at rotation θ = 60° with angle-measurement protractors visible as well as the angle indicator and crocodile clamps

The entire test section functioned as a single fixed unit that rotated within the L-fitting at either end. The protractors were directly attached to the rigid tubing encapsulating the endcap at the outlet of the test section, which rotated with the entire test section. A horizontal reference angle was determined from which the system could then be rotated. The microchannel was defined as being in the correct position once the angle of the system was within 1° of the specified rotation. This was a fine enough resolution for this study as the smallest incremental change in rotation was 30°.

The test section was mounted onto a rotary table attached to set of aluminium extrusions through specially manufactured interfacial blocks at the inlet and outlet. The table allowed for inclination changes. The inclination of the test section needed to be adjusted so that air could be purged from the system. For horizontal tests, the inclination of the setup was fixed in place using the clamps to ensure that the system remained horizontal.

Extruded aluminium sections were used to indirectly attach the test section to a 200-mm Axminster rotary table. The rotary table held an ER32 12-mm thread collet holder and a 14–15 mm-collet which held a stainless-steel shaft (length 50 mm; diameter 15 mm). This shaft had a threaded hole bored into it, which held a screw to lock into the aluminium extrusion, thus completing the interfacial component between the test section and the rotary table. The extrusion had a profile on all four sides that allowed screws with a specially designed head to be locked into the profile.

3.4 Properties of FC-72

Perfluorohexane (C_6F_{14}), known as FC-72, was chosen for several reasons. Table 3 lists some of FC-72's properties. The main characteristics that supported the choice of FC-72 were as follows:

- its saturation temperature at approximately atmospheric conditions is 56°C; this is lower than many electronic components' maximum operating temperature
- its dielectric properties
- its low surface tension compared to other coolants, such as water and ethanol which would promote buoyancy driven motion.

Table 3: Properties of FC-72

Property	Value source	Source
Saturation temperature at 101 kPa (T_{sat})	56°C	3M [142]
Latent heat of vaporisation (h_{fg})	88 kJ/kg	3M [142]
Vapour density (ρ_v)	13.86 kg/m^3	3M [142]
Kinematic viscosity (v)	3.8x10^{-7} m^2/s	Chang, et al. [194]
Liquid dynamic viscosity (μ_l)	0.00064 Pa·s	Chang, et al. [194]
Vapour dynamic viscosity (μ_v)	7.19x10^{-6} Pa·s	Chang, et al. [194]
Liquid surface tension (σ)	0.01 N/m	3M [142]

The FC-72 used during the two-phase experiments was unboiled. Once boiled, the fluid could have contained a large proportion of dissolved gasses, producing vapour prior to the saturation temperature being reached during boiling. Three of the liquid physical properties were calculated as a function of the local fluid temperature and are tabulated in Table 4.

Table 4: Correlations for thermodynamic properties of FC-72 [103]

Property	Equation	Units
Liquid specific heat ($c_{P,l}$)	$c_{P,l} = 1010 + 1.554T$	$(\frac{J}{kg°C})$
Liquid thermal conductivity (k_l)	$k_l = 0.060 - 0.00011T$	$(\frac{W}{m°C})$
Liquid density (ρ_l)	$\rho_l = 1740 - 2.61T$	$(\frac{kg}{m^3})$

Specific heat, thermal conductivity and density of the liquid was first measured in the fluid at the inlet thermocouple (T_{in}). The value of these properties was updated using the updated local fluid temperature (see section 5.2). The correlations shown above were calculated by the manufacturer of the fluid, 3M [142].

3.5 Chapter summary

The experimental setup located at the University of Edinburgh was updated to include a rotary table, allowing inclination changes to be made to the test section so that air could effectively be purged from the flow loop. An infrared camera mapped the surface temperature profile of the heated surface, and a high-speed camera recorded the flow patterns. Gauge pressure transducers and thermocouples measured the inlet and outlet conditions. The environmental temperature inside the enclosure and the laboratory temperature were measured using thermocouples. The rotation of the channel was altered from a bottom-heated reference position with rotations of θ = 0°, 30°, 60°, 90° and 180° tested.

4. Experimental procedure

This chapter gives an overview of the laboratory procedures that were followed in the investigation. The discussion includes the pre-calibration processes, the test matrix and the main experimental test procedure.

4.1 Calibration

Before the single or two-phase experiments were conducted, special care was taken to calibrate the thermocouples, the pressure transducers, the infrared camera settings, and the syringe pump flow settings.

4.1.1 Thermocouple calibration

As mentioned, four K-type thermocouples were used in this experimental study. The first was located at the test section inlet (T_{in}), the second at the test section outlet (T_{out}), the third inside the enclosure (T_{∞}) and the fourth within the laboratory. They were calibrated via an OPTIMA T100 thermal circulation bath which had a temperature measurement uncertainty of ± 0.1°C. The thermocouples were submerged in distilled water. Calibrations were conducted during steady state isothermal conditions for target temperatures between 20°C and 60°C at intervals of 5°C. For each target temperature, 5 min was allowed for the bath to reach thermal equilibrium and steady state. This was followed by data recording over a period of 15 s at 100 Hz, before the bath was adjusted to the next target temperature.

A temperature calibration correction curve was created for each thermocouple, based on the raw thermocouple measurements and the thermal-bath reference temperatures. This corrective curve was used during data reduction to adjust and correct the logged temperature data. The laboratory temperature's curve is not discussed as it was not used in the calculation of any output presented in this study. The curves are described by equations (4-1), (4-2) and (4-3) below.

$$T_{in} = 0.9964T_m + 0.35 \quad (4\text{-}1)$$

$$T_{out} = 0.9999T_m + 0.0697 \quad (4\text{-}2)$$

$$T_{\infty} = 0.9851T_m + 0.3498 \quad (4\text{-}3)$$

All three equations exhibited an error prediction accuracy represented by an R^2 value of 1 (i.e., the coefficient of determination). The equations reduced the mean error to less than 0.001°C for each thermocouple. Calibrations were repeated before the first experiment and after the last experimental, to check for possible drift in the thermocouple output. No observable drift was evident and the same calibration correction factors were employed throughout the investigation.

The uncertainty of the temperature measurements was obtained through a combination of bias error (b_i) and random error (p_i). The bias error was the uncertainty of the thermal bath's reference temperature and was obtained from the thermal bath's datasheet. The random error was determined using the standard deviation of the thermocouple measurements at each calibration temperature. These two absolute errors were combined as shown in equation (4-4) to determine the total absolute uncertainty.

$$\delta x_i = \sqrt{b_i^2 + p_i^2} \tag{4-4}$$

The δx_i term refers to the total absolute uncertainty of the measurement; this was determined using the bias error and random error. The random error of the thermocouple at the inlet and outlet as well as inside the enclosure was ± 0.1°C and was ± 0.2°C outside of the enclosure. These random errors were typical for K-type thermocouples. The bias error was based on the mean error previously presented for the calibration curves. These two errors resulted in an error of ± 0.14°C for the inlet and outlet thermocouple as well as the thermocouple inside the enclosure. The thermocouple outside the enclosure was not used in any output's calculations but had a mean error of 0.03°C and total absolute error of ± 0.2°C.

4.1.2 Pressure transducer calibration

Calibration of the pressure transducers was performed with a hand operated manometer (SPER SCEINEFITIFC® Model 84083). The pressure transducer was connected to the manometer with a gas tube, after which a hand-operated pump was used to increase the pressure in the tube. Once the pressure measurement on the digital read-out of the device was stable, the output measurement from the pressure transducer was recorded. Both pressure transducers were calibrated *in-situ* within the enclosure at their intended operating orientation and expected operating temperature (atmospheric ≈ 16°C).

The adjustment to the pressure values was performed by altering the raw data received from the pressure transducer before it was saved in LabVIEW to an exported file. Both pressure transducers provided a unique equation to correct the raw data. The equations were similar, shown in equations (4-5) and equation (4-6)(4-6), because both pressure transducers were of the same model.

$$P_{in} = 0.2508P_m - 0.647 \quad (4\text{-}5)$$

$$P_{out} = 0.251P_m - 0.6397 \quad (4\text{-}6)$$

The fitted linear approximations had R^2 values of 1. Prior to the corrective equations, the absolute errors in the measurement were approximately 64 Pa. After correction, the error was reduced to 3 Pa in both cases.

As with the temperature readings, the pressure measurement uncertainty was a combination of bias and random errors. The bias error magnitude represented the uncertainty of the manometer, which was 0.025% of the full-scale range used (200 kPa), namely an uncertainty of 50 Pa. The error from the linear approximations was added, producing a total bias error of 53 kPa. The random error was determined through calculating the typical standard deviation of the measurements, which was 76 Pa for the inlet and 77 Pa for the outlet pressure transducers. The total absolute error of the pressure transducers was 93 Pa and was calculated using equation (4-4).

4.1.3 Infrared camera calibration

As mentioned, the infrared camera had an uncertainty of ±2°C. The emissivity of the infrared camera's target surface was determined through a technique that uses two surfaces, one with known emissivity and the second with unknown emissivity both at the same temperature [197]. The known emissivity surface was used to ensure the camera was functioning as it should.

In this case, surface 1 was the tantalum layer on the microchannel's surface, which had an unknown emissivity, whereas surface 2 was covered by insulation tape with a known emissivity of 0.96 [198]. A calibrated K-type thermocouple was placed on each surface to check the reference temperatures. They were securely affixed to the relevant surface and forced the soldered thermocouple junction to remain in contact with the surface. The infrared camera was located above the target surfaces such that its viewing direction was approximately perpendicular to the surfaces. Because tantalum has a high reflectivity in the infrared spectrum, the infrared viewing direction was always set to

approximately 5° from the orthogonal. This prevented self-reflection of the camera on the tantalum surface, which would have resulted in substantial measurement error.

Once properly set up, both surfaces were subjected to two steady state uniform temperature conditions, 16°C and 35°C, inside the previously described test facility enclosure. The thermocouple and infrared camera measurements were performed concurrently.

The infrared camera required inputs to describe the camera's optics temperature, reflected temperature and the environmental temperature. These were assumed to be the same at the atmospheric temperature, which was measured directly by a third thermocouple in the enclosure. The distance between the infrared camera and the surfaces was recorded in the software and was measured using a Vernier calliper and remained fixed at 25 cm during the experiments. The emissivity for surface 2 was set to its known value.

The emissivity of surface 1 was determined using the ratio of the temperature difference between the two surfaces, as measured by the infrared camera ($T_{IR,1} - T_{IR,2}$) and the same temperature difference measure by the thermocouples ($T_1 - T_2$). For the measurements to be taken, the infrared camera required an emissivity value to be selected. The selected value was 1, which was approximately the emissivity of the known surface.

$$\epsilon = \frac{T_{IR,1} - T_{IR,2}}{T_1 - T_2} \tag{4-7}$$

Surface 2 was used to validate the procedure. From equation (4-7), the emissivity of the tantalum surface was calculated to be 0.8 (±0.09). This is in line with previous studies conducted with tantalum [45, 54, 160-163, 196]. The uncertainty was high due to infrared camera's absolute measurement uncertainty from the manufacture defined at ±2°C.

Additional precautions were taken to consider possible environmental influences. The acrylic-glass enclosure had a high transmittance of over 90% in the visible spectrum but a transmittance approaching zero in the spectral range of the infrared camera (7.5–14 μm). This low transmittance in the sensory range of the infrared camera ensured no external source could artificially inflate the temperature measured by the camera. The aluminium base plate on which the experimental setup was placed inside the enclosure had a reflectance of almost 99% in the infrared spectrum. The aluminium surface resulted in some radiative reflection, which was corrected for by adjusting the

position of the infrared camera and the test section. In addition, a cardboard strip was placed on the aluminium surface if reflections were unavoidable.

4.1.4 Syringe pump calibration

The syringe pump was factory-calibrated and could only be recalibrated by the company post-purchase. The calibration was checked before the experiments by comparing the displayed volumetric flow rate output on the pump with the actual measurements, using a beaker and a stopwatch, at three different mass flow rates.

A 150-mL beaker (PYREX®) which had an accuracy of ±5% was used. The syringe pump was set at 50 mL/h, 100 mL/h and 200 mL/h; these rates were close to the volumetric flow rates used during the main experiments. The rates were comparable, with the difference between the pump setting and the actual flow rate being less than 1%. From this it was concluded that there had not been significant drift in the syringe pump's calibration.

4.2 Test matrix

The goal of this study was to determine the extent to which the buoyancy forces in the channels tested affected flow behaviour by changing the rotation (θ). From literature, it was noted that decreasing the mass flux would result in the buoyancy effects becoming more dominant. Wang, et al. [163] showed that with channels of similar hydraulic diameters and the same working fluid as in the present study, buoyancy effects at mass fluxes between 11.2 kg/m^{2}s and 44.8 kg/m^{2}s, increased heat transfer coefficients. Based on this information, the mass fluxes (G) selected for this study were 10 kg/m^{2}s, 20 kg/m^{2}s and 40 kg/m^{2}s. The corresponding volumetric flow rates were approximately 53.6 mL/h, 107.1 mL/h and 214.3 mL/h. (Mass flux is defined in this study as $G = \dot{m}/A_c$, with $A_c = WH$).

The associated heat flux ranges were mass flux and channel orientation specific. The first heat flux tested was selected such that the onset of nucleate boiling would be present. The final heat flux tested was based on two criteria, firstly heating would not be increased if the maximum measured surface temperature increased to 150°C or if 7 or more heat fluxes had been tested. The infrared camera could only measure up to 150°C at an accuracy of ±2°C, above 150°C the camera's sensitivity and accuracy became less favourable. It was deemed unnecessary to test more than 7 heat flux cases as many

orientation and mass flux cases would not have had similarly high heat fluxes to which higher heat fluxes could be compared.

Table 5 lists the test cases that were considered to determine the influence of the channel rotation. The influence of the rotational orientation was determined by considering θ = 0°, 30°, 60°, 90° and 180°. All these rotations were tested at all three mass fluxes; and a minimum of four heat fluxes tested. The heat fluxes reported in this study were based on the net amount of heat absorbed by the fluid ($\dot{Q}_{net}$), considering the amount of heat lost to the environment and the amount of heat applied to the heated surface. Often this net heat absorbed was referred to as a heat flux ($\dot{q}_{net}$). Only the net absorbed heat and effective heat flux are presented in this study using the symbols $\dot{Q}$ and $\dot{q}$. Any variability in the inlet temperature was due to variation in the atmospheric temperature on various testing days. The saturation temperature variability was due to changes in the atmospheric pressure on the day of testing.

Table 5: Rotational angle test matrix

Experimental parameter	Value		
Fluid	FC-72		
Inlet temperature (T_{in})	19.5°C ± 3.5°C		
Saturation temperature (T_{sat})	56.25°C ± 0.75°C		
Rotational orientations (θ)	0°, 30°, 60°, 90° and 180°		
Mass fluxes (G)	10 kg/m^{2}s	20 kg/m^{2}s	40 kg/m^{2}s
Net heat input ($\dot{Q}$)	2.6 – 6 W	4.2 – 9 W	7 – 11 W
Net absorbed heat flux into fluid ($\dot{q}$)	3 – 7.3 kW/m^2	5 – 13.8 kW/m^2	9.6 – 15.1 kW/m^2

The degree of subcooling in this study was high at 36.5°C ± 3.5°C. Inlet temperatures, when tightly controlled, can be increased to decrease the level of subcooling. This can be important as the total pressure drop and heat transfer coefficient is affected by the level of subcooling [199]. However, variability in the level of subcooling on the heat transfer coefficient is amplified when the degree of subcooling decreases [200]. The experimental equipment used in previous studies to increase the inlet fluid temperature did not result in repeatable inlet temperatures within a narrow range which made results unusable. Experimental investigations of the effect of subcooling on the heat transfer coefficient typically suggest that as the subcooling increases to more than 20°C - 25°C the influence in open systems becomes small [200-203]. It was thus determined that the high level of subcooling, although variable, would have had little influence on the results from the experiments.

4.3 Experimental procedures

The experimental procedure was divided into three stages, as follows:

- system preparation
- single-phase experiments to determine the heat loss characteristics from the channels
- the main two-phase experiments.

4.3.1 System preparation

The existing experimental setup, used in previous investigations [45, 54, 133, 160-163, 196, 204, 205], had endured exposure to several different fluids – including ethanol, water, and binary fluids. This exposure could have resulted in fluid residue and solid-particle deposition such as dust. These first needed to be removed.

Before each main set of tests was conducted, the flow path (which included the test section) was flushed several times with deionised water at a volumetric flow rate of approximately 10 L/s to remove traces of dust and impurities. Air at a gauge pressure of 37 kPa was then passed through the flow path for at least 30 min. Furthermore, the acrylic-glass enclosure, which was equipped with an electric heating element, was heated to 36°C for 5 min to ensure full evaporation and removal of the water.

To prevent the presence of air bubbles during tests, the syringe pump was preliminarily charged with previously boiled FC-72 and the flow path was flushed again. This was done while slowly altering the channel inclination from horizontal flow to vertical upward flow, then to vertical downward flow, and back to horizontal flow. This process was repeated at least three times. Eventually, visual inspection of the opaque connective tubing and hosing indicated that the test section and all upstream and downstream tubing were purged of air and the syringe pump cylinder was empty. The syringe pump was then filled with unboiled FC-72 and the remaining flow path was re-flushed using the charging syringe.

The channel's rotation position was set using the procedure described in subsection 3.3. Care was taken to match the orientation of the pressure transducers to that used during their calibration. The infrared and high-speed camera positions were adjusted and clamped in place. Both cameras were held by test-tube clamps and stands. The position of the high-speed camera relative to the test section

and the backlight required meticulous adjustment, and care was taken to prevent self-reflection by the infrared camera.

4.3.2 Single-phase experiments

As mentioned, it was impossible to thermally insulate the test section; hence, substantial heat loss occurred from the tantalum surface to the atmosphere inside the acrylic-glass enclosure during the flow boiling experiments. To enable later calculation of the local and average heat transfer coefficients, it was necessary to determine the test section heat transfer rate into the fluid. However, during flow boiling conditions, it was quite challenging to accurately and directly determine the inlet and outlet thermodynamic states of the fluid based on the measured pressure and temperature values. Therefore, it would be impossible to calculate the heat transfer rate based on inlet and outlet measurements.

Alternatively, an energy balance could be created between the heat lost from the tantalum to the surroundings, the total power input to the heating layer and amount of heat absorbed. This method has been used extensively in the literature with one-sided heated channels with a constant heat flux and an infrared camera viewing the heated surface [206-211].

To find the heat loss characteristic of each test section orientation, single-phase liquid experiments were performed. For the liquid flow conditions, several variables could be measured directly. These included the total heat input, the heat absorbed by the fluid (based on the temperature rise of fluid in the test section), the tantalum surface temperature (obtained from the infrared camera) and the surrounding temperature in the acrylic-glass enclosure.

The above measurements enabled the characterisation of the heat loss rate from the heated tantalum surface as a function of the temperature difference between the tantalum and the surrounding air, which discussed in section 5.1. For this purpose, steady state single-phase tests were conducted for each test section orientation at mass fluxes of G = 10 kg/m^{2}s, 20 kg/m^{2}s and 40 kg/m^{2}s, and at a range of applied heat fluxes. Each rotation had approximately 21 single-phase experiments at various mass flux and heat flux combinations that were used to create a heat loss correlation.

In the two-phase region, the range of temperature differences between the tantalum and the environment were much larger than in the single-phase region, requiring accurate heat loss curves.

To reduce experimental uncertainty, the single-phase tests were conducted such that the temperature of the fluid over the test section increased at 5°C intervals at each applied heat flux. In these tests, steady state was identified when the outlet temperature changed by less than 0.1°C within 3 min, as measured by the outlet thermocouple.

A text file was created for each experiment. It reflected the date, orientation, voltage, current, thermocouple and pressure transducer start times, infrared camera start time, channel size, working fluid and any other observations that could have affected the results.

4.3.3 Two-phase experiments

Once single-phase data was collected, the main two-phase flow boiling tests could commence. The syringe pump settings were adjusted, and the pump was started. The power input to the tantalum layer remained off until fluid was seen collecting in the reservoir at the outlet of the setup. The heating was gradually increased to just below saturation conditions to prevent sudden and unexpected system instability which could result in damage to the test section or sensory equipment and system seals. Heat input was slowly increased to the target value until a stationary nucleation site was present in the channel.

Capturing of the flow behaviour was performed under steady-state conditions. Steady state during two-phase flow boiling involves natural transient flow behaviour such as the location of the nucleation site changing cyclically as well as cyclic flow instability. These cyclic variations mean that quasi-steady state conditions were achieved in this study. Quasi-steady conditions were defined as the outlet temperature having a variation of less than 0.2°C over a period of 3 min; the nucleation site remaining fixed (or changing cyclically); and the observed flow pattern remaining consistent or periodic in nature before data was recorded.

After an additional 3 min of steady conditions, the pressure transducer and thermocouple data were logged at 100 Hz for 60 s per experiment and approximately 7 min per heat flux. High-speed camera footage was recorded at between 100 fps and 140 fps, depending on the flow pattern behaviour, for 70 s. This period spanned from before the infrared image started to record until after the infrared images stopped recording. The infrared footage was recorded at 25 fps for exactly 60 s. The input power and volumetric flow settings were recorded manually. Care was taken to ensure time synchronisation between the two computers as well as the cameras.

Each test case and heat flux condition was repeated three times. Only once this sequence was complete was the next heat flux and/or mass flux and/or rotation case considered. At the end of each experimental set, the collected FC-72 in the outlet reservoir was retrieved and stored in a sealed glass jar until it could be disposed of safely.

As before, a text file was created for each experiment with the date, orientation, voltage, current, thermocouple and pressure transducer start time, infrared camera start time, channel size, working fluid and any other observations that could have affected the results. The unique text files (for both single- and two-phase tests) were saved in a folder made specifically for each experimental repetition, with high-speed camera images saved directly to the folder. Infrared camera images were captured in a video format and were renamed after the experiment with the identifiers: orientation, mass flux, heat flux and test number, before being moved to the correct folder. Thermocouple and pressure transducer data was saved on a separate computer and was named in the same way as the infrared images before being moved to the correct folder. All this information ensured that data was correctly matched up.

When a round of experiments was completed, data recording and all heating were stopped. The syringe pump continued to pump if fluid was left in the syringe to help cool down the test section.

4.4 Chapter summary

This chapter has described the calibration of the thermocouples, pressure transducers, infrared camera, and syringe pump, with both bias and random error considered. The test matrices of the rotation tests were presented, and the typical heat fluxes, mass fluxes and orientation positions discussed. The methods used to prepare the experimental setup and to conduct the single-phase and two-phase experiments were also described.

5. Data reduction

This chapter details the data processing method that was used to derive the test section heat loss characteristics, heat transfer coefficients, local vapour quality, total pressure drop, surface temperature metrics and cross-sectional temperature variability. An uncertainty analysis is presented at the end, discussing the typical uncertainty of measured parameters and output parameters.

Due to the relatively complex nature of the recorded data and the many transient state data-points, a MATLAB code was developed to automate the data reduction. From this MATLAB code, time-average local heat transfer coefficients, surface temperature metrics and pressure metrics were obtained. The code was used to determine the local heat transfer coefficients is shown in Appendix A: Data interpretation code.

5.1 Heat loss characterisation

As mentioned, diabatic steady state single-phase liquid experiments were conducted to characterise the heat loss behaviour from the tantalum surface to the surroundings. This section will discuss the approach used in this study for all rotations, mass fluxes and heat fluxes.

First, the heat absorbed into the fluid ($\dot{Q}$) was determined from the change of temperature of the fluid, shown in equation (5-1).

$$\dot{Q} = \dot{m} c_p (T_{out} - T_{in}) \tag{5-1}$$

Here $\dot{m}$ is the mass flow rate of FC-72, c_p is the specific heat capacity of the liquid, and T_{out} and T_{in} are respectively the time-averaged outlet and inlet fluid temperatures (obtained from the relevant outlet and inlet thermocouples). The mass flow rate was calculated from the syringe pump's volumetric flow rate setting ($\dot{V}$) and the liquid density (ρ).

$$\dot{m} = \dot{V} \rho \tag{5-2}$$

The specific volume and density values were assumed to be constant and were calculated from correlations supplied by the fluid manufacturer [142], based on the thermocouple temperature measurement at the inlet of the microchannel (T_{in}). These equations are described in Table 4.

The rate at which heat was applied was directly measured using ohmic heating with the DC voltage (U) and the current (I):

$$\dot{Q}_{ap} = U \cdot I \tag{5-3}$$

The voltage and current values were measured using multimeters and were manually logged for each experiment. The amount of heat lost from the system ($\dot{Q}_{loss}$) was calculated using the applied heat and the net amount of heat absorbed by the fluid, as shown in equation (5-4).

$$\dot{Q}_{loss} = \dot{Q}_{ap} - \dot{Q} \tag{5-4}$$

The amount of heat lost to the environment in the two-phase region could not be directly measured. This situation required the creation of a heat-loss correlation based on single-phase experiments in which the absorbed heat was directly measured, using equation (5-1). The single-phase correlation reflected the amount of heat lost to the environment, based on the difference between time and spatially averaged heated surface temperature ($\bar{T}_s$) and the environment temperature (T_∞). The calculation is shown in equation (5-5).

$$\Delta T_{env} = \bar{T}_s - T_\infty \tag{5-5}$$

A typical heat-loss curve for the single-phase experiments is shown in Figure 8, with heat loss as a function of the environmental temperature difference. Increasing the heat flux tested produced a steadily increasing average surface temperature, resulting in a larger environmental temperature difference. In Figure 8, a representative curve is shown, employing a power function line of best fit to represent the amount of heat lost at the various environmental surface temperature differences.

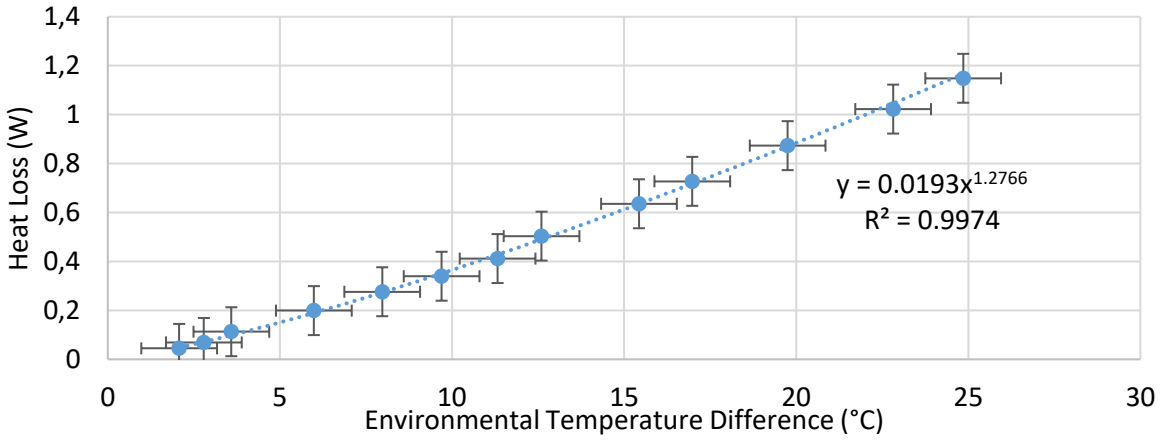

Figure 8: Amount of heat lost with increased environmental-to-surface temperature difference at an arbitrary rotation

The relationship regarding the heat loss rate, as found in the single-phase experiment, was described with two coefficients. The first was a heat loss coefficient (*a*) and the second was an exponent loss coefficient (*b*). These values are used in equation (5-6):

$$\dot{Q}_{loss} = \mathrm{a}\Delta T_{env}^{b} \tag{5-6}$$

Each rotation had a unique combination of coefficients (a and b) based on the data regression analysis. The heat loss equations correlated to within ± 1.49% (± 0.1W) of the measured ΔT_{env} values, ranging from 5°C to 25°C during the single-phase testing. In the subsequent flow boiling experimental data, significantly higher ΔT_{env} values were present, ranging from 5°C to 130°C, due to the increased heat flux that was needed to sustain flow boiling. Due to the nature of convection, which was the dominant heat loss mechanism, it was assumed that the heat loss equations were also applicable to the elevated temperature operating conditions. A further explanation and verification of the use of this approach is given in section 6.3.

5.2 Heat transfer coefficient

The net heat transfer rate ($\dot{Q}$) into the fluid for the subsequent two-phase experiments was determined using the homogeneous equilibrium model. This model assumed all energy applied by the heated metal layer was either absorbed by the fluid or lost to the environment. The energy balance equation is shown in equation (5-7):

$$\dot{Q} = \dot{Q}_{ap} - \dot{Q}_{loss} \tag{5-7}$$

Here $\dot{Q}_{ap}$ was calculated using equation (5-3), and $\dot{Q}_{loss}$ was determined from equation (5-6), using the appropriate a and b values applicable to the particular rotation case under consideration. The amount of heat absorbed was represented as a heat flux, as shown in equation (5-8) during calculation of various other parameters.

$$\dot{q} = \frac{\dot{Q}}{W l_h} \tag{5-8}$$

Here the net heat flux ($\dot{q}$) was calculated using the net rate of energy absorbed from equation (5-7), the width (W) of the channel and the total heated length (l_h). The total heated length was subdivided

into several control volumes, which spanned the width of the channel, depth of the channel and a distance (Δl).

The infrared camera captured an image of the heated side of the channel, which spanned 25 pixels across the width of the channel and 400 pixels along the length of the channel. A control volume was the length of a single pixel, which was determined using the heated length (measured with a Vernier calliper) and the number of pixels along the length of the channel. A visual representation of the segmentation of the channel's heated length is shown in Figure 9.

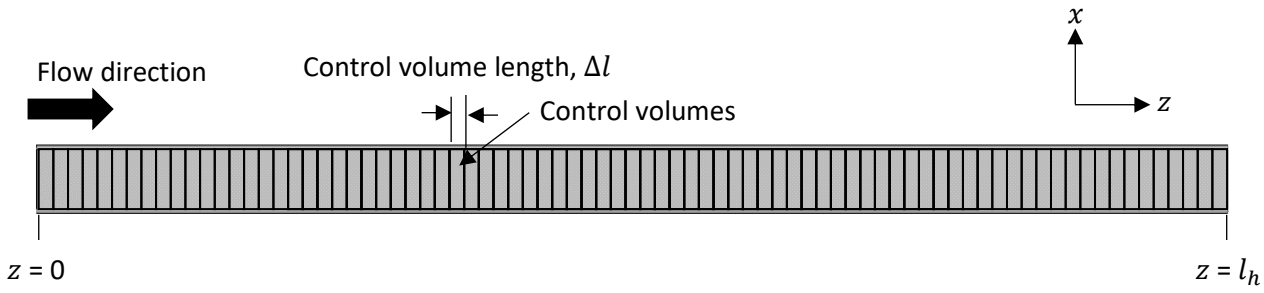

Figure 9: Control volumes used in analysis of local temperatures, heat transfer coefficients and surface temperature values

The control volumes represented were the entire width of the channel in the x direction, the entire depth of the channel (H) in the y direction and a distance Δl in the z direction. This approach allowed the creation of a local net heat flux ($\dot{q}_z$) specific to each control volume, with the time-averaged heat loss ($\dot{q}_{loss,z}$) based solely on the average surface temperature the control volume. The heat applied to the channel was assumed to be constant at all points on the heated surface. Hence, equation (5-3) for the total applied heat was converted to a flux using the same approach as that applied for heat loss – that is, using the surface area of a control volume. This method resulted in different heat losses in each control volume, with the same applied heat. The approach is shown in equation (5-6):

$$\dot{q}_z = \frac{\dot{Q}_{ap}}{W\Delta l} - \frac{\dot{Q}_{loss,z}}{W\Delta l} \tag{5-9}$$

In equation (5-9), the amount of heat lost based on the average surface temperature across the width of a control volume was converted to a heat flux using the surface area of a single control volume. The applied heat was converted to a flux using the surface area of the control volume.

Heat transfer coefficients were calculated for each control volume, producing local heat transfer coefficients (α_z). These were based on the net local heat flux presented in equation (5-10):

$$\alpha_z = \frac{\dot{q}_z}{(T_{s,z} - T_z)} \tag{5-10}$$

Here $T_{s,z}$ is the local heated surface temperature at the liquid–wall interface and T_z is the local bulk fluid temperature. The $T_{s,z}$ value was assumed to be the same as the outer heated wall temperature as measured by the infrared camera. This assumption was based on the small distance between the inner wetted surface of the channel and the heated external surface. The temperature difference across the wall thickness was neglected, and it was assumed that the local inner-wall temperature was equal to the local external heated wall temperature. This assumption was based on the Biot number, where a value of less than 1 suggests that the thermal gradient is negligible. It was calculated using equation (5-11).

$$Bi_z = \frac{\alpha_z}{k} t_w \tag{5-11}$$

The Biot number (Bi_z) was calculated with the local heat transfer coefficient (α_z), the thermal conductivity (k) of the borosilicate glass (which was 1.14 W/mK) and the characteristic length the thickness of the wall (t_w), 0.35 mm. Biot numbers were calculated at control volumes with the minimum and maximum heat transfer coefficient and ranged from 0.06 to 0.61. These values were all less than 1 suggesting thermal stratification through the heated wall was negligible. Thus, $T_{s,z}$ was determined via MATLAB as the arithmetic average of the infrared camera pixel temperature values for each control volume, shown in equation (5-12).

$$T_{s,z} = \frac{\sum_t^j \sum_x^i T_s(x_i, t_j)}{N_x N_t} \tag{5-12}$$

The term $T_{s,z}$ is the average surface temperature in a control volume, t is the temporal averaging, x is the spatial average in the x axis direction on the heated surface, T_s is the temperature measured by the infrared camera at a position x_i in time t_j, N_x is the number of temperature values across the channel in the x direction at one time step and N_t is the number of time steps taken during an experiment. The calculation produced a time-average local surface temperature unique to each control volume.

The local fluid temperature was also calculated in each control volume and averaged in time. It was assumed that the local bulk fluid temperature in a control volume remained the same. An analytical model written in MATLAB was used to calculate the local bulk fluid temperature using the following relationships, where z = 0 was the start of the heated length.

If in the liquid-phase ($T_{b,z} < T_{sat}$):

$$T_{b,z} = T_{in} + \frac{\dot{q}Wz}{\dot{m}c_p} \tag{5-13}$$

If in the two-phase region:

$$T_{b,z} = T_{sat} \tag{5-14}$$

The value of T_{sat} was determined using the time-averaged outlet temperature measured from the thermocouple and was cross-checked with the expected thermodynamic saturation temperature at atmospheric pressure. The inlet temperature (T_{in}) was determined from the thermocouple at the inlet to the channel and was also time averaged.

An image captured by the infrared camera had a size of 640 x 480 pixels. For the analysis of surface temperature, the infrared images were cropped to the size of the channel, with each image being a temperature matrix of approximately 400 x 25 pixels after cropping. The channel was not always exactly horizontal in the frame, resulting the top and bottom pixel locations changing between the inlet and the outlet. The slanted frame used in the analytical model only encompassed the surface temperatures on the heated surface, as shown in Figure 10.

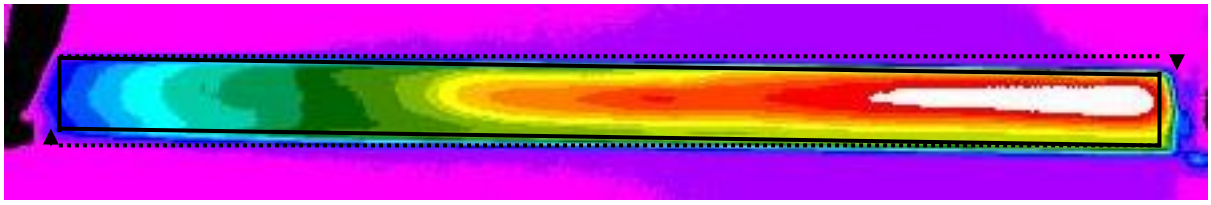

Figure 10: Infrared image with corrected frame

In Figure 10 the frame has been corrected both at the top and bottom of the microchannel, resulting in no temperatures off the microchannel's heated surface being used in calculations. Further surface temperature averaging is shown in Appendix B: Averaging infrared temperature values over time.

For validation purposes, spatially average surface temperatures were calculated to determine the average heat transfer coefficient in the two-phase region. The same approach to heat flux and the heat transfer coefficient was used where local heat transfer coefficients were created at all local control volumes. The time-average local vapour qualities were computed for each control volume, yielding a vapour quality associated with each control volume. All control volumes with a vapour quality of 0 or higher had their heat transfer coefficients incorporated in the calculation of an arithmetic mean.

5.3 Local vapour quality

Vapour quality was determined in the control volume as discussed previously. The vapour quality calculated was the time averaged vapour quality as transient vapour qualities along the length of the channel could not be accurately determined analytically. The thermodynamic state of the fluid entering the control volume was used as the reference vapour quality. The amount of energy absorbed by the fluid in that control volume was used to determine the change in vapour quality across the control volume.

The fluid entering the channel was subcooled with a vapour quality of less than 0. Hence, according to the definition, it was classified as having a negative vapour quality. The degree to which the system was subcooled was based on the amount of energy required to bring the bulk fluid's temperature to saturation conditions. Equation (5-1) was modified with the outlet temperature replaced with the saturation temperature:

$$\dot{Q} = \dot{m} c_p (T_{sat} - T_{in}) \tag{5-15}$$

This amount of energy required to reach saturation conditions was calculated using the time-average mass flow rate from equation (5-2), the specific heat of liquid FC-72 at the inlet temperature (averaged in time) from Table 4, the time-averaged inlet temperature (measured by the inlet thermocouple) and the saturation temperature. All two-phase experiments had heat fluxes initially applied that initiated flow boiling which resulted in the outlet quality being between 0 and 1, allowing the outlet thermocouple's temperature to be used as the saturation temperature. An initial subcooled vapour quality was then determined using the amount of energy required to raise the fluid to a saturation temperature and the latent heat of evaporation:

$$\chi_{z=0} = -\frac{\dot{m}c_p(T_{sat} - T_{in})}{\dot{m}h_{fg}} \tag{5-16}$$

In equation (5-16), the vapour quality at the inlet ($\chi_{z=0}$) was determined using the following terms: the single-phase change in energy required to reach saturation temperature; the mass flow rate, which was assumed to be constant at all points along the channel; and the latent heat of evaporation (h_{fg}). The latent heat of evaporation is the amount of energy (kJ/kg) required to convert one kilogram of a liquid to vapour. In all experimental test cases, the initial vapour quality was negative to a subcooling of approximately $\chi_{z=0}$ = -0.4.

From this initial condition of the system, the change in thermodynamic state could be calculated across each control volume. At least 400 local vapour qualities were calculated, based on the number of control volumes created by the infrared camera. The amount of energy absorbed in each control volume was based on average surface temperature of the control volume which significantly affected the amount of heat lost to the environment, directly impacting the amount of heat absorbed. The amount of heat absorbed was calculated using the net heat flux in equation (5-9), calculated locally in each control volume a distance z from the inlet. This heat flux was then converted to a net rate on the surface area of the control volume:

$$\dot{Q}_{net,z} = \dot{q}_{net,z}(W\Delta l) \tag{5-17}$$

This net amount of energy absorbed was then used to calculate the net change in thermodynamic quality across the control volume, which was assumed to the same in the entire cross-section of the channel. The vapour quality at the outlet of a control volume (χ_z) was determined using the inlet vapour quality from the previous control volume ($\chi_{z-\Delta l}$) and the net amount of heat absorbed in the control volume a distance z from the inlet. This analysis approach produced time-average local vapour qualities based along the length of the channel.

$$\chi_z = \chi_{z-\Delta l} + \frac{\dot{Q}_{net,z}}{\dot{m}h_{fg}} \tag{5-18}$$

The single-phase length was then determined analytically based on the location of χ_z = 0. The length of the single-phase region was calculated using the total heated length of the channel (l_h), the z position associated with the commencement of two-phase conditions ($z_{\chi=0}$), the z position that

corresponded to the inlet (z_{inlet}) and the total number of z locations between the inlet and the outlet (z_h).

$$l_{sp} = l_h \cdot \frac{z_{\chi=0} - z_{inlet}}{z_h} \tag{5-19}$$

The single-phase length (l_{sp}) is shown in the equation above as ranging from the inlet (z_{inlet}) to the point at which two-phase conditions were first found ($z_{\chi=0}$). This distance relative to the total distance between the inlet and outlet (z_h) was used in conjunction with the Vernier Calliper measured heated length to determine the single-phase length.

5.4 Cross-sectional surface temperature variability

Cross-sectional surface temperature ($\Delta T_{s,z}$) indicates the difference between the maximum and minimum surface temperature value in a control volume. This value was determined locally at all control volumes and at all time steps, as shown in (5-19).

$$\Delta T_{s,z} = T_{s,z,max} - T_{s,z,min} \tag{5-20}$$

The cross-sectional temperature was determined using the maximum surface temperature on the heated surface at a cross-section ($T_{s,z,max}$) and the minimum surface temperature on the heated surface at in a cross-section ($T_{s,z,min}$) at the same time step. These cross-sectional temperature differences were calculated at all control volumes at all time steps. The largest cross-sectional temperature at any location at any time step was then reported.

5.5 Uncertainty analysis

The uncertainty approach used in this study is discussed in detail in Appendix C: Uncertainty propagation. The bias and random error associated with each input parameter (measured directly by a device such as a thermocouple) were calculated using equation (4-4), shown discussed again in equation (5-20). This root of summed squares method was only applicable to parameters that were directly measured, such as temperature, pressure, voltage, current and length. The uncertainty calculated for these parameters was an absolute value with the same unit as the parameter (e.g., °C for thermocouples).

Each calculated quantity had an uncertainty that was one of two forms: an absolute uncertainty or a relative uncertainty. Calculated quantities, based on input parameters having the same unit, remained absolute uncertainties. An example is pressure drop, where the inlet and outlet pressure was the input parameters and the pressure drop was the calculated quantity, all with the same unit (kPa). Some calculated quantities – such as applied heat and vapour quality – were calculated with at least two input parameters that having different units from each other and from the calculated quantity, which produced a relative uncertainty with % unit. An example of the calculation of the absolute uncertainty of a pressure drop ($\epsilon_{\Delta P}$) is shown in equation (5-20).

$$\epsilon_{\Delta \mathrm{P}} = \sqrt{\epsilon_{\mathrm{P_{in}}}^2 + \epsilon_{\mathrm{P_{out}}}^2} \tag{5-21}$$

Here, the absolute uncertainty is calculated based on the absolute uncertainty of the inlet pressure transducer ($\epsilon_{P_{in}}$) and the outlet pressure transducer ($\epsilon_{P_{out}}$). The absolute uncertainty was calculated using the root of the summed squares of the uncertainty of each transducer, due to the form of the pressure-drop calculation where one quantity is subtracted from the other. The equation used to calculate the uncertainty depends on the form of the equations. If the input parameters were multiplied or divided, for example, the equation would require a different method of calculation [212], see Appendix C: Uncertainty propagation. Absolute uncertainties can be converted into relative uncertainties using the absolute uncertainty of an input parameter or quantity and the typical value that was calculated:

$$\sigma_{\Delta \mathrm{P}} = \frac{\epsilon_{\Delta \mathrm{P}}}{\Delta P} \tag{5-22}$$

Here, the relative uncertainty of the pressure drop ($\sigma_{\Delta \mathrm{P}}$) is calculated using the absolute uncertainty and the typical pressure-drop reading (ΔP). This relative uncertainty can be either a maximum or a minimum value, depending on the denominator chosen. A larger reading produces the minimum relative error, and the lowest typical pressure drop produces the maximum relative error.

An uncertainty propagation for the heat transfer coefficient as well as other calculated parameters can be found in **Appendix D: Error propagation**. Here the propagation of an error from input parameter to the calculated quantity is shown. The uncertainties of each input parameter and calculated quantity are summarised in Table 6, which lists the minimum absolute uncertainties and the minimum relative uncertainties.

Table 6: Absolute uncertainties of the input parameters

Parameter	Minimum relative error	Minimum absolute error
Thermocouple temperature (T)		± 0.14°C
Saturation temperature (T_{sat})		± 0.14°C
Infrared camera temperate (T_w)		± 2°C (factory uncertainty)
Channel length (l)		± 0.02 mm
Channel internal width (W)		± 0.02 mm
Channel internal height (H)		± 0.02 mm
Local distance from inlet (z)		± 0.09 mm
Rotational orientation (α)		± 1°
Liquid density (ρ_l)		± 0.37 kg/m^3
Pressure (P)		± 93 Pa
Heat absorbed ($\dot{Q}$)	$\pm$ 2.48%	± 0.16 W
Voltage (U)	±0.63%	± 0.15 V
Current (I)	±1.23%	± 0.53 mA
Heat flux ($\dot{q}$)	2.48%	± 0.17 kW/m^2
Heat transfer coefficient (α)	2.8%-6.2%	± 7 W/m^{2}K to 35 W/m^{2}K
Volumetric flow rate ($\dot{V}$)	1%	± 2 mL/hr
Mass flux (G)	4.5%	± 0.16 kg/m^{2}s
Vapour quality (χ)	3%	

In the case where a relative uncertainty was determined a minimum absolute uncertainty was provided.

5.6 Chapter summary

The heat lost from the system was calculated based on single-phase experiments. These were critical to the calculation of the local fluid temperature, heat transfer coefficient and local vapour quality. Rotational effects were further investigated using cross-sectional temperature variations. The absolute and relative uncertainty of the input parameters and calculated quantities was also presented.

6. Experimental heat transfer analysis: rotation

This chapter presents the experimental results for a horizontal channel at different rotational orientations (θ). First, the experimental setup is validated by comparing some of the results to findings reported in literature. This is followed by flow visualisation to identify the typical flow patterns associated with the two-phase boiling and the location of nucleation sites, as well as the degree to which the vapour component of the flow was confined. Heated surface temperature profiles are presented, showing how the average cross-sectional temperature changes along the length of the channel. Variations in the cross-sectional temperature are also investigated. Local heat transfer coefficients are discussed at corresponding axial local vapour qualities. The chapter ends with a discussion about typical pressure-drop results at various rotations and mass fluxes. Rotation, mass flux and heat flux effects are investigated where possible.

6.1 Experimental validation

Validation of the experimental setup, test procedure and data-analysis methods was challenging. The reason was that reference data for a microchannel having the same characteristics as those used in this study was not available (i.e., internal cross-section of 5 mm x 0.5 mm; circumferentially non-uniformly heating; FC-72 used as the working fluid at low mass fluxes of 10 kg/m^{2}s, 20 kg/m^{2}s and 40 kg/m^{2}s). Deionised water has been used in published studies with similar system parameters. However, in the current study it could not be used as its saturation temperature is higher than the melting temperature of the epoxy used in the test section, at atmospheric conditions (101 kPa).

Microchannels of a similar size (6 mm x 0.3 mm) were investigated by Wang, et al. [163] with uniform circumferential ohmic heating. They reported the average heat transfer coefficients on the entire heated surface at a mass flux of 44 kg/m^{2}s, at various heat fluxes. They used the same fluid and data collection method as in the current study and similarly based their results on measurements from thermocouples, pressure transducers, an infrared camera and high-speed camera. Because of these similarities, the method and data analysis used in the current study were validated by creating a test section having the same specifications as those used by Wang, et al. [163]. Their data is compared in Figure 11 with data reproduced and analysed using the experimental set-up of the current study.

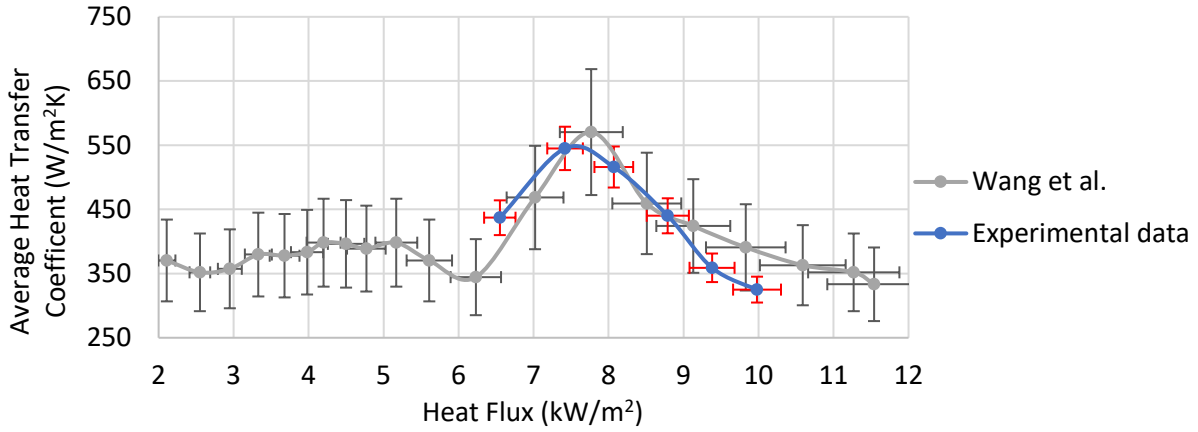

Figure 11: Validation curve for experimental setup, bottom-heated (θ = 0°) at mass flux of 44 kg/m²s and various heat fluxes

It should be noted that the uncertainties in the current study (shown in red) were smaller than those reported in the reference study (in black). Both datasets indicated that a maximised average heat transfer coefficient exists at a heat flux of approximately 7.5 kW/m^2. There were several cases where near exact agreement between the two datasets was found. In general, the data produced in the current study fell within the uncertainty band of the reference set. Based on the agreement between the two data sets, it was concluded that the current experimental setup – with the associated data-reduction methods – produced accurate and repeatable results.

6.2 Experimental Repeatability

To assess the repeatability of the results from this study each experiment was repeated 3 times. In this section a single mass flux and heat flux case at each rotation is presented with the sole purpose of determining the repeatability of the results. Errors bars for the heat transfer coefficient are a relative uncertainty of between 2.8% and 6.2%.

In general, variations observed occurred in regions where the flow behaviour was variable. Two-phase flows are susceptible to flow instability which was observed in two forms in this study. The first is vapour motion towards the inlet called reverse flow. The second was mixing of the liquid and vapour phase in the two-phase region which presented as turbulent flow which presents like churn flow. The instability events were cyclic in nature decreased the surface temperature on the heated wall. The amount of surface cooling was dependent on the intensity of the flow instability, for instance, how far the vapour moved towards the inlet during a reverse flow.

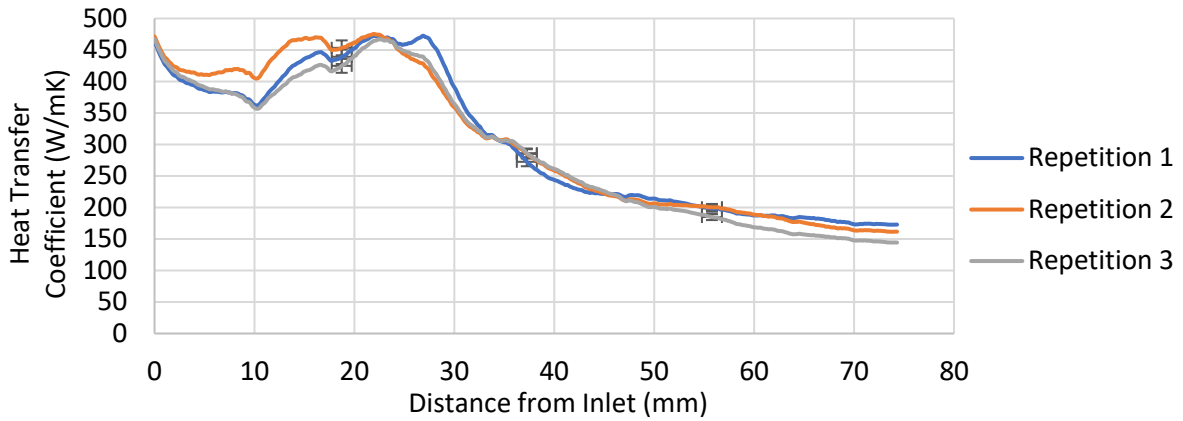

Figure 12: Repeatability testing at a rotation of θ = 0°, mass flux of 10 kg/m²s and heat flux of 4.3 kW/m²

The heat transfer coefficients at a rotation of θ = 0° was larger than at other rotations with an average difference between the highest and lowest heat transfer coefficient at a location of 23.4 W/mK or 8.6 %. In most axial positions the difference in the heat transfer coefficient were within the uncertainty of the measurement. Between 5 mm and 15 mm from the inlet, repetition 2 had a heat transfer coefficient that was up to 49 W/mK higher than repetition 1 and 3. This is attributed to transient flow instability being more intense in this period than at repetition 1 and 3, specifically reverse flow. Similarly, repetition 1 had a heat transfer coefficient that was up to 45 W/mK higher than repetition 2 and 3 between 25 mm and 30 mm from the inlet. This large deviation is also attributed to transient flow instability, specifically two-phase mixing. When comparing the heat transfer coefficients in this case to other rotations, repetition 3 would be chosen for comparison. This is because repetition 3 had good agreement with at least one other repetition at all times.

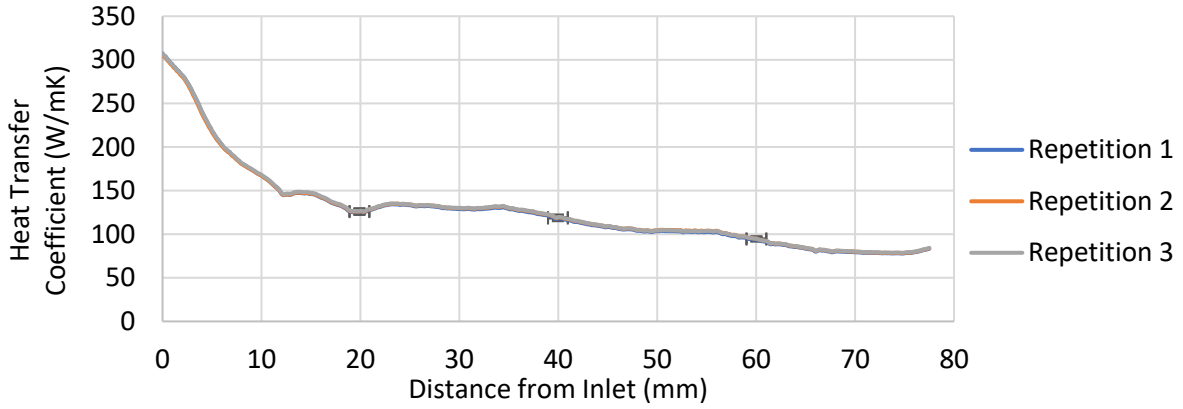

Figure 13: Repeatability testing at a rotation of θ = 30°, mass flux of 10 kg/m²s and heat flux of 4.6 kW/m²

The heat transfer coefficients at all axial positions between the inlet and the outlet are near identical at all repetitions at a rotation θ = 30°. The average difference between the highest and lowest heat transfer coefficient at a location was 1.2 W/mK or 1 %. This high level of agreement was due to two main factors, the first was minimal flow instability and secondly the nucleation sites had little effect on the flow behaviour.

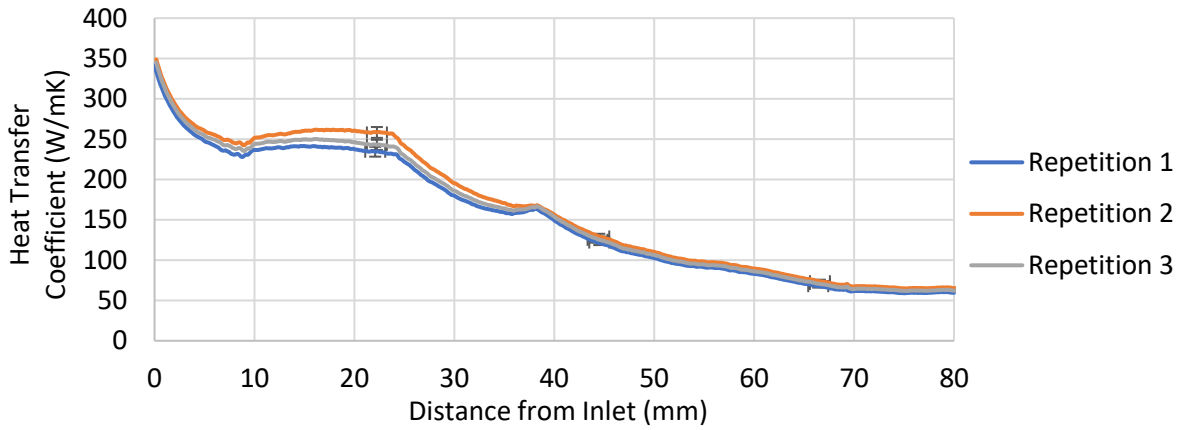

Figure 14: Repeatability testing at a rotation of θ = 60° mass flux of 10 kg/m²s and heat flux of 4.5 kW/m²

At a rotation of 60° good agreement was found between the three repetitions with an average difference between the highest and lowest heat transfer coefficient at a location was 10 W/mK or 7 %. A deviation of the heat transfer coefficient at around 22 mm is large compared to the other axial positions at 24 W/mK. This deviation between the repetitions is within the uncertainty range of the measurement. The good agreement is attributed to little flow instability and a nucleation site with less bubble nucleation, growth and detachment.

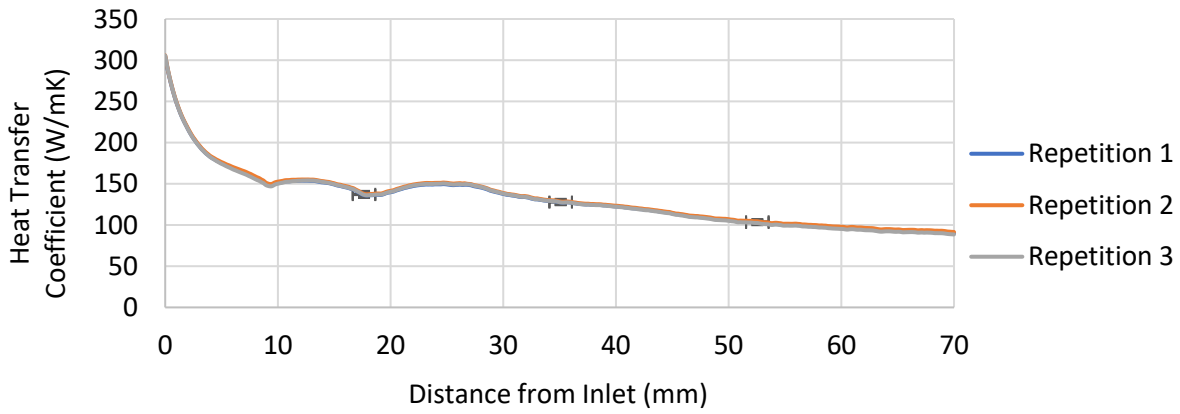

Figure 15: Repeatability testing at a rotation of θ = 90°, mass flux of 10 kg/m²s and heat flux of 4.4 kW/m²

At a rotation of θ = 90°, the heat transfer coefficients at all axial positions between the inlet and the outlet are near identical at all repetitions. The average difference between the highest and lowest heat transfer coefficient at a location was 1.9 W/mK or 1.6 %. No flow instability was observed, and the nucleation site did not have nucleating bubbles growing and detaching resulting in little transient variation.

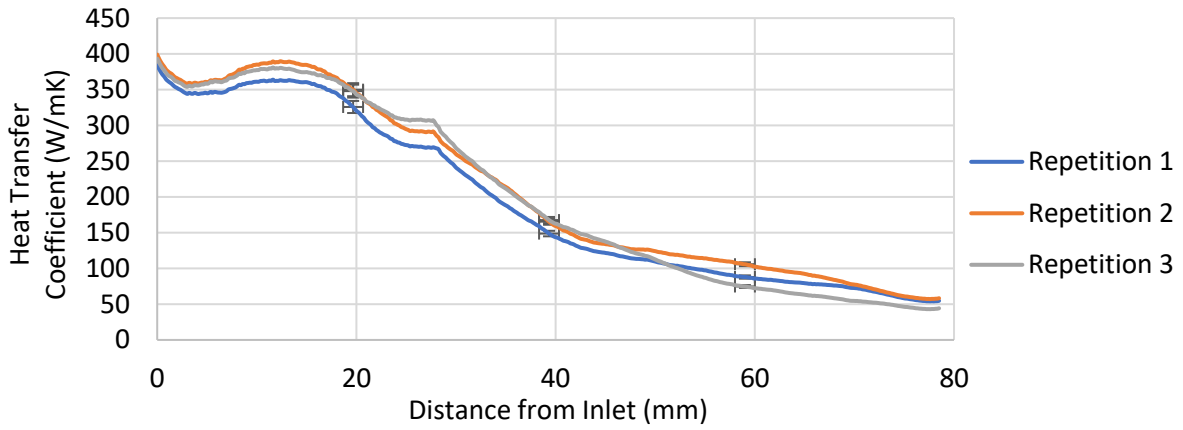

Figure 16: Repeatability testing at a rotation of θ = 180°, mass flux of 10 kg/m²s and heat flux of 4.4 kW/m²

The agreement between the repetitions at a rotation of θ = 180° is poor compared to the other rotations. The average difference between the highest and lowest heat transfer coefficient at a location was 22.9 W/mK or 16 %. The errors bars at 20 mm and 40 mm from the inlet are within the uncertainty of the measurement. At approximately 60mm from the inlet a difference of 30 W/mK is observed which is greater than the uncertainty of the measurement. The reasons for this variability is due to the flow instability which could have periods of up to 20 s which means the time averaged value could result in different quasi-steady-state heat transfer coefficients.

In all the cases presented good agreement is shown between each repetition with the variability within the error range for the measurement.

The heat flux associated with the commencement of two-phase flow was also consistent. Each experimental mass flux, and rotation would have two-phase conditions commence at the same heat flux. On occasion the fluid had to be slightly super-heated prior to a nucleation site becoming active. When this was the case the heat flux was then decreased to the heat flux which previously resulted in the commencement with two-phase conditions. If the heating was decreased below this level two-phase conditions would cease

6.3 Single-phase experiments - validation

The single-phase experiments described in section 5.1 are now discussed in this section. The energy balance approach used in this section required due to the literature review in section 2.6 not producing an appropriate heat loss equation for natural convection away from the single-sided heating of a microchannel with a uniform heat flux. Similarly, section 2.5 an appropriate internal forced convection Nusselt number was not obtained although an approximate value might be discernible.

An important non-dimensional number to establish for natural convection heat loss equations is the Raleigh number, as was discussed in section 2.6. The Rayleigh number (Ra) calculation is presented in Table 7 at two temperatures. The first is a typical surface temperature observed in the single-phase tests (40°C) and the maximum surface temperature measured during the two-phase tests (150°C).

Table 7: Fluid properties used in the calculation of Gr, Pr and Ra

Property	Single-phase values	Maximum value
T_∞ (°C)	24.5°C	
T_s (°C)	40°C	150°C
Temperature for air properties (°C)	32.25	87.25
g (m^2/s)	9.81	
β (1/K)	0.00327	0.00277
Lc (m)	9.4μm	
k (W/mK)	0.02588	0.03024
ν (m^2/s)	1.608×10^{-5}	2.201×10^{-5}
α (m^2/s)	2.208×10^{-5}	3.086×10^{-5}
$\boldsymbol{Gr}$	**1605**	**5878**
$\boldsymbol{Pr}$	**0.72**	**0.72**
$\boldsymbol{Ra}$	**1169**	**4193**

From the table it can be observed that the Pr number is within an expected value of 0.72. The Gr number on the other hand is extremely low which results in Ra numbers are also comparably low. The reason they are so low is due to the characteristic length which for a plate heated from below which was four times the surface area divided by the perimeter. This single side heated channel had a characteristic length that became extremely small when cubed. The Ra number thus did not change substantially between single-phase tests and the two-phase tests ranging between 1100 and 4200. This small change in the Ra number indicates that the Nusselt number would not change substantially

between the coldest and hottest portions of the channel. This observation suggests that the single-phase heat loss equations would be appropriate in the two-phase region.

Verifying the amount of heat lost from the bottom heated surface often requires two main assumptions. The first is with regards to the geometry of the heated surface and the second is with the type of heating. The first type of geometric assumption is that the plate is large. This means that the effect of heat loss from conduction through the channel's material and convected form the unheated side is negligible compared to the heated surface. The second type of geometric assumption is that the plate is an infinite strip. This is not valid as the length of the channel is only 16 times longer than it is wide. The type of heating is either isothermal conditions or a uniform heat flux condition. An isothermal equation would not be appropriate as the heating in this case was a uniform heat flux. The uniform heat flux cases typically are used for pipes or square channels heated on all sides. Most experimental investigations of bottom heated channels don't require a natural convection correlation to be used as the heating blocking cases have a different method for determining the heat lost.

In all cases where the channel is heated from below a set of single-phase equations are created with the heat lost to the environment calculated from an energy balance of the heat absorbed and heat lost to find the heat lost [206-211].

Heat loss % were not presented as the absolute heat losses used in the analytical model were absolute values rather than percentages. In this study the heat loss percentages ranged from 17% to approximately 32% in the single-phase tests depending on the surface temperature and rotational orientation. The maximum heat loss was in the two-phase region where the surface temperature had reached 150°C and only vapour was in contact with the heated wall. At this point most of the heat was lost to the environment with a heat loss of up to 75%. The Rayleigh number range of these tests were also small, suggesting that a Natural convection flow regime change was not a factor affecting the heat loss rate in the two-phase region.

Validation of the heat transfer in the single-phase region was also not directly possible due to the type of heating applied, channel geometry and mass flux. The internal forced convection Nusselt number required for validation had to be a high-aspect ratio rectangular channel at rotations from horizontal heated below to horizontal heated from above, with a uniform heat flux boundary condition on one

side only, using FC-72, at Pr = 12.3 and $14 \leq Re \leq 57$. A correlation for these test conditions was not found.

A rectangular channel with an aspect ratio of 10, Reynolds numbers of 14, 28 and 57 could have the expected Nusselt number for the internal forced convection determined using equation 1-17. This equation requires a Reynolds number between 20 and 2000 and an aspect ratio between 0 and 20 and a uniform heat flux on three sides. The Nusselt numbers were calculated to be 6.4, 6.2 and 6.1, for each Reynolds number case. This correlation had an accuracy of 13% which resulted in an error of 0.83.

The single-phase experiments of a bottom heated channel had an average Nusselt number of 4.2. This means that the Nusselt number for the single side heated case was 2 less than the three-side heated case. It is possible that this would be appropriate.

In the absence of a correlation to use, the results from the single-phase experiments were assumed to be accurate. This was based on the observed internal forced convection Nusselt number having a value in the order of magnitude that would be expected. Secondly, the Rayleigh number on the heated surface between the single-phase tests and the two-phase tests did not vary substantially.

6.4 Initial observations

This section investigates the flow patterns observed during two-phase boiling of horizontal channels (θ = 0° and 180°) and rotated channels (θ = 30°, 60° and 90°). High-speed images are used to visually identify the flow patterns, and infrared images are used to demonstrate the effect of vapour location on the heated surface's temperature. The nucleation site location at various heat fluxes and mass fluxes is presented using the high-speed and time-averaged local vapour quality calculations.

6.4.1 Axial profiles (influence of rotation and heat flux)

Surface temperature profiles are useful in heat transfer analysis as they give a first-order approximation of the relative heat transfer performance of the system. In the single-phase region, a rapid increase in the surface temperature accompanied by a short distance between the nucleation site and the inlet is indicative of a high heat transfer coefficient.

In the two-phase region, rotations that had surface temperatures relatively close to the saturation temperature of the fluid had relatively high heat transfer coefficients. That is, when the same heating load was applied to the wall, a smaller portion of the heating load was lost to the environment and the rest was absorbed by the fluid. Regions with poor heat transfer were unable to effectively remove heat from the heated wall and increase the vapour quality of the fluid. As a result, the heat increased the heated wall's surface temperature, and more energy was lost to the environment.

Bubble dynamics were observed on the heated surface with dynamic changes in the hot and cold surface temperatures, indicative of bubble motion on the heated wall. Bubble motion on the heated wall is observed as a moving hotspot with the approximate shape of the vapour bubble, surrounded by relatively colder surface temperatures. Axial positions with a high surface temperature relative to the wall upstream and downstream can decrease the adjacent surface temperature due to bubble motion in the cross-sectional direction, for example, away from the heated wall.

The impact of rotation on the axial surface temperature profiles was investigated at rotations of θ = 0°, 90° and 180° at a mass flux of 40 kg/m^{2}s and heat flux of 14 kW/m^2. All rotational cases presented have a high-speed and infrared image corresponding to the same point in time. The surface temperature profile is the average surface temperature in each cross-section along the axial length of the channel and is averaged in time.

The first case presented in Figure 17 is a channel at a rotation of θ = 0° at quasi-steady state conditions. Flow occurs from left to right. Points and regions of interest are indicated on the figure, such as the liquid region, nucleation site, detached bubble, partial confinement region, confinement region and the vapour slug.

In Figure 17, the time and cross-section average surface temperature at all axial positions is presented. A gradual increase in the surface temperature was observed, with the rate of increase in surface temperature decreasing closer to the nucleation site. At the nucleation site, a wall superheat of at least 6°C and up to 18°C in a single pixel was observed. The local maximum surface temperature was found at the centre of the horizontal channel, with the nucleation site found at approximately the same location, as seen in the high-speed image. It is thus concluded that the location of the maximum wall superheat is a strong indicator of the location of the nucleation site.

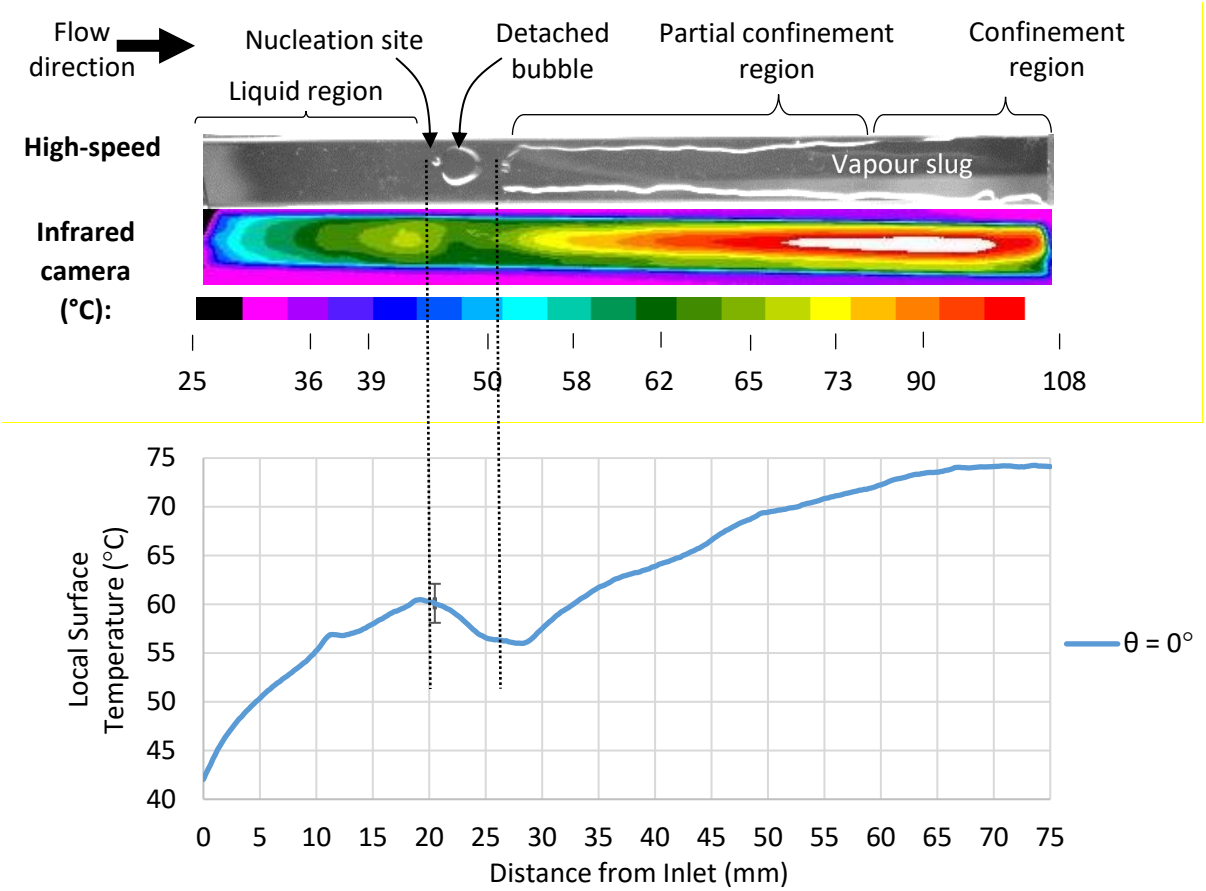

Figure 17: Typical two-phase infrared, high-speed and average surface temperature representations for θ = 0° at a heat flux of 14 kW/m² and mass flux of 40 kg/m²s

Complete bubble detachment produced a decrease in the heated surface temperature. The decrease in the heated surface temperature was due to the increased localised vapour motion in the transverse direction due to bubble motion from the nucleation site. The buoyancy assisted flow allowed the vapour in contact with the heated surface to be replaced by liquid. This is important, as the liquid FC-72 had a thermal conductivity that was higher than vapour FC-72, further assisting in a high local heat transfer coefficient to be attained.

Surface temperatures remained approximately constant between 25 mm and 28 mm from the inlet. The steady increase seen between 28 mm from the inlet and the outlet was due to the formation of a large vapour column. The formation of the vapour column occurred in the partial confinement region where the bubble grew but did not have its shape influence by the channel's geometry. Vapour was present in the centre of the channel and liquid occurred at the extremes of the width of channel. This created a symmetrical thermal gradient due to the symmetric form of the vapour slug.

As the vapour slug continued to grow, the channel's geometry impacted the shape of the slug by forcing it to grow in the depth of the channel rather than the width. This was the confinement region where the maximum surface temperature occurred and was located along the centre line of the channel. The maximum surface temperature was found close to the exit as the portion of the channel that was filled with vapour was greatest. The vapour quality at the outlet was larger than the rest of the channel resulting in less high heat transfer liquid available to remove heat from the heated surface, resulting in a decreased rate of heat transfer from the wall and in turn an increased surface temperature.

Figure 18 represents a channel at a rotation of θ = 90°, tested at a mass flux of 40 kg/m^{2}s and heat flux of 14 kW/m^2. The nucleation site cannot be clearly located as the vapour had moved to the top of the channel, with the nucleation site located at the liquid-vapour boundary. The liquid region, vapour slug front and vapour slug are shown. The vapour slug is fully confined in the depth of the channel.

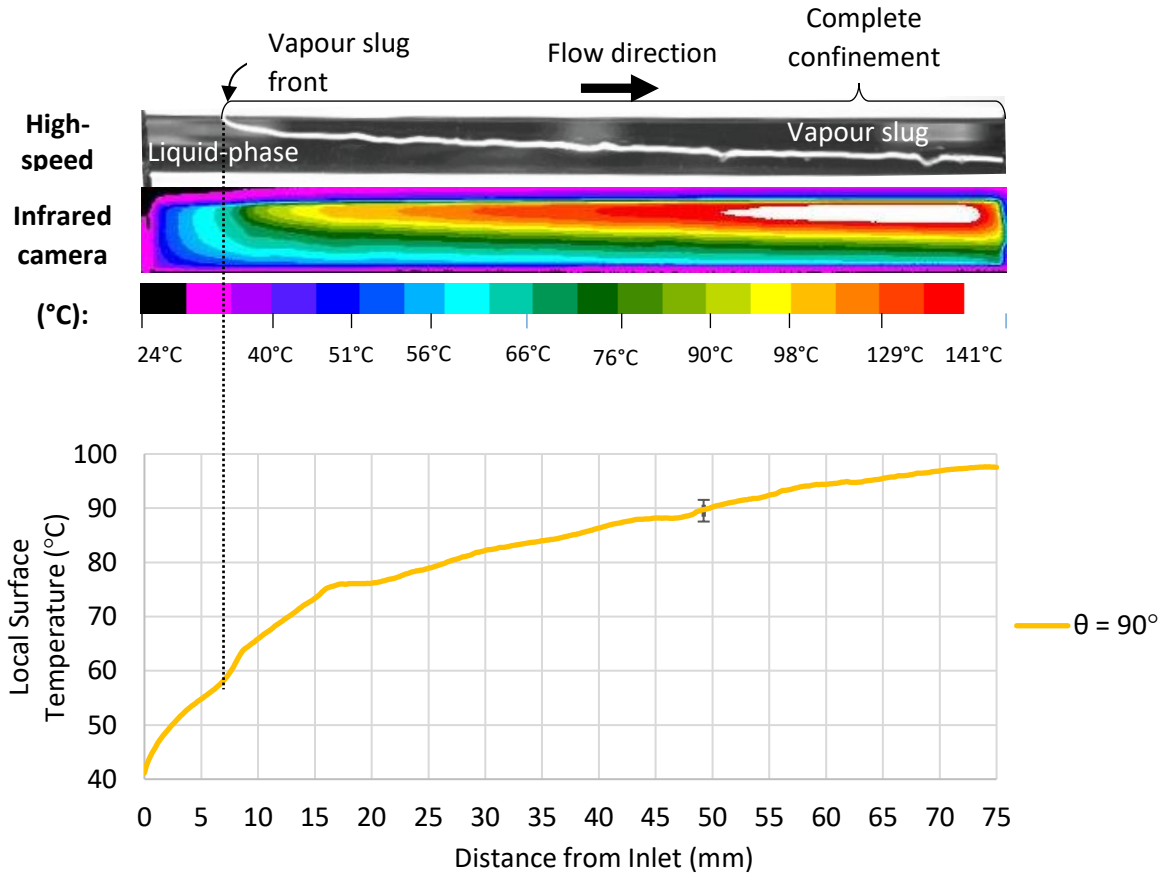

Figure 18: Typical two-phase boiling represented with high-speed and infrared image; average surface temperature plot with a channel at θ = 90°; mass flux 40 kg/m^{2}s and heat flux of 14 kW/m^2

From Figure 18, the surface temperature profile is observed to increase continually between the inlet and the outlet. The rate at which the surface temperature increases between the inlet and a point

roughly 7.5 mm from the inlet slowed until the vapour front of the slug was reached. Thereafter, the surface temperature continued to increase at a constant rate. The surface temperature then continued to increase at an ever-slower rate from 18 mm from the inlet, reaching a maximum temperature at the outlet of around 98°C.

At θ = 90°, no decrease was observed in the temperature profile, unlike what was observed at a rotation of θ = 0°. A decrease in the surface temperature was not observed because the nucleation site did not produce bubbles which detached from the heated surface producing secondary flow effects. The nucleation site could also not be clearly identifiable and was presumed to be at the liquid-vapour interface. These key observations significantly impacted the heat transfer coefficient and was typical of all rotated channels.

The bubble position, as shown in the high-speed image, is at the top of the channel and is fully confined in the depth of the channel. As heating continues, the bubble continues to grow towards the bottom of the channel, the width. A maximum wall temperature is measured at the top of the channel where the bubble is confined and complete dryout is assumed to have occurred. An asymmetric thermal gradient is observed across the width of the channel due to discrete large portions of the channel being filled by both vapour (low heat transfer) and liquid (high heat transfer).

A channel at a rotation of θ = 180° is represented in Figure 19. This test case had a mass flux of 40 kg/m^{2}s and heat flux of 14 kW/m^2. A high-speed and infrared image of the channel is shown, with the local surface temperature averaged across a cross-section shown in profile. In the high-speed image, the following elements are indicated: liquid-phase, nucleation site, partial confinement region and complete confinement region.

Figure 19 shows that when θ = 180°, there was a steady increase in the average surface temperature in the liquid-phase region up to 20 mm from the inlet. At 20 mm from the inlet, nucleation occurred. Between 20 mm and 30 mm, the heated surface temperature plateaued at a constant 65°C, during which time the bubble growth occurred, and a large vapour slug formed. An accelerated increase in the heated surface temperature occurred between 45 mm and 50 mm from the inlet. The surface temperature then increased at an ever-decreasing rate up to the exit.

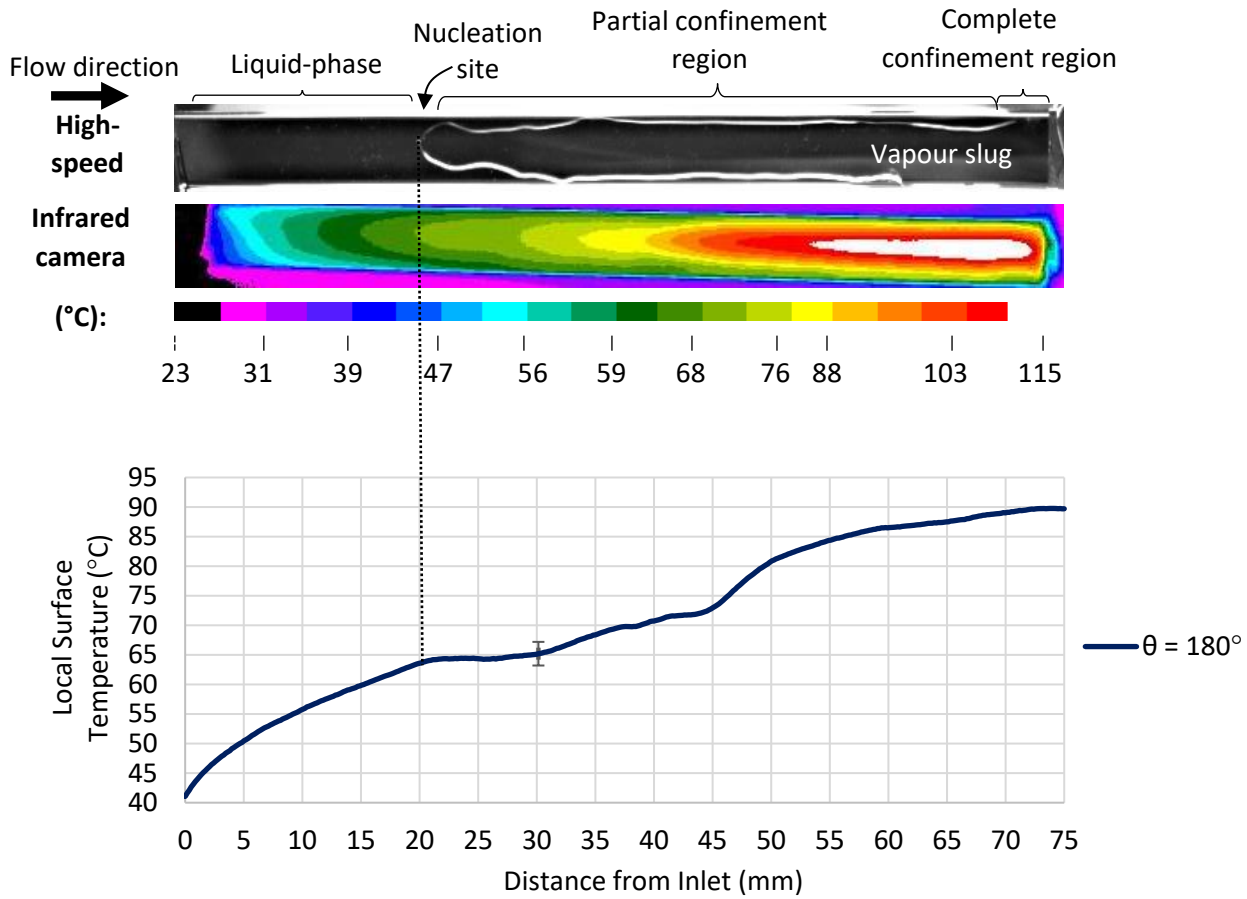

Figure 19: Typical two-phase boiling represented with an infrared, high-speed image and average surface temperature plot for a top-heated channel (θ = 180°) at a mass flux of 40 kg/m^{2}s and heat flux of 14 kW/m^2

From the high-speed image, it is observed that the nucleation site did not produce a clear bubble that detached, grew, and attached to the main vapour slug. This is an important observation as the detachment and vapour motion resulted in the surface temperature decreasing between the nucleation site and the vapour slug (rotation θ = 0°). Instead, the vapour slug appeared to be attached to the nucleation site on the heated wall and the vapour slid away.

Between 20 mm and 30 mm, in the region where the surface temperature plateaued, the bubble dynamics are worth noting. The vapour slug spread to 90% of the channel's width, then decreased in width at 30 mm from the inlet to approximately 70%. This would increase the portion of the heated wall entirely in contact with liquid, allowing the surface temperature to remain low. It is important to remember that the surface temperatures are averaged in time and the high-speed image is a representative image showing a single moment from a set of more than 6000 images. Hence, the simple observation of a bubble width is insufficient to explain the plateau.

At 30 mm from the inlet, the vapour slug was spread over most of the width of the channel. Presumably, as heating continued, the vapour slug grew in the depth of the channel and was not yet fully confined. This growth produces a region on the heated surface where the vapour's temperature may increase to superheated temperatures, driving an increase in the heated wall's surface temperature.

45mm from the inlet, the bubble became confined and dryout occurred. It was suspected that prior to this point, a liquid film was in contact with the heated wall and had evaporated. The liquid was replaced by vapour, which had a lower heat transfer coefficient due to its thermal conductivity being lower, which resulted in the higher surface temperatures.

A symmetric surface temperature profile was observed about the centre line of the channel. The maximum surface temperature was reached close to the exit and along the centre line. This temperature profile is indicative of an even distribution of vapour along the heated wall.

A direct comparison between the channels at rotations of θ = 0°, 90° and 180° is now presented. All three cases presented previously were at the same mass flux and heat flux. The surface temperature profiles are compared in Figure 20, with the cross-sectional average surface temperature calculated at all axial points; the temperatures were also averaged in time. The figure allows for direct comparison.

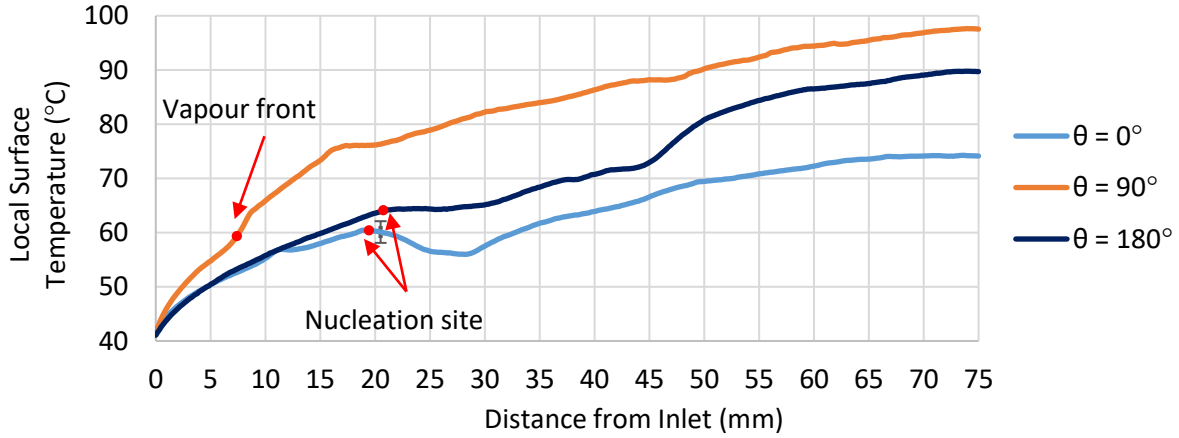

Figure 20: Surface temperature comparison of channels at rotations of θ = 0°, 90° and 180° at mass fluxes of 40 kg/m²s and heat flux 14 kW/m²

The single-phase region's temperature profiles were similar at all rotations. The surface temperature increased between the inlet and the point at which nucleation occurred or where the vapour front

was located. θ = 90° had a higher surface temperature in the single-phase region than θ = 0° and 180°. This was primarily due to a lack flow instability. Flow instability was not quantitively analysed in this study, but the effect of flow instability was observed to decrease the surface temperature. This decrease in surface temperature was attributed the buoyancy assisted cooling that resulted where the tangential velocity of the liquid and vapour was increased due to reverse flow and turbulent two-phase mixing. θ = 90° experienced the most stable flow behaviour of all rotations tested with near negligible flow instability observed, while θ = 0° and 180° experienced the most unstable flow behaviour.

The nucleation sites were at 19 mm, 7.5 mm, and 21 mm from the inlet for θ = 0°, 90° and 180° respectively. The horizontal channels displayed indistinguishable surface temperatures up to roughly 11 mm, when the effect of the bubble dynamics around the nucleation site started to affect the surface temperature. At a rotation of θ = 90°, the surface temperature 5 mm from the inlet was 5°C higher than was the case for either θ = 0° or 180°. This temperature difference grew to 17°C and 25°C at 30 mm from the inlet, compared to θ = 0° and 180° respectively.

At the point of nucleation, the wall superheat was 6°C and 8°C for channels at a rotation of θ = 0° and 180° respectively. The wall superheat at θ = 90° was difficult to determine as the exact location of the nucleation site was not known. A lower wall superheat is suggestive of a higher heat transfer coefficient at that point. The energy supplied was absorbed by the fluid to produce a nucleation site rather than being absorbed by the wall. Superheated wall temperatures at the point of nucleation are not of interest to experimental studies but are sought after in computational fluid dynamics investigations.

In the two-phase region, the surface temperatures of the horizontal channels continued to diverge, with θ = 180° measuring up to 15°C more than θ = 0°. The θ = 90° rotation continued to display increasingly slower surface temperature increases closer to the system exit. The θ = 90° rotation produce the highest surface temperatures at all positions. The θ = 180° case yielded a rapid incline in surface temperature at 45 mm to 50 mm from the inlet. This incline reduced the surface temperature difference between θ = 90° and 180° to a minimum of 9°C in the two-phase region. The maximum surface temperature in a single infrared pixel were approximately 108°C, 115°C and 141°C for channels at rotations of θ = 0°, 90° and 180° respectively.

The differences in surface temperature produced were the result of bubble dynamics around the nucleation site, the vapour slug's settling location and the prevalence of superheated vapour in the vapour slug. The θ = 0° case was heated from below, allowing the vapour formed at the nucleation site to detach and settle away from the heated surface. Complete confinement occurred only at vapour qualities near the exit of the channel.

The θ = 90° case produced higher average surface temperatures, despite a smaller portion of the heated surface being in contact with the vapour slug. The high temperatures resulted from the dryout that occurred on the heated wall due to complete confinement. It is expected that a small portion of the vapour in the vapour slug was at superheated temperatures. The horizontal channels displayed a vapour slug that was thinner than that of the θ = 90° channel, decreasing the chances of superheated vapour forming.

The θ = 180° case was heated from above and showed no bubble detachment or vapour motion away from the heated surface. Heating from above resulted in the vapour slug forming on and settling on the heated surface. This settling location produced higher surface temperatures than was the case for θ = 0°, as vapour was either directly in contact with the heated wall or separated by a thin liquid film. Vapour confinement occurred at 45 mm to 50 mm from the inlet, increasing the surface temperature.

Figure 21 presents the effect of heat flux on surface temperature profile at a rotation of θ = 0° and mass flux of 40 kg/m^{2}s. The surface temperatures shown for each heat flux were averaged in each cross-section and in time. The nucleation site at each heat flux is indicated.

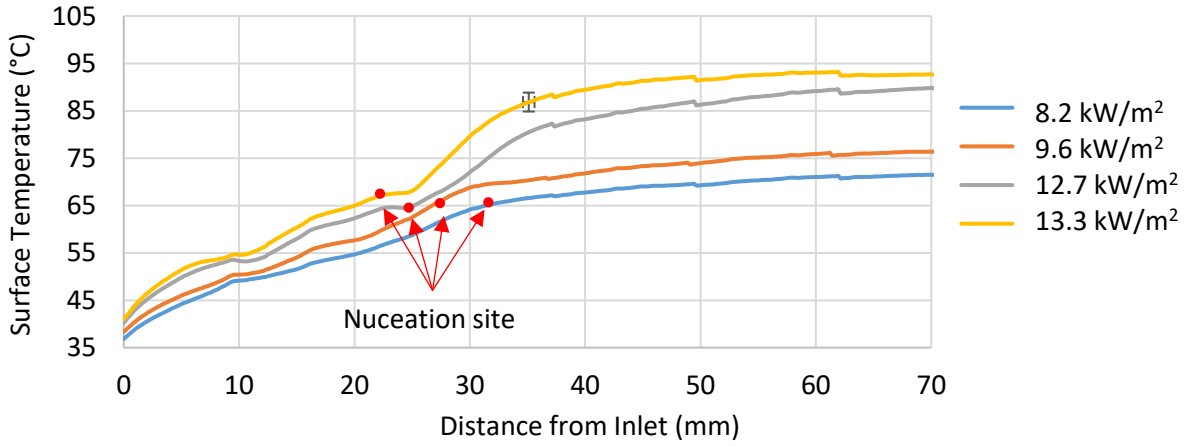

Figure 21: Heat flux effect on surface temperature of channels at a rotation of θ = 0° at a mass flux of 40 kg/m²s and heat fluxes of 8.2 kW/m², 9.6 kW/m², 12.7 kW/m² and 13.3 kW/m²

From Figure 21, the location of the nucleation site and the surface temperature profile can be observed to be influenced by the magnitude of the effective heat flux. In the single-phase region, between the inlet and the nucleation site, a similar surface temperature profile was observed at all heat fluxes. The inlet fluid temperature was the same at each heat flux, but the surface temperature 1 mm from the inlet was up to 3°C higher at 13.3 kW/m^2 than at 8.3 kW/m^2. The surface temperature between the inlet and 10 mm increased at a similar rate at each heat flux. Between 10 mm from the inlet and the nucleation site, the rate at which the surface temperature increased was nearly identical for all heat fluxes. The nucleation site was located where the average cross-sectional temperature was approximately 65°C. The wall superheat at a heat flux of 13.3 kW/m^2 was the only exception, at 67°C.

In the two-phase region, from the nucleation site to the outlet, the surface temperature continued to increase. The maximum temperature occurred at the outlet of the channel, where the highest vapour quality was found. The temperatures were 15.5°C, 20.4°C, 33.8°C and 36.7°C above the saturation temperature, at heat fluxes of 8.2 kW/m^2, 9.6 kW/m^2, 12.7 kW/m^2 and 13.3 kW/m^2, respectively.

After nucleation occurred, no notable decrease in the surface temperature was observed, contrary to the observations in Figure 17. Figure 17 illustrates the typical vapour behaviour and surface temperature profile at quasi-steady state conditions. The surface temperature profiles in Figure 21 considered instability events in the single-phase region, around the nucleation site and in the two-phase region, which effected the surface temperature.

The nucleation site was 10 mm closer to the inlet for a heat flux of 13.3 kW/m^2 than for 8.2 kW/m^2. Increasing the effective heat flux increases the rate at which the bulk fluid temperature reaches saturation conditions. Once at saturation conditions, a nucleation site could be produced. The effect of rotation, mass flux and heat flux on the nucleation site are discussed in the next subsection.

6.4.2 Observed flow patterns

All channels had a single-phase region followed by a two-phase region, with the transition to two-phase indicated by a vapour slug or annular column with or without an identifiable nucleation site. Horizontal channels had a clear nucleation site, whereas rotated channels had a nucleation site that was hard to identify but displayed a clear bubble front. All channels experienced slug flow and annular flow, which consisted of a single large slug which grew larger towards the outlet of the channel during steady state behaviour.

The vapour location depended on the channel's orientation. Horizontal channels had an annular vapour column that had a bullet-shaped outline that spread the width of the channel. These channels also had a clear nucleation site where bubbles formed. The bubbles joined the main vapour column in one of two forms. The first was where the bubble detached from the nucleation site, forming a stand-alone bubble not attached to the heated surface or the vapour column. Figure 22 (a) depicts this pattern, with multiple bubbles having detached from the nucleation site, moving downstream to attach to the main annular vapour column. Bubbly flow is observed in this short region. The second case was where the vapour column was attached to the nucleation site with a bubbly flow region not observed, as shown in Figure 22 (b). Neither of the two cases presented were found in rotated channels.

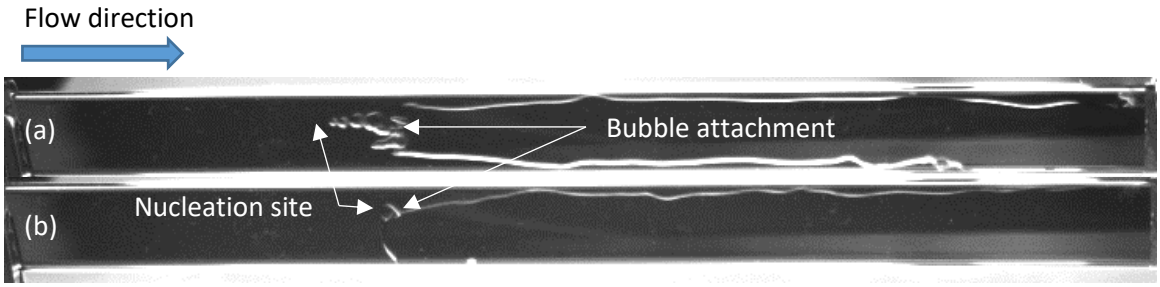

Figure 22: A vapour slug with (a) bubble detachment and growth upstream, and (b) direct contract with a nucleation site at a rotation of θ = 0° and mass flux (a) 40 kg/m²s and (b) 10 kg/m²s

Rotated channels had a nucleation site that was not always clearly visible as in the horizontal channels. The nucleation site was located at the liquid-vapour interface, with the main vapour column across the entire depth of the channel, enveloping the nucleation site. This meant that the liquid which evaporated at the nucleation site immediately coalesced with the vapour column making the nucleation site's location near impossible to determine using highspeed images. The vapour was pressed against the top of the channel (the portion furthest from the ground) with a curved vapour flow profile at the bottom. The vapour expanded across the depth of the channel at low vapour qualities and was forced to expand across the width of the channel as the vapour quality continued to grow. This geometry-enforced expansion is known as confinement and is shown in Figure 23.

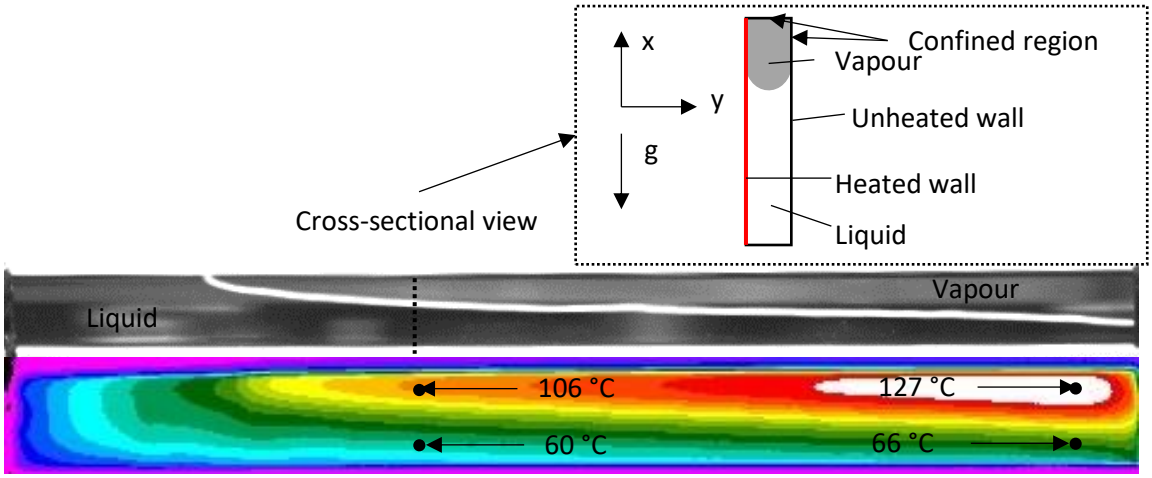

Figure 23: High-speed and infrared image of a channel at a rotation of θ = 90° with a cross-sectional representation of vapour bubble confinement

Figure 23 shows a high-speed and infrared image of a channel at a rotation of θ = 90°, with a cross-sectional view of the confined vapour slug. The cross-sectional view shows the vapour bubble confined between the heated and unheated walls, with vapour expansion in the negative x direction. This confinement produced premature dryout in the vapour region, resulting in high surface temperatures on the heated wall and significantly lower surface temperatures in the liquid region.

At the point where the cross-section view was drawn, a 46 K temperature difference was found between the vapour and liquid regions. Further downstream, at the point where the maximum surface temperature was recorded, a temperature difference of 61 K was found due to the larger local vapour quality. This discrepancy is of concern to heat transfer, because large thermal gradients can warp microelectronics or cause burnout. The large thermal gradient was due the vapour location in the channel and was not due to the channel's material. Vapour always produces a lower heat transfer coefficient and therefore higher surface temperature than liquid. This was due to the relatively low thermal conductivity of the vapour compared with the liquid-phase. This effect of vapour on the surface temperature was observed at all rotations, mass fluxes and heat fluxes.

Rotated channels experienced substantial confinement at low vapour qualities due to the depth being a tenth of the width of the channel. This resulted in confinement occurring at lower vapour qualities than was the case for horizontal channels – which had a width ten times greater for the bubble to expand across before confinement occurred.

Mass flux affected the shape of the flow around the nucleation site for horizontal channels. Figure 22 shows a horizontal channel at a mass flux of (b) 10 kg/m^{2}s and (a) 40 kg/m^{2}s. At the mass flux of 10 kg/m^{2}s, the bubble front covered more than 75% of the width of the channel within a few millimetres downstream of the nucleation site. At a mass flux of 40 kg/m^{2}s, the vapour slug's profile became strung-out, the vapour having moved more than 10% of the channel length downstream before 75% of the channel width was vapour. A mass flux of 10 kg/m^{2}s resulted in only slug flow during steady state behaviour, whereas a mass flux of 20 kg/m^{2}s and 40 kg/m^{2}s had both bubbly and slug flow. Rotated channels had an indistinguishable bubble front shape between different mass fluxes.

The nucleation site formed in the centre of the channel for horizontal orientations and at the top of the channel for rotated orientations. When a cold fluid was on the heated wall, a higher single-phase heat transfer coefficient was found than where hotter fluid was located. Horizontal channels exhibited nucleation sites at the centre of the channel due to the maximum fluid temperature being in the centre. Rotated channels had a nucleation site on the highest point of the channel, where the hottest – and therefore most buoyant – fluid was located, which reached saturation temperature first and resulted in a nucleation site. Nucleation sites are further discussed in 6.5.1.

6.5 Wall temperature profiles

Wall surface temperatures were measured using the infrared camera. The readings gave insight into the thermal stratification on the heated wall and by proxy the fluid. Bubble location effects on the heated surface were also observed. This subsection investigates the surface temperature profile along the length of the channel using the average surface temperature in each cross-sectional position. The cross-sectional profiles are investigated by considering the cross-sectional temperature at all axial positions. The effect of heat flux on the maximum cross-sectional temperature difference is presented for all rotations, mass fluxes and heat fluxes tested.

6.5.1 Nucleation site location (influence of rotation, mass flux and heat flux)

Nucleation site locations were affected by the inlet fluid temperature, the single-phase heat transfer coefficient and flow instability which sometimes resulted in the nucleation site's location moving. Flow instability resulted in increased heat transfer performance which meant that saturation conditions were reached closer to the inlet. This increased heat transfer performance in the single-phase region was due to increased fluid velocity resulting from reverse flow where the vapour would move up to

the length of the single-phase region to the inlet in 2 ms. This rapid motion resulted in the Reynolds number increasing producing turbulent flow and a resulting increased heat transfer performance. Thus, an orientation with higher flow instability would have a nucleation site that was closer to the inlet than the same test case without flow instability. Flow instability was heat flux, mass flux and rotation dependent.

Nucleation sites normally formed in approximately the centre of the channel, and the distance between the nucleation site and the inlet depended on the mass flux and heat flux combination. The nucleation site moved towards the inlet as the heat flux increased, for the same mass flux (see the discussion above regarding Figure 21). This was due to the local fluid's temperature increasing from a subcooled temperature to a saturated temperature more rapidly at higher heat flux conditions.

The distance between the inlet and the nucleation site can be used as an analogy for the heat transfer coefficient. A shorter distance between the inlet and the nucleation site, at the same flow conditions, is indicative of a higher heat transfer coefficient. Nucleation site position in the cross-section of the channel is of interest in tests where bubble detachment occurred. Bubble detachment from a position close to the top of a channel would not result in measurable secondary flow effects. Bubble detachment at the bottom of the channel had the possibility of producing measurable changes in the system's parameters, such as the heat transfer coefficient.

Nucleation site location is discussed first by considering the effect of rotation and heat flux jointly at each mass flux tested. A more complete picture emerges when considering the effect of both these parameters simultaneously. The mass flux effect is discussed later.

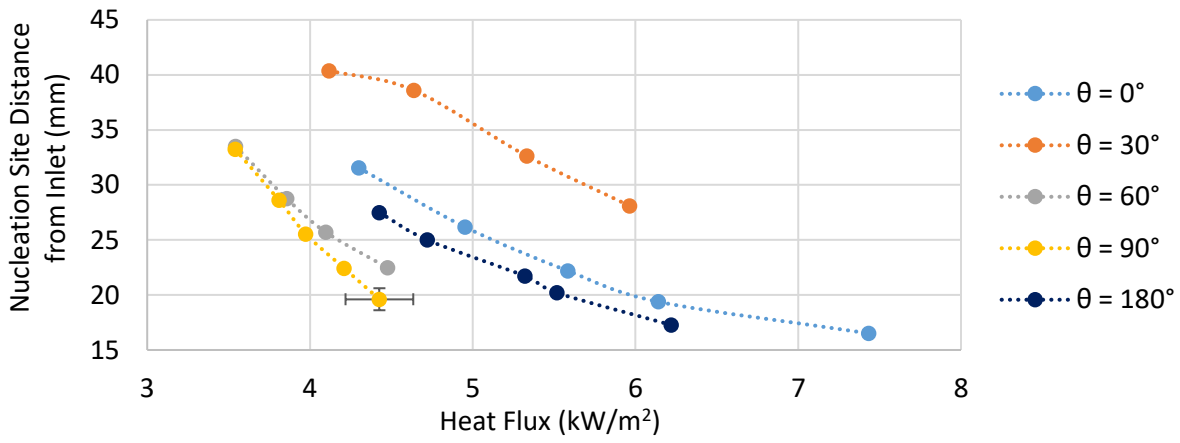

Figure 24: Nucleation site distance from inlet at rotations of θ = 0°, 30°, 60°, 90° and 180° and mass flux of 10 kg/m²s

From Figure 24, an increase in the heat flux, at a mass flux of 10 kg/m^{2}s, resulted in the distance between the nucleation site and the inlet decreasing, for all rotations. At all comparable heat fluxes (such as 4.5 kW/m^2), the nucleation sites of the horizontal channels were within 3 mm of each other, showing similar heat transfer behaviour. Channels at rotations of θ = 60° and 90° were closely grouped, with nucleation sites located within 3 mm of each other for all heat fluxes tested (such as 4.5 kW/m^2). These rotations had nucleation site closer to the inlet than the horizontal channels. The nucleation at a rotation of θ = 30° was at least 10 mm further from the inlet at all heat fluxes than the other rotations and up to 18 mm further away.

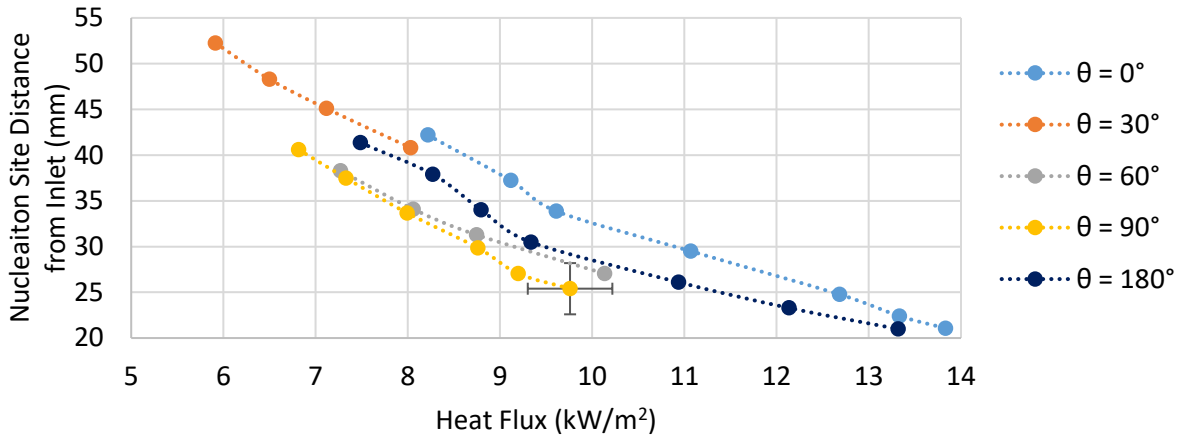

Figure 25: Nucleation site distance from inlet at rotations of θ = 0°, 30°, 60°, 90° and 180° and mass flux of 20 kg/m²s

The distance between the inlet and the nucleation site at all rotations was within 9 mm of each other at a heat flux of 8 kW/m^2 and a mass flux of 20 kg/m^{2}s, as is shown in Figure 25. This difference in nucleation site distance from the inlet for the various rotations was present at all heat fluxes tested. Channels at a rotation of θ = 60° and 90° had a near-identical distance between the inlet and nucleation site, with at most a 2 mm difference, at a heat flux of 9.7 kW/m^2. Horizontal channels, similarly, had less than a 4 mm difference in their distances between the nucleation site and the inlet.

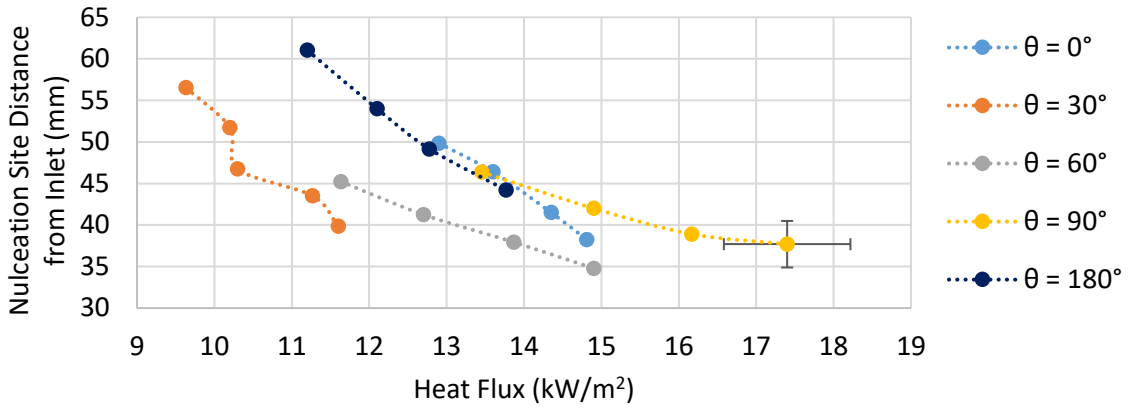

Figure 26: Nucleation site distance from inlet at rotations of θ = 0°, 30°, 60°, 90° and 180° and mass flux of 40 kg/m²s

From Figure 26, at rotations of θ = 0°, 90° and 180°, the distance between the inlet and the nucleation site was similar for each heat flux condition. The θ = 60° case had a shorter distance between the inlet and nucleation site than the other rotations, and θ = 30° had the shortest distance at the various heat flux conditions. The nucleation site in the θ = 30° case was closer to the inlet than in the θ = 0°, 90° and 180° cases, at each heat flux tested; this was because of the differences in inlet temperature to the system.

Two main factors affected the rate at which the bulk fluid's temperature increased to saturation conditions. The two factors were inlet fluid temperature and single-phase heat transfer coefficient. Higher inlet temperatures required less energy to be added to the system before saturation temperatures were reached, thus reducing the subcooled distance. A higher single-phase heat transfer coefficient resulted in a more effective transfer of energy from the heated wall to the fluid, which meant that a smaller heated area was required to reach saturation conditions.

The distance between the nucleation site and the inlet at the various rotations was expected to be nearly identical if the inlet fluid temperature was similar. At a mass flux of 10 kg/m^{2}s, the inlet temperature of the fluid at the various rotations differed by up to 4.9°C. At a mass flux of 20 kg/m^{2}s, the maximum inlet temperature difference was 3°C. A difference in the inlet temperature of 5.9°C was found between various rotations at a mass flux of 40 kg/m^{2}s.

These differences in inlet fluid temperature correlated with the distance between the inlet and the nucleation site. The maximum difference between the furthest and closest distance to the nucleation site was 18 mm, 10 mm, and 18 mm at a mass flux of 10 kg/m^{2}s, 20 kg/m^{2}s and 40 kg/m^{2}s, respectively at heat fluxes of 4.5 kW/m^2, 8 kW/m^2, and 11.2 kW/m^2. These findings suggest that to a large extent,

the variation in inlet fluid temperature was responsible for the differences in distance between the nucleation site and the inlet.

Single-phase heat transfer coefficients are discussed in section 6.6; these were found not to correlate with the distance to the nucleation site. Inlet fluid temperature has already been identified as a key contributor to differences between nucleation site locations. Another important factor to consider is the buoyancy of the single-phase liquid. The buoyancy of single-phase fluid at a rotation of θ = 60° and 90° could account for the shorter distance to the nucleation site. The buoyancy resulted in large thermal gradients in the transverse direction and the hottest liquid accumulating at the top of the channel. This would not occur in horizontal channels with buoyancy effects having a less substantial influence on the distance between the inlet and point at which the fluid reaches saturation conditions. As a result, θ = 60° and 90° had nucleation sites closer to the inlet at a mass flux of 10 and 20 kg/m^{2}s. At a mass flux of 40 kg/m^{2}s, θ = 60° was again closer to the inlet than the other rotations.

6.5.2 Wall temperature cross-sectional variation (influence of rotation, mass flux and heat flux)

Cross-sectional temperature variation were examined to assess the magnitude of the temperature gradient in a cross-section. This metric illustrated the effect of vapour location on the thermal gradient across a heated surface at different rotations. The cross-sectional variability was investigated first at all axial locations between the inlet and outlet, and at all time steps. The results illustrated the differences between the rotational orientations in the single-phase region, around the nucleation site and around the two-phase region. Second, the absolute maximum cross-sectional temperature variability was investigated. The maximum temperature variation demonstrated the importance of the vapour slug's settling location in the two-phase region.

A high surface temperature variation was indicative of poor heat transfer performance. High surface temperatures were a relative analytical tool, as 'high' or 'low' depended on the temperature that it was being compared to. Elevated surface temperatures meant that much of the available energy was absorbed by the microchannel (and then lost to the environment) rather than by the liquid.

Large cross-sectional temperature variations measured at specific rotations indicated a large variation in heat transfer performance in the cross-section. This scenario is dangerous in microelectronics as it can result in hotspots and warping. Varying the rotation of the channel allowed the buoyancy of the

heated fluid to be used to change the cross-sectional temperature profile. This was shown earlier, where horizontal channels had an even symmetrical thermal gradient in a cross-section, whereas rotated channels had an asymmetrical thermal gradient.

This section first compares the local cross-sectional temperature variation at mass fluxes of 10 kg/m^{2}s, 20 kg/m^{2}s and 40 kg/m^{2}s. The temperature variation was calculated locally at each control volume location shown in Figure 9, based on the maximum and minimum temperature in the cross-section. Rotations experiencing lower cross-sectional temperature variation at similar vapour qualities were deemed to be optimal. Vapour quality was used instead of distance from the inlet, as vapour quality was fundamental for understanding why large cross-sectional temperature variability occurred.

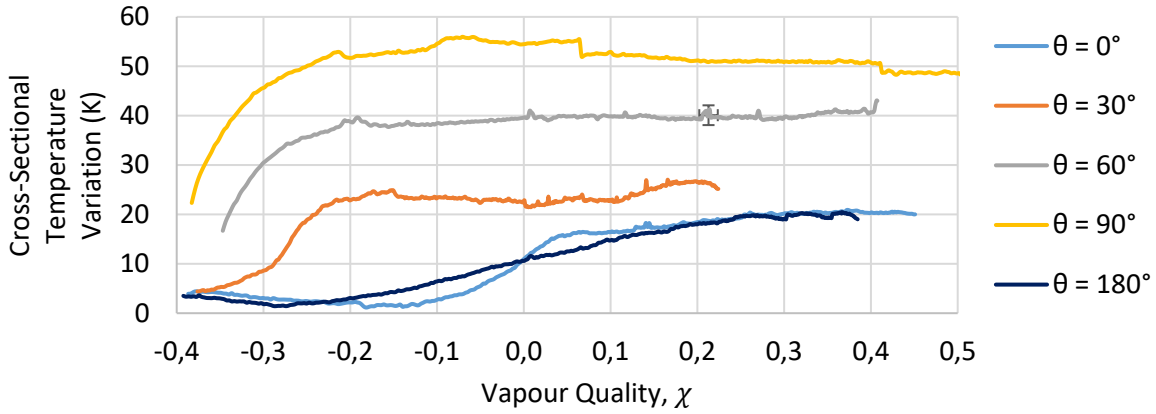

Figure 27: Cross-sectional temperature variation at a mass flux of 10 kg/m^{2}s and heat flux of 4.5 kW/m^2

Rotation is shown to affect the cross-sectional temperature variation, as is shown in Figure 27. Channels at a rotation of θ = 0°, 30° and 180° had temperature variations at the inlet that were nearly identical. The θ = 60° and 90° cases displayed temperature variations that were 13 K and 19 K higher at the inlet, respectively. Horizontal channels reached a maximum temperature variation of 20 K in the two-phase region. The temperature variation of channels at rotations of θ = 60° and 90° did not vary more than 7 K between a vapour quality of -0.2 and the outlet. The θ = 90° case produced a surface temperature variation at least 12 K higher than any other rotation and up to 44 K more than horizontal channels.

Thermal stratification of the rotated channels was far larger than that of the horizontal channels in the subcooled region ($\chi < 0$). This stratification was due to vapour being present in the subcooled region. The control volume in which saturation conditions were defined to have been met was based on the average cross-sectional fluid temperature having reached the saturation temperature. As a result of this model, vapour was present in the subcooled region. The vapour results in poor heat

transfer on the heated surface primarily due to the decreased thermal conductivity of the vapour when compared to the liquid. The asymmetric temperature profile is created by vapour at the top of the channel and liquid in the bottom of the channel.

The maximum cross-sectional temperature variation was found at a rotation of θ = 90° where the vapour slug became confined rapidly in the depth of the channel due to the large width-to-height ratio. The vapour slug in horizontal channels could expand 5 mm in the transverse direction before becoming completely confined, while θ = 90° only had the 0.5 mm depth before being confined. The θ = 30° and 60° cases had temperature variations between those experienced by horizontal channels and θ = 90° because the vapour slug requires a larger volume to become confined than θ = 90° but less than the horizontal channels.

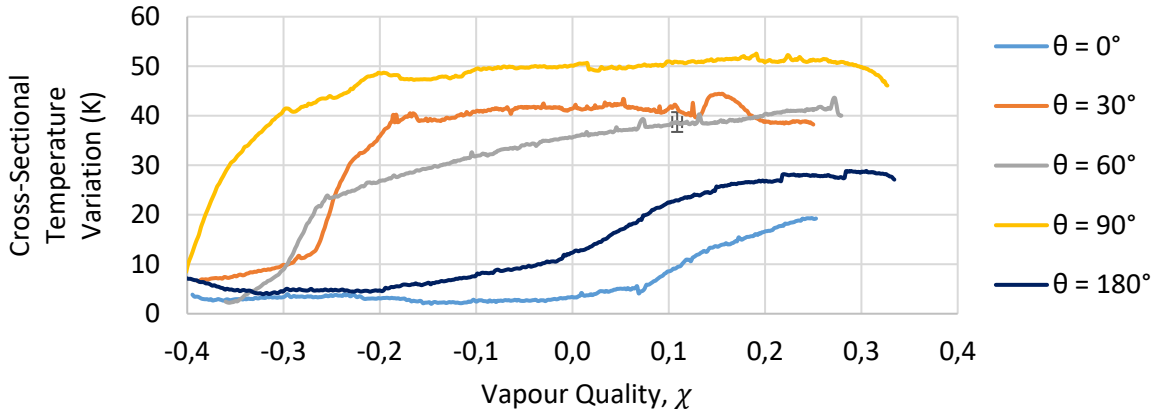

Figure 28: Cross-sectional temperature at a mass flux of 20 kg/m²s and heat flux of 8 kW/m²

At a mass flux of 20 kg/m²s, the cross-sectional temperature variations of the rotated channels was up to 48 K higher than those of horizontal channels, as is shown in Figure 28. The temperature variation at the inlet was similar at all rotations. Horizontal channels experienced little change in the temperature variation in the subcooled region while increasing steadily to a maximum near the outlet in the two-phase region. Rotated channels experienced an increase in the temperature variation in the subcooled region. The θ = 90° case experienced an increase in the temperature variation of 40 K between a vapour quality of -0.4 and -0.2. The θ = 90° case produced the highest surface temperature variability at all vapour qualities. θ = 30° and 90° showed no increase in their respective temperature variations between a vapour quality of -0.2 and the outlet.

The θ = 60° case displayed an unexpected temperature variation profile. The temperature variation increased rapidly between the inlet and a vapour quality of -0.25. A steady increase in temperature

variation was then observed between -0.25 and the outlet. The maximum temperature variation occurred at the outlet of the channel.

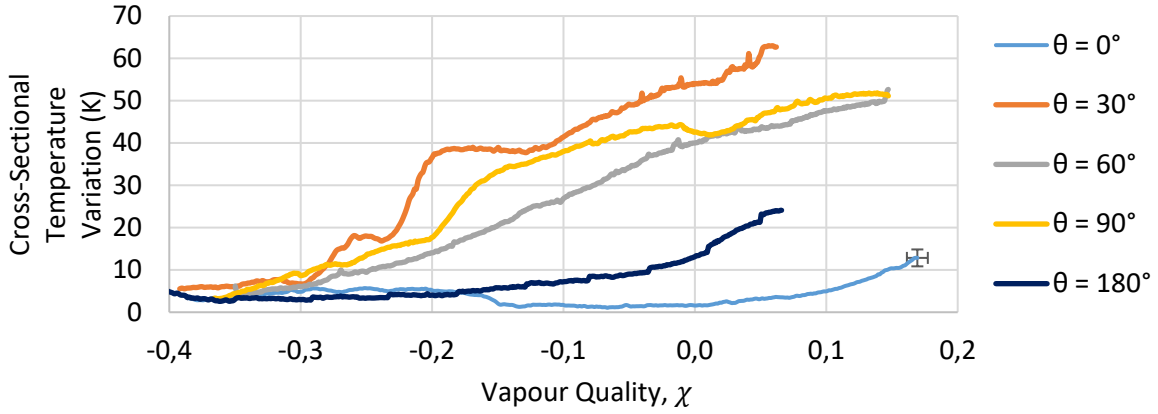

Figure 29: Cross-sectional temperature variation at a mass flux of 40 kg/m²s and heat flux of 12 kW/m²

From Figure 29, rotation is observed to affect the cross-sectional temperature variation. Rotated channels displayed increased temperature variations between the inlet and the outlet, starting in the subcooled region. The θ = 30° case produced the highest temperature variation at all vapour qualities, followed closely by θ = 60° and 90°. Horizontal channels produced the lowest temperature variations. Horizontal channels showed increased temperature variation at vapour qualities in the two-phase region. For all orientations, the absolute maximum temperature variation occurred at the exit vapour quality.

At mass flux of 10 kg/m²s, 20 kg/m²s and 40 kg/m²s, rotated channels had higher cross-sectional temperature variations than horizontal channels. This was primarily due to the volume of vapour required for confinement to occur being less as the rotational angle approached θ = 90°. The relatively low thermal conductivity of the vapour resulted in a decrease in the Nusselt number, leading to a decreased heat transfer coefficient and increased surface temperature locally. This two-phase distribution was enhanced as the rotational angle got closer to θ = 90°, resulting in the increased cross-sectional temperature variation.

Horizontal channels displayed relatively low cross-sectional temperature variations in both the subcooled and two-phase region. In the subcooled region, only liquid was found for horizontal channels which resulted in cross-sectional temperature variations remaining low and caused only by thermal satisfaction of the liquid. The increases in cross-sectional temperature variations evident in the two-phase region of horizontal channels were due to the level of confinement of the vapour

bubble and the extent to which dryout had occurred in the centre of the channel between the vapour and heated wall. When not fully confined, the liquid at the edges of the channel produced relatively lower surface temperatures and increased cross-sectional temperature variation. Once confined, liquid film thickness between the vapour slug and the heated wall at the centre of the channel is expected to be the driving factor in the continued increased cross-sectional temperature variation. From this analysis it can be concluded that for systems which are sensitive to cross-sectional temperature variations, horizontal channels should be used rather than rotated channels.

The effect of heat flux on the cross-sectional temperature variation was investigated at mass fluxes of 10 kg/m^{2}s, 20 kg/m^{2}s and 40 kg/m^{2}s. The absolute maximum cross-sectional temperature variation is presented. The maximum temperature variation was chosen from all the calculated temperature variation at any point on the heated wall and at any point in time. From the analysis presented in Figure 27, Figure 28 and Figure 29, this value can be expected in the two-phase region of horizontal channels. In rotated channels, it can occur in either the subcooled or two-phase region. These results are compared at the outlet vapour quality.

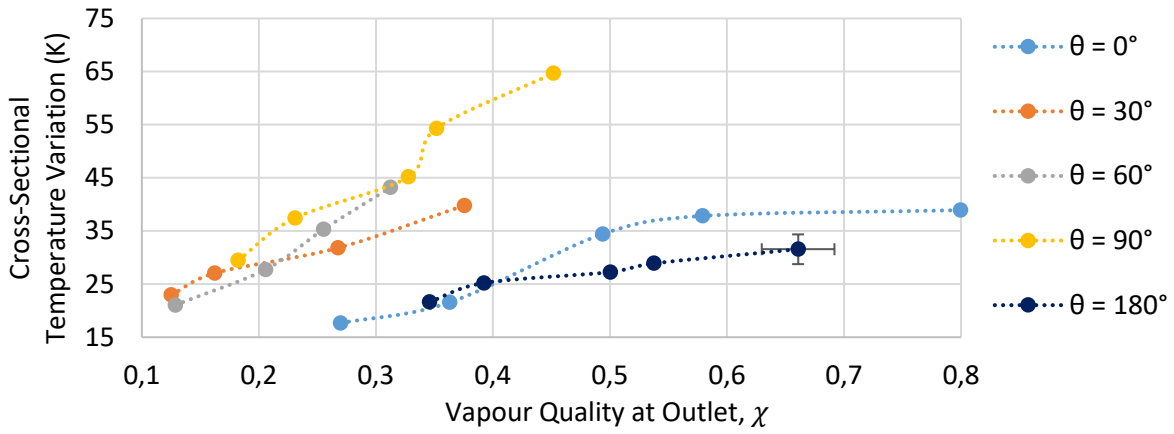

Figure 30: Temperature variability in a cross-section at a mass flux of 10 kg/m^{2}s

From Figure 30, an increase in the outlet vapour quality results in an increase in the cross-sectional surface temperature variation, at all rotations. Rotation affected the cross-sectional temperature variation with rotated channels producing higher temperature variations than horizontal channels at the same outlet vapour qualities. The rotated channels produced a cross-sectional temperature variation between 15 K and 33 K higher at an outlet vapour quality of between 0.3 and 0.35.

Horizontal channels seem to have a maximum cross-sectional temperature once the outlet vapour quality reaches 0.58 for θ = 0° and 0.54 for θ = 180°. The plateauing of the cross-sectional temperature

variation is expected to be due to the liquid film thickness decreasing at a similar rate across the cross-sectional width of the channel. The symmetric distribution of the vapour across the width of horizontal channels means that there is a proportional change in the local vapour quality at all cross-sectional locations.

Rotated channels have an asymmetrical vapour distribution across the width of the channel. Between the fully confined vapour slug and the heated wall a substantially smaller portion of the cross-section was high heat transfer liquid. This means that as the vapour quality increases the surface temperature in the vapour region continues to increase. In the liquid region the surface temperature increases slower with an increase in vapour quality as the high thermal conductivity of the liquid continues to effectively remove the heat from the heated surface.

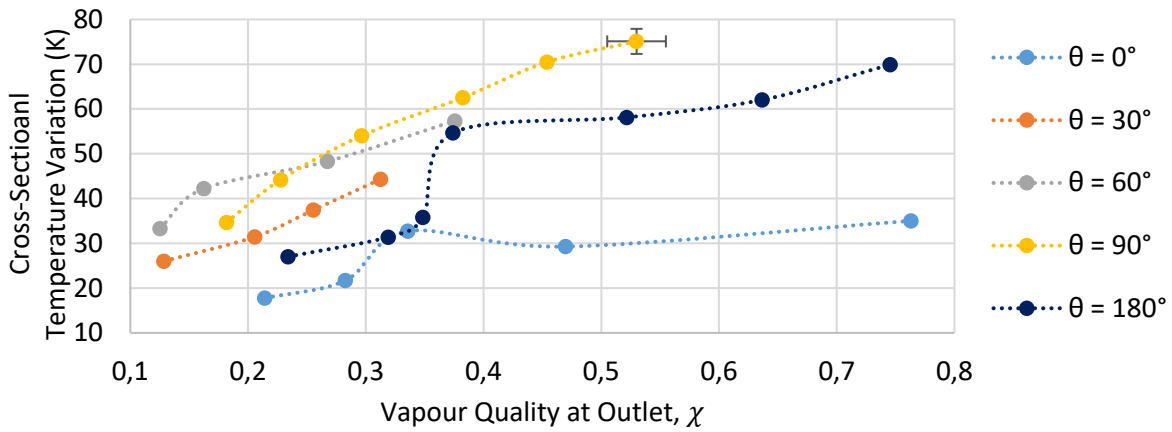

Figure 31: Temperature variability in a cross-section at a mass flux of 20 kg/m²s

From Figure 31, increases in outlet vapour quality are shown to result increases in the cross-sectional surface temperature variation. Rotation again affected the cross-sectional temperature variation. Horizontal channels, however, experienced two plateaus, with a sharp rise between the plateaus occurring at a vapour quality of 0.35. The θ = 0° case experienced an increase of 14 K with a change in vapour quality of 0.05. The θ = 180° case experienced a more substantial increase of 24 K in cross-sectional temperature variation with a change in vapour quality of 0.05. Rotated channels experienced a gradual increase in the cross-sectional temperature variation with an increase in vapour quality.

The θ = 0° case produced the lowest cross-sectional temperature variations at all outlet vapour qualities. The temperature variation of θ = 0° was at least 28°C lower than other rotations at vapour qualities above 0.35. By contrast, θ = 60° and 90° produced the highest cross-sectional temperature difference at all outlet vapour qualities. The θ = 90° case produced the maximum absolute

temperature variation, 75 K, at an outlet vapour quality of 0.53; this result was 17 K higher than that of θ = 180° and 45 K higher than θ = 0°.

The rapid increase in the cross-sectional temperature of horizontal channels was due to a change in confinement occurring at higher heat fluxes. At low heat fluxes, the vapour slug was almost completely confined in the two-phase region, whereas at higher vapour qualities the liquid below the vapour slug penetrated the sides of the slug, forcing it to the centre of the channel. This caused a portion of the heated surface's cross-section to be in contact with the vapour in the centre and the liquid on the sides.

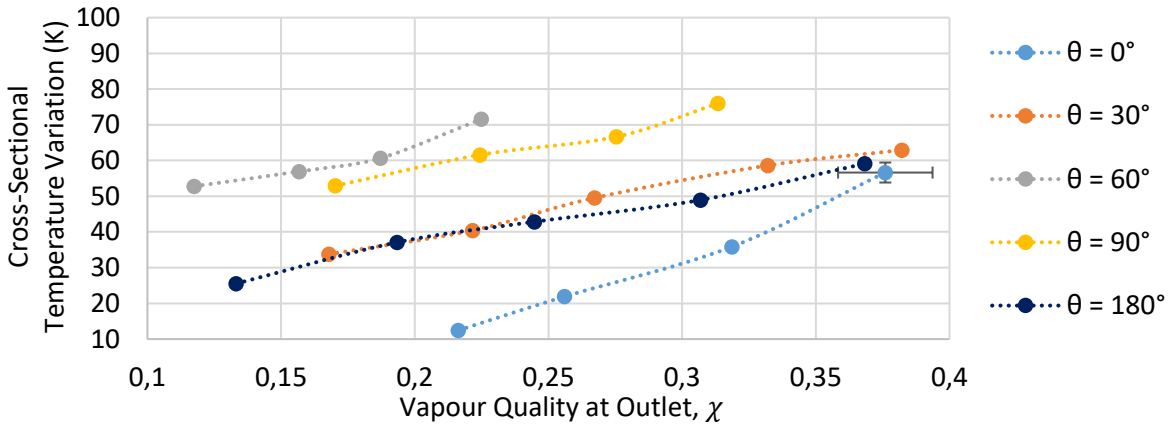

Figure 32: Temperature variability in a cross-section at rotations of θ = 0°, 30°, 60°, 90° and 180°; vapour qualities of χ = 0.12 to 0.38 and a mass flux of 40 kg/m²s

Figure 32 shows that increases in the outlet vapour quality resulted in an increase in the cross-sectional temperature variation, at all rotations. All rotations experienced an increase in the temperature variation of 6 K with an increase in outlet vapour quality of 0.1. The magnitude of the cross-sectional temperature variation depended on the rotation. The θ = 60° and 90° cases produced cross-sectional temperature variations of at least 15°C higher than the other rotations at all outlet vapour qualities.

The θ = 0° case produced the lowest cross-sectional temperature variations at all vapour qualities. The even distribution of vapour in the cross-section combined created an event spread of vapour above the heated surface. The thin layer of liquid between the vapour and the heated surface also assisted in keeping the cross-sectional temperature lower than at the other rotations.

For all rotations and mass fluxes tested, an increase in outlet vapour quality was associated with an increase in cross-sectional temperature variation. It was also found that rotated channels generally produced higher cross-sectional temperature variations than did horizontal channels. Horizontal channels experienced changes between complete and partial confinement of the vapour slug. This change in confinement resulted in both liquid and vapour encountering the heated wall, resulting in increases in the cross-sectional temperature variation.

From the analysis of cross-sectional temperature variations, it is concluded that rotated channels could pose a threat to microelectronics sensitive to such temperature variations. Horizontal channels were found to produce the lowest cross-sectional temperature variations in most cases. The θ = 0° case produced lower cross-sectional temperature variations than θ = 180° at some mass flux and heat-flux combinations, but the reverse was true at others. Thus, the optimal orientation regarding cross-sectional temperature variation depended on the mass flux and heat flux.

6.6 Heat transfer coefficients

This section discusses the time-averaged heat transfer coefficients calculated locally in each control volume. The local heat transfer coefficients are presented with the effect of rotation and heat flux discussed at three mass fluxes. The optimal channel orientation in each case was the one that produced the highest heat transfer coefficient. The rotations presented are θ = 0°, 30°, 60°, 90° and 180°.

6.6.1 Influence of rotation

The heat transfer coefficients are discussed with reference to the effect of rotation. The local heat transfer coefficients at the various rotations are directly compared at the same local vapour qualities. The vapour quality and heat transfer coefficients presented in this section were based on the time-averaged inputs: inlet temperature, outlet temperature, temperature inside the acrylic enclosure and infrared surface temperature.

An analytical model was used to calculate the time-averaged local vapour quality, local fluid temperature and local heat transfer coefficient. The vapour slug's size depended on the local vapour quality. Larger vapour qualities were indicative of a larger vapour slug, which has already been shown to impact the local heated wall temperature and the cross-sectional temperature variation.

Two-phase boiling was defined as the point at which the vapour quality reached χ = 0. As discussed, this point did not necessarily coincide with the nucleation site. At the nucleation site, a small portion of the fluid had reached saturation conditions. The analytical model was based on the average bulk fluid temperature in the entire cross-section. This could result in a small portion of the cross-section being vapour at a vapour quality less than 0.

A typical local heat transfer coefficient profile for each rotation at a mass flux of 10 kg/m^{2}s and heat flux of 4.5 kW/m^2 is shown in Figure 33. The physical interpretation of the vapour qualities are shown by indicating various regions of interest. The liquid-phase was the portion of the channel where no vapour was found. The nucleation region was the portion of the channel where a nucleation site was found, and vapour first formed. The vapour slug development region is where the vapour slug settled and started to grow but had not yet become confined. The developed vapour slug was the portion of the channel where the vapour slug's growth was impacted by both side walls of the channel with either partial or complete confinement.

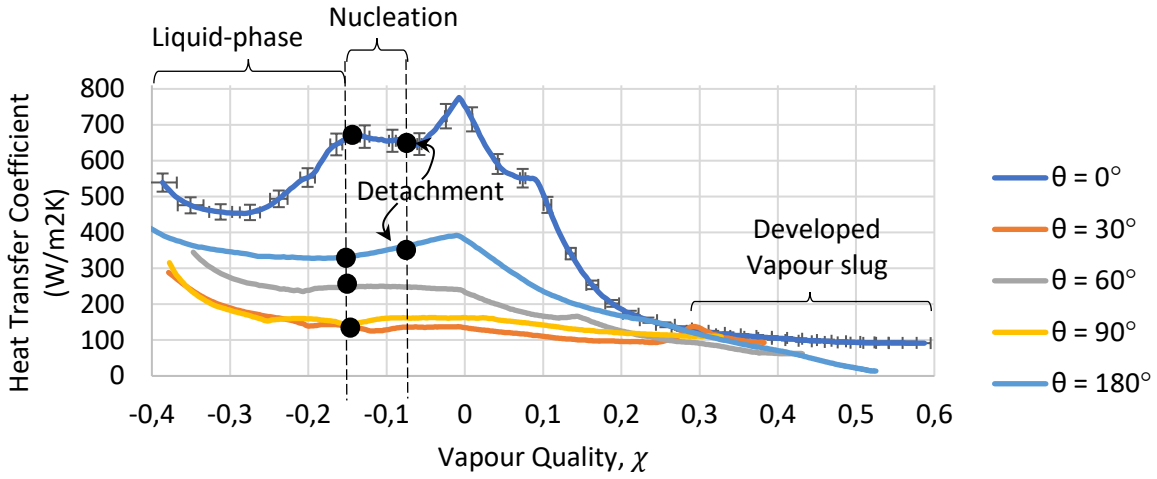

Figure 33: Local heat transfer coefficient at a mass flux of 10 kg/m^{2}s and a heat flux of 4.5 kW/m^2

The magnitude of the local heat transfer coefficients (see Figure 33) are directly influenced by the rotation of the channel and by the region investigated. In the liquid-phase region, a decrease in the local heat transfer coefficient was observed due to thermal flow development during sensible heating and a short portion of the inlet region (<5 mm) having some temperature distortion. The local heat transfer coefficients are not of the same magnitude at the inlet for two reasons. First, the inlet temperature was not precisely the same as discussed previously. Secondly, flow instability events influenced the time-averaged surface temperature in this portion of the channel, effecting the time averaged heat transfer coefficients. These instability events had large effects on the surface

temperature measured, the flow regime and the heat transfer coefficients. The analysis of flow instability fell outside the scope of this study.

The heat transfer coefficient of a channel at a rotation of θ = 0° increased between a vapour quality of -0.28 and -0.15. All other rotations either showed a subsequent decrease (θ = 30°, 90° and 180°) or a consistent heat transfer coefficient (θ = 60°). The improved heat transfer performance of θ = 0° was probably due to bubble detachment and growth around the nucleation site. Such bubble motion increases the local fluid velocity in this region by introducing a tangential velocity component.

Nucleation typically occurred at a single site at all rotations. Horizontal channels generally had nucleation sites in the centre of the channel, and rotated channels generally had nucleation sites towards the top of the channel. The θ = 0° case had a local maximum in the heat transfer coefficient at the nucleation site. All other rotations experienced no significant change in the heat transfer coefficient around the nucleation site.

Bubble detachment from the heated surface was observed at a rotation of θ = 0°. The detachment resulted in the heat transfer coefficient reaching its maximum value around a vapour quality of 0. Rotated channels experience no bubble detachment and thus no local peak in the heat transfer coefficient. The θ = 180° case experienced an increase in the local heat transfer coefficient. This increase was caused by bubble motion on the heated surface between the nucleation site and the vapour slug. An absolute maximum heat transfer coefficient was again found at a vapour quality of 0.

Vapour slug development resulted in a decrease in the local heat transfer coefficient at all rotations. Increase in the vapour slug's size resulted in partial or complete confinement of the vapour slug, which produced areas with dryout conditions. The dryout conditions resulted in high surface temperatures, which decreased the local heat transfer coefficients.

The rapid increase in the heat transfer coefficient at a rotation of θ = 0° was primarily due to bubble nucleation, growth and detachment which produced buoyancy assisted cooling where the motion of the vapour away from the surface increased the fluid's velocity vector in the transverse direction producing a localised increase in the liquid velocity. This was not observed at rotations of θ = 30°, 60°, 90° and 180° as these rotations have a vapour column directly in contact with the nucleation site. This meant there was no detached bubble motion resulting in buoyancy assisted cooling.

Developed vapour slugs became confined after sufficient heating was applied. Vapour slugs at horizontal rotations were confined in the width of the channel and had to expand into the depth. Vapour slugs of rotated channels were confined in the depth of the channel and were forced to expand in the width of the channel. In this region, the heat transfer coefficients appeared to converge to a similar value. The θ = 180° case was noted to experience a continual decline in the heat transfer coefficient, whereas other rotations remained approximately constant at vapour qualities greater than χ = 0.3. These findings were probably due to the vapour slug being directly on the heated surface, whereas other rotations had only partial coverage of the heated surface.

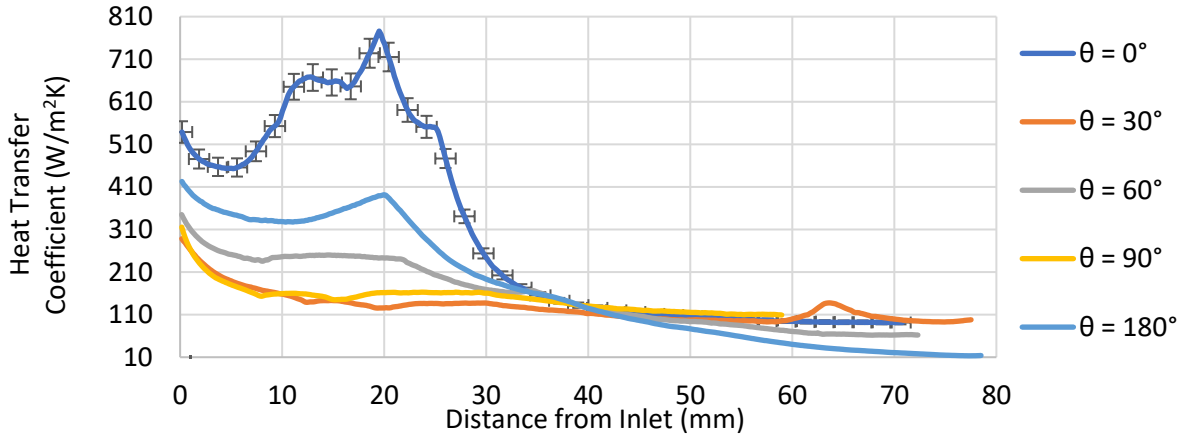

Figure 34: Local heat transfer coefficient at a mass flux of 10 kg/m²s and a heat flux of 4.5 kW/m² at various distance from the inlet

The local heat transfer coefficient at various axial distances from the inlet is shown in Figure 34. From this figure the bulk of the effective heat transfer occurs in the region between the inlet and 30 mm from the inlet. Past this point the heat transfer coefficient are nearly identical. θ = 60° and 90° have little change in the heat transfer coefficient between 10 mm form the inlet and the outlet, 20 mm closer than the other rotations.

Vapour quality and location were shown to significantly affect the surface temperature and therefore the heat transfer coefficient in sections 6.4 and 6.5. Figure 34 gives no information about vapour quality at axial locations thus subsequent heat transfer coefficient investigations will be presented while considering the local vapour quality rather than distance from the inlet.

This study focused on the flow boiling portion of the channel and thus only considered vapour qualities of $\chi \geq 0$. The maximum vapour quality worth comparing, from the observations in Figure 33, was determined to be around χ = 0.3. Above a vapour quality of 0.3, the difference between the heat

transfer coefficients at the various rotations was negligible. The effect of rotation on the heat transfer coefficients are compared at specific vapour qualities in the rest of this section.

The local heat transfer coefficients at all rotations tested are presented at mass fluxes of 10 kg/m^{2}s, 20 kg/m^{2}s and 40 kg/m^{2}s and corresponding heat fluxes of 4.5 kW/m^2, 8 kW/m^2 and 12 kW/m^2. Each figure compares the local heat transfer coefficient at specific local vapour qualities. The vapour qualities chosen were based on the observations in Figure 33. The optimal rotation was defined as the rotation resulting in the highest heat transfer coefficient at most vapour quality cases.

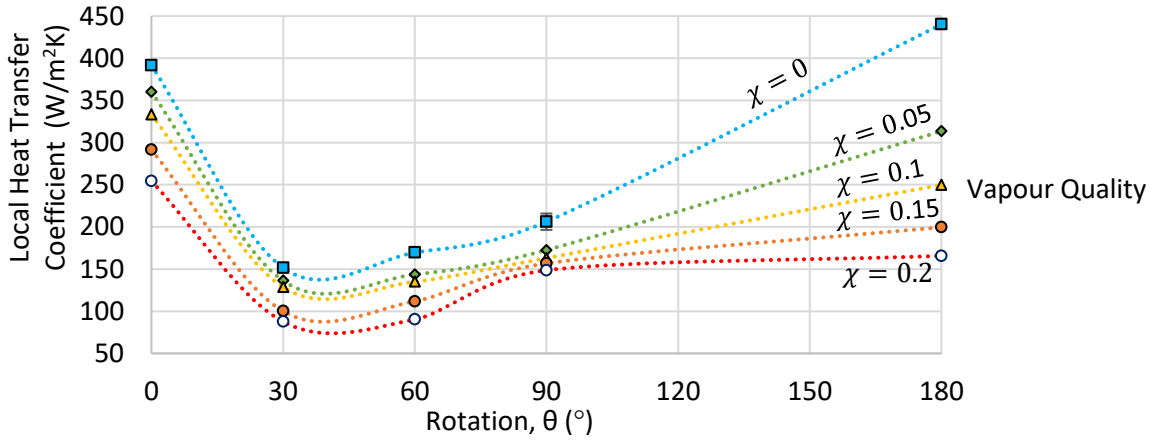

Figure 35: Local heat transfer coefficient at a mass flux of G = 10 kg/m^{2}s and heat flux of $\dot{q}$ = 4.5 kW/m^2

From Figure 35, rotation and vapour quality are shown to affect the heat transfer coefficient. The θ = 0° and 180° cases produced the highest heat transfer coefficients, at all vapour qualities. The θ = 30° and 60° cases yielded the lowest heat transfer coefficients at all rotations. The highest heat transfer coefficients, irrespective of the channel rotation, were achieved at a vapour quality of zero. All channels experienced a decrease in the heat transfer coefficient as the vapour quality increased.

The highest heat transfer coefficient, 440 W/m^{2}K, was recorded at a vapour quality of χ = 0 when the channel was rotated to θ = 180°. The θ = 0° case also experienced a maximum heat transfer coefficient at a vapour quality of χ = 0, at 390 W/m^{2}K (approximately 11% lower than for θ = 180°). The worst-performing case was θ = 30°, which had a maximum heat transfer coefficient 66% lower than that of θ = 180°.

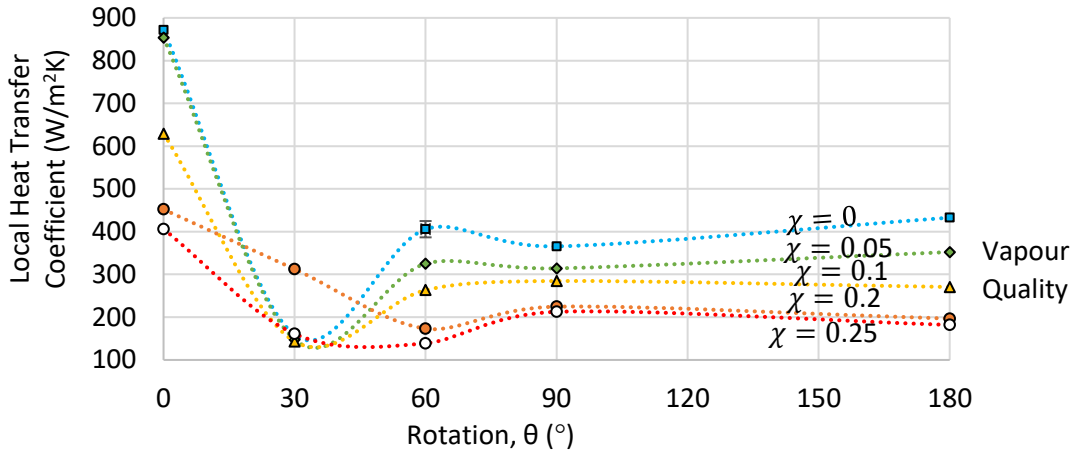

Figure 36: Local heat transfer coefficient at a mass flux of 20 kg/m²s and heat flux of 8 kW/m²

In Figure 36, the highest heat transfer coefficients were recorded at vapour quality of χ = 0. The heat transfer coefficient of θ = 0°, 60°, 90° and 180° decreased with an increase in vapour quality. The θ = 60°, 90° and 180° cases had local heat transfer coefficients that were within 70 W/m²K at the same vapour qualities. The θ = 30° case produced the lowest heat transfer coefficients at around 160 W/m²K at all vapour qualities except χ = 0.2. A second nucleation site caused by a surface imperfection unrelated to the channel rotation produced the increase.

The θ = 0° case consistently had a higher local heat transfer coefficient than the other rotational orientations. For instance, at vapour qualities of χ = 0, 0.1 and 0.2, θ = 0° had heat transfer coefficients that were respectively 100%, 132% and 134% greater than those of θ = 180°. As before, the lowest heat transfer coefficient at rotation of θ = 30°, which were between 60% and 81% lower than for θ = 0°.

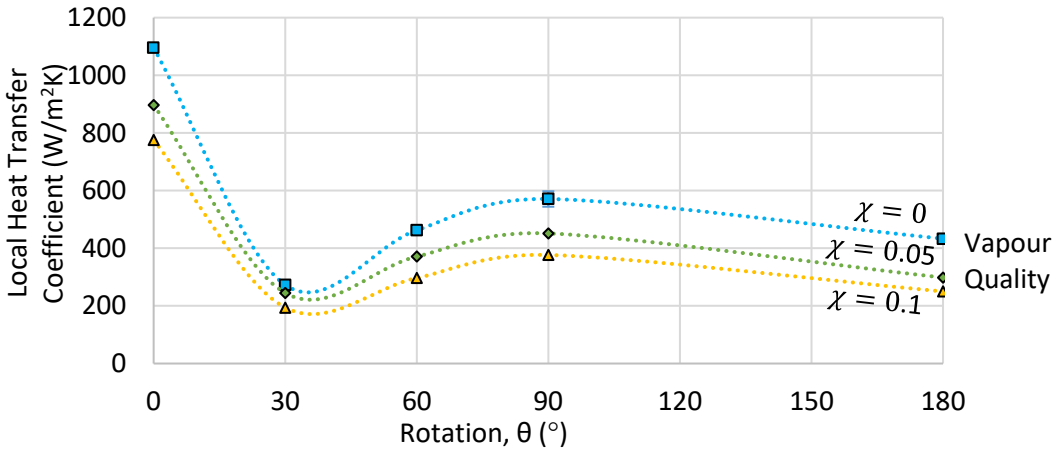

Figure 37: Local heat transfer coefficient at a mass flux of 40 kg/m²s and heat flux of 12 kW/m²

From Figure 37, rotation and vapour quality are observed to affect the local heat transfer coefficient. An increase in vapour quality produced a decrease in the local heat transfer coefficient, at all rotations. The θ = 0° case produced the highest heat transfer coefficient at all vapour qualities. At vapour qualities of χ = 0 and 0.1, bottom heating resulted in heat transfer coefficients that were 153% and 201% greater than those for top heating. The θ = 30° case produced heat transfer coefficients that were approximately 75% lower than for θ = 0°.

At mass fluxes of 10 kg/m^{2}s, 20 kg/m^{2}s and 40 kg/m^{2}s, the heat transfer coefficient decreased as the vapour quality increased. This vapour quality dependence is typical of nucleate boiling. Channels rotated at θ = 0°, 30°, 60° and 90° displayed increases in the local heat transfer as mass flux increased, typical of forced convection dominated boiling. The heat transfer coefficient for θ = 180° appeared to be independent of mass flux, typical of nucleate boiling dominated flows.

θ = 0° experienced the highest heat transfer coefficient of all the rotations due to a few factors. The first was bubble nucleation, growth and detachment enabling buoyancy assisted cooling to occur. This cooling was observed at some test cases at a rotation of θ = 180° but not for the rotated channels. The second was that as the vapour quality increased, a larger vapour quality was required for confinement to play a role in decreasing the heat transfer coefficient. θ = 180° had vapour nucleating on the heated surface resulting in the heat transfer coefficients that were less than θ = 0°. Rotated channels, as was previously discussed, experienced confinement at a substantially lower vapour quality. The regions of low heat transfer performance between the vapour slug and heated wall had a large effect on the average heat transfer coefficient in the cross-section.

The combination of nucleate boiling and forced convection dominated boiling requires further investigation to understand the dominant mechanism. Some flow-boiling cases do not have an inherently dominant mechanism and rely on both mechanisms. In this regard, θ = 0°, 30°, 60° and 90° presented as relying on a combination of both mechanisms. The θ = 180° case presented as being dominated by nucleate boiling. An increase in the heat transfer coefficient with an increase in heat flux would be typical of nucleate boiling. A decrease or no change in the heat transfer coefficient with an increase in the heat flux would be typical of forced convection dominant boiling. The effect of heat flux is investigated in the next subsection.

6.6.2 Influence of heat flux

In this subsection, the effect of heat flux on the heat transfer coefficient is discussed. This section presents each rotation separately at a mass flux of 10 kg/m^{2}s. This is the only mass flux presented because the heat flux affected each rotation the same way at all mass fluxes.

The rapid increase in the heat transfer coefficient at a rotation of θ = 0° was primarily due to bubble nucleation, growth and detachment which produced buoyancy assisted cooling where the motion of the vapour away from the surface increased the fluid's velocity vector in the transverse direction producing a localised increase in the liquid velocity. This was not observed at rotations of θ = 30°, 60°, 90° and 180° as these rotations have a vapour column directly in contact with the nucleation site. This meant there was no detached bubble motion resulting in buoyancy assisted cooling.

Nucleate-dominated boiling experiences an increase in the local heat transfer coefficient with an increase in the heat flux. This is because a stable nucleation site with bubble growth, detachment and motion are amplified at higher heat fluxes. Bubble departure size increases at higher heat fluxes, which produces relatively more intense secondary flow induced by bubble motion. This secondary motion increases the total fluid velocity, producing higher local heat transfer coefficients.

Figure 38 and Figure 39 represent the local heat transfer coefficients of the horizontal channels. Both the θ = 0° and 180° cases experienced an increase in the heat transfer coefficient with an increase in heat flux. Figure 40 and Figure 42 show the rotated flows of θ = 60° and 90°. The θ = 60° and 90° cases experienced a decrease in the heat transfer coefficient with an increase in heat flux. Figures 33 to 37 are presented from a subcooling of χ = -0.2 to the exit vapour quality.

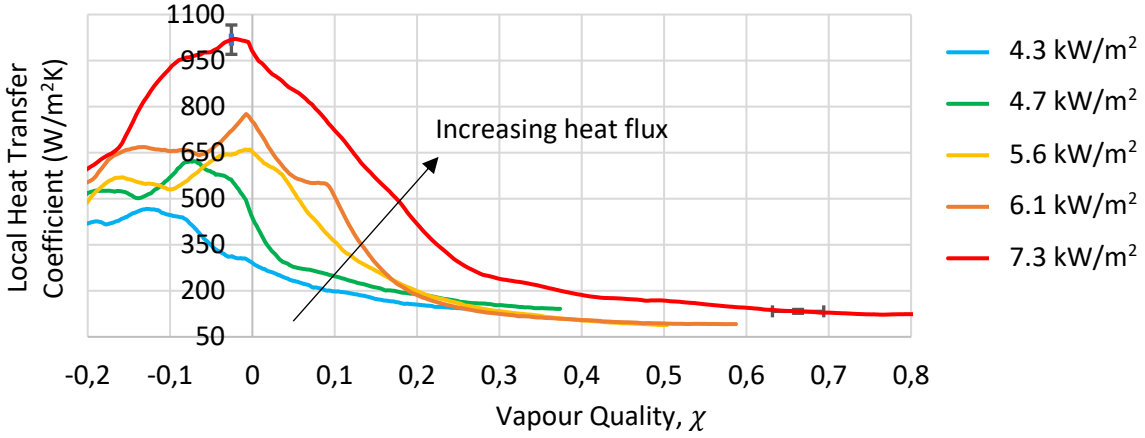

Figure 38: Local heat transfer coefficient vs vapour quality of a channel at a rotation of θ = 0° and mass flux of 10 kg/m²s

From Figure 38, it is evident that an increase heat flux was associated with increased heat transfer coefficient at most vapour qualities. The effect of heat flux on the heat transfer coefficient is amplified around a vapour quality of χ = 0. This was due to intensity of the bubble nucleation increasing as heat flux increased. The increased intensity was observed to be both rate and bubble size. It is expected that the increased intensity resulted in an increase in the transverse velocity of the liquid phase which assisted in increasing the heat transfer performance. The heat transfer coefficients reduced to approximately the same value at a vapour quality above χ = 0.2 at heat fluxes between 4.3 kW/m^2 and 6.1 kW/m^2. The heat transfer coefficient at a heat flux of 7.3 kW/m^2 remained higher than all other heat fluxes at all vapour qualities.

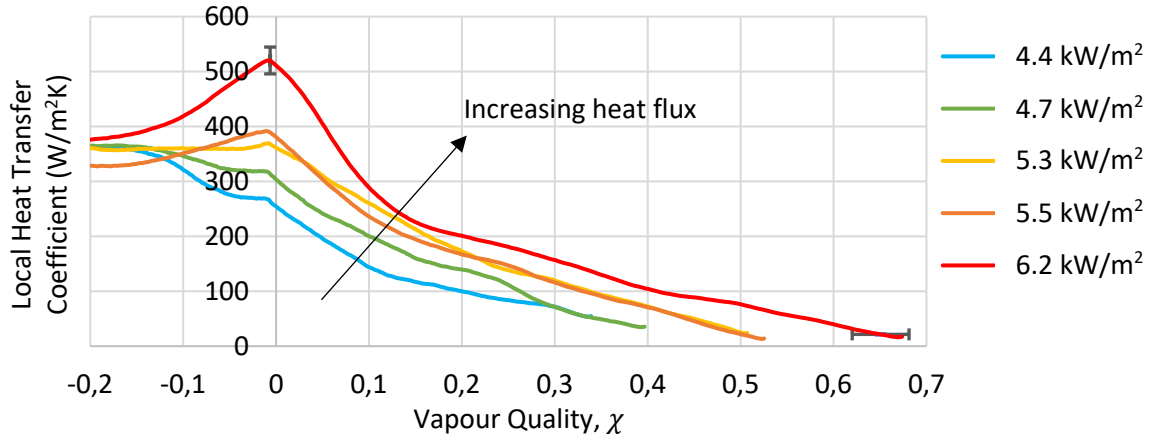

Figure 39: Local heat transfer coefficient vs vapour quality of a channel at a rotation of θ =180° and mass flux of 10 kg/m^{2}s

At a rotation of θ = 180°, an increase in heat flux resulted in an increase in the heat transfer coefficient, as is show in Figure 39. The initial heat transfer coefficients of the various heat fluxes at a vapour quality of χ = -0.2 were within a range of 48 W/m^{2}K of each other. Heat fluxes of 4.4 kW/m^2 and 4.7 kW/m^2 experienced a decrease in the heat transfer coefficient as vapour quality increased. At a heat flux of 5.3 kW/m^2, the heat transfer coefficient remained constant up to a vapour quality of 0, after which it gradually declined towards the exit. Heat fluxes of 5.5 kW/m^2 and 6.2 kW/m^2 showed an increase in the heat transfer coefficients between the inlet and a vapour quality of χ = 0, where a local maximum was found.

These trends can be explained by considering the effect of an increase in heat flux on the intensity of bubble nucleation. As heat flux increase, bubble nucleation, growth, and detachment occur more intensely resulting in an increase in the tangential velocity components. This enhances the buoyancy assisted cooling and allows for a higher heat transfer coefficient to be produced. At heat fluxes below

5.5 kW/m^2 the bubble nucleation was not intense enough to affect the local heat transfer coefficient as the vapour bubble almost immediately coalesced with the larger vapour slug.

The local heat transfer coefficients for tests at a heat flux of 4.4 kW/m^2 and 4.7 kW/m^2 merged to approximately the same value above a vapour quality of χ = 0.27. Similarly, tests at a heat flux of 5.3 kW/m^2 and 5.5 kW/m^2 merged to approximately the same value at all vapour qualities. The highest heat flux of 6.2 kW/m^2 yielded the highest heat transfer coefficient at all vapour qualities.

The maximum heat transfer coefficient was found at the highest heat flux tested, namely 6.2 kW/m^2. This maximum heat transfer coefficient value was 520 W/m^{2}K, which was 33% higher than that of the second highest heat flux (5.5 kW/m^2). The maximum heat transfer coefficient at a heat flux of 6.2 kW/m^2 was also 92% higher than at the lowest heat flux of 4.4 kW/m^2 at a vapour quality of χ = 0. All the observations discussed for θ = 180° are typical of nucleate-dominated flow boiling.

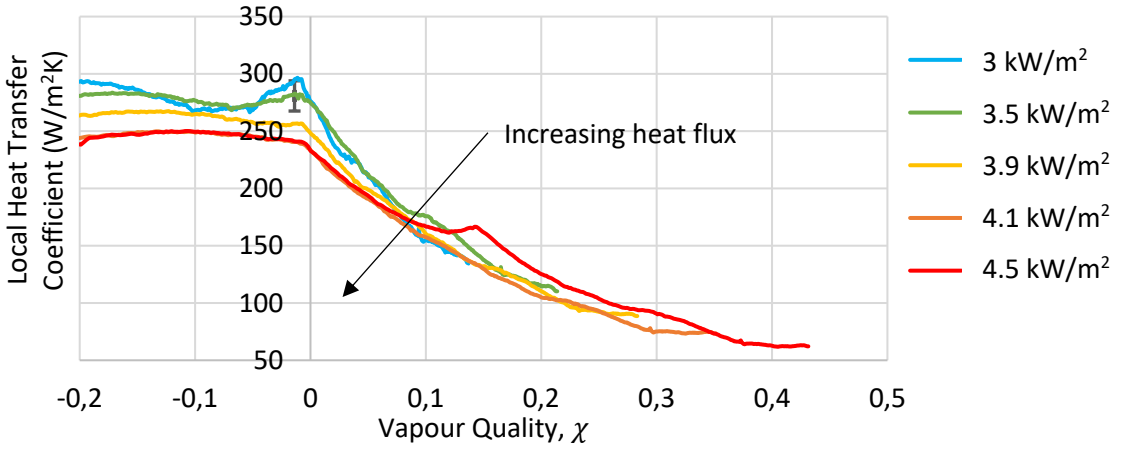

Figure 40: Local heat transfer coefficient vs vapour quality of a channel at a rotation of θ = 60° and mass flux of 10 kg/m²s

As shown in Figure 40, an increase in the heat flux produced a minor decrease in the heat transfer coefficient. Heat flux effects were relatively mild at this rotation with the heat transfer coefficients at all heat fluxes falling with in the error bars of the measurements. For χ = 0, the maximum heat transfer coefficient for a heat flux of 3 kW/m^2 was 295 W/m^{2}K, which was 25% higher than that of the highest heat flux (4.5 kW/m^2). The heat transfer coefficient of the various heat fluxes reached approximately the same value at vapour qualities above χ = 0.08. This suggests forced convection dominated boiling occurred without substantial bubble nucleation and detachment.

The only exception to the above findings was the highest heat flux of 4.5 kW/m^2, which showed an increase at a vapour quality of approximately χ = 0.15. For this flux, an increase in the heat transfer

coefficient resulted from a second nucleation site with bubble growth and detachment. The nucleation site was found at only this heat flux, suggesting some debris might have entered the microchannel during the test, resulting in the second peak. A high-speed image of the second nucleation site can be seen in Figure 41.

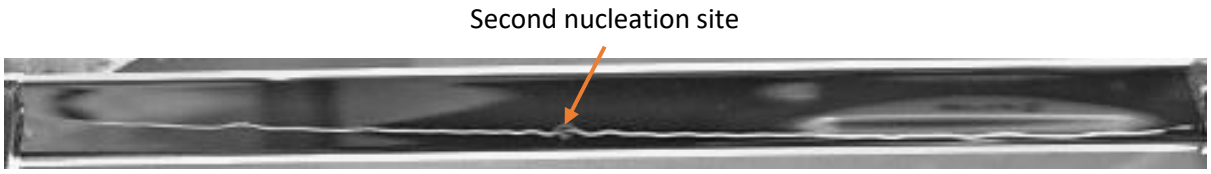

Figure 41: High-speed image of a channel at a rotation of θ = 60°, mass flux of 10kg/m²s and heat flux of 4.5 kW/m²

The secondary nucleation site resulted in a localised nucleate boiling mechanism increasing the heat transfer coefficient. In the small region around the nucleation site, nucleate-dominated boiling was the dominant mechanism. The θ = 60° case experienced forced convection dominated flow boiling due to the negligible effect of heat flux on the heat transfer coefficient, as is shown in Figure 40.

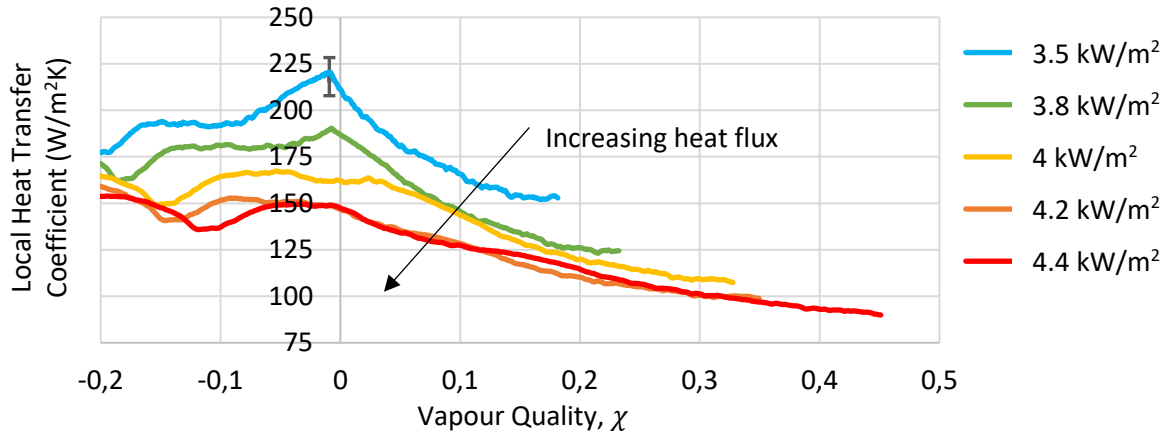

Figure 42: Local heat transfer coefficient vs vapour quality of a channel at a rotation of θ = 90° and mass flux of 10 kg/m²s

As shown in Figure 42, at a rotation of θ = 90°, the heat transfer coefficient decreased with an increase in heat flux. At a vapour quality of $\chi \geq 0.05$, the heat transfer coefficient at the two highest heat fluxes (4.2 kW/m² and 4.4 kW/m²) were approximately the same. Similarly, the heat transfer coefficients at heat fluxes of 4 kW/m² and 3.8 kW/m² converged to the same value.

The maximum heat transfer coefficient of 218 W/m²K was measured at a vapour quality of χ = 0, at the lowest heat flux (3.5 kW/m²). This maximum heat transfer coefficient was 15% higher than that of the second lowest heat flux (3.8 kW/m²) and was 48% higher than that of the highest heat flux

(4.4 kW/m^2). The difference between heat transfer coefficients of heat fluxes between 3.8 kW/m^2 and 4.4 kW/m^2 were negligible above a vapour quality of χ = 0.15. These observations suggest forced convection was the dominant flow boiling mechanism.

Heat flux affected the heat transfer coefficients at various rotations differently, depending on the main mechanism of boiling. As mentioned earlier, two flow mechanisms were observed: nucleate-dominated flow boiling and forced convection dominated flow boiling. The θ = 0° and 180° cases experienced increases in the local heat transfer coefficient as heat flux increased, indicative of nucleate-dominated boiling. The θ = 60° case had little change in the heat transfer coefficients as heat flux increased, indicating forced convection boiling. The θ = 90° case experienced decreases in the local heat transfer coefficient as the heat flux increased, indicative of forced convection boiling.

The θ = 0° case was influenced by a combination of forced convection and nucleation boiling. The influence of the nucleate boiling mechanism, however, was dominant when considering the heat flux and vapour quality effects. The θ = 180° case only experienced nucleate boiling as a mechanism.

The findings for θ = 60° and 90° were not as expected. Previously, the local heat transfer coefficient seemed to be nucleate boiling dominated, as a significant decrease in the heat transfer coefficient was observed with an increase in vapour quality. The θ = 60° and 90° cases have a combination of nucleate boiling and forced convection dominated mechanisms.

At a rotation of θ = 30°, the location of the most upstream nucleation site's location was affected by the combination of heat flux and mass flux, which is consistent with the observations from section 6.5.1. A second nucleation site was observed downstream the first nucleation site. While the experiments were conducted, it was not known if the presence of the second nucleation site was due to a containment, an imperfection on the microchannel's surface or bubble dynamic behaviour. An attempt was made to clear the channel in case it was a contaminant, after which, the nucleation site reformed at the same location. In the post-experiment analysis, it was found that the second nucleation site did not change location as heat flux changed, indicating that it was the result of a contaminant rather than flow behaviour. The attempt to clear the channel of debris must have been unsuccessful.

Identifying the nucleation site as being a contaminant could have been achieved by removing the channel, a swapping the inlet in the outlet location (reversing the flow direction through the channel).

This was not done because the channels used in this study had thin walls and were incredibly easy to break. Reorienting the entire setup was also not easy to do and the priority was put on keeping the orientation and inclination of the test section consistent for all single-phase and two-phase experiments at the rotation of θ = 30°.

From the analysis it was concluded that the second nucleation site was not a flow phenomenon but rather a contaminant in the flow passage. This observation does suggest that nucleation sites in this micro passage can be created by simply placing a surface structure or contaminant at various points along the heated length and have the heat transfer coefficient enhanced in this way.

As previously discussed, a nucleation site produces a significant increase in the local heat transfer coefficient as the bubble motion is expected to create secondary liquid motion towards the heated surface. Both nucleation sites would influence the heat transfer coefficient. At θ = 30°, heating occurred mainly from below, allowing any intense bubble growth with detached to move off the heated surface.

The effect of the second nucleation site was investigated at three mass fluxes (G = 10, 20 and 40 kg/m^{2}s) and various heat fluxes. Each test case is presented with a high-speed image and a plot of heat transfer coefficients at various heat fluxes. The high-speed image is a representation of the typical secondary nucleation site with bubble growth and detachment. The X-axis represents the distance from the inlet, in millimetres, rather than vapour quality. This is necessary to demonstrate the effect of the second nucleation site.

As shown in Figure 43, an increase in the heat flux resulted in a decrease in the heat transfer coefficient between the inlet and 20 mm from the inlet. The heat transfer coefficients were approximately the same at all heat fluxes between 20 mm from the inlet and the outlet. At the maximum heat flux of 6 kW/m^2, a localised increase in the heat transfer coefficient was found at the second nucleation site. This increase was attributed to the bubble detachment and growth from this second site. At the second nucleation site and a heat flux of 6 kW/m^2, a heat transfer coefficient of 137 W/m^{2}K was measured, which was 69% higher than the other heat fluxes. This increase suggests that when a significant nucleation site is present, nucleate boiling becomes the dominant heat transfer mechanism in this region. Forced convection dominated boiling was observed at all locations except the second nucleation site, for a heat flux of 6 kW/m^2.

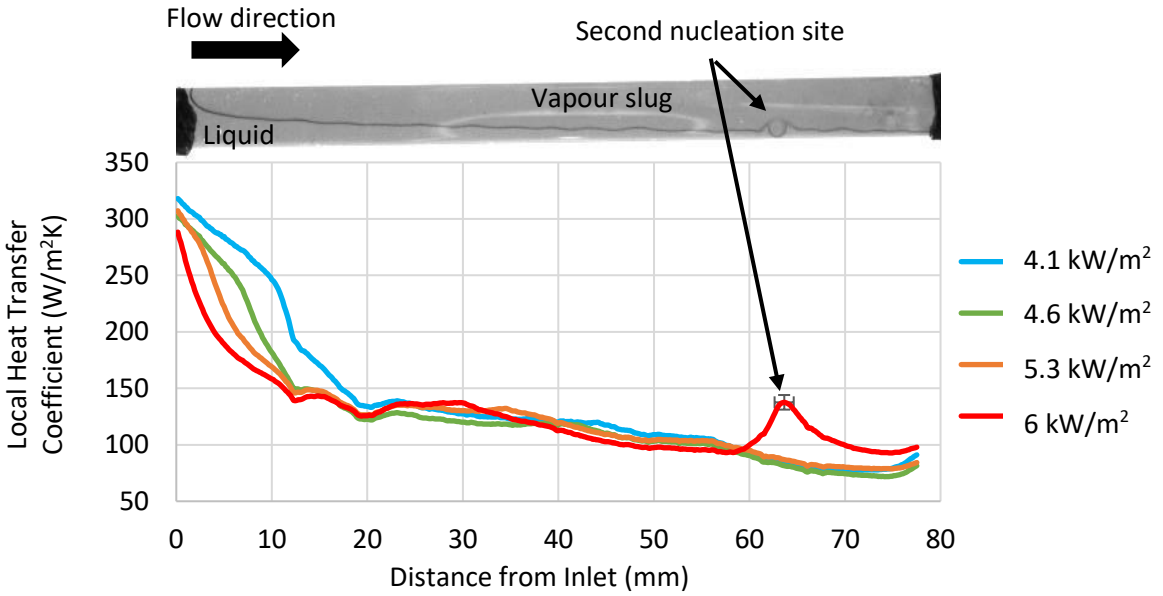

Figure 43: Local heat transfer coefficients at a rotation of θ = 30° with two nucleation sites at a mass flux of 10 kg/m²s

From Figure 44, the heat transfer coefficient at the second nucleation site decreased with an increase in the heat flux. The heat transfer coefficients were not impacted by changes in the heat flux in the single-phase region up to 10 mm from the inlet. A drop of up to 30% in the heat transfer coefficient was found beyond the first nucleation site. Bubble confinement resulted in the heat transfer coefficient produced by the lowest heat flux (5 kW/m²) being 44% higher than that of the highest heat flux (8 kW/m²) at the first nucleation site.

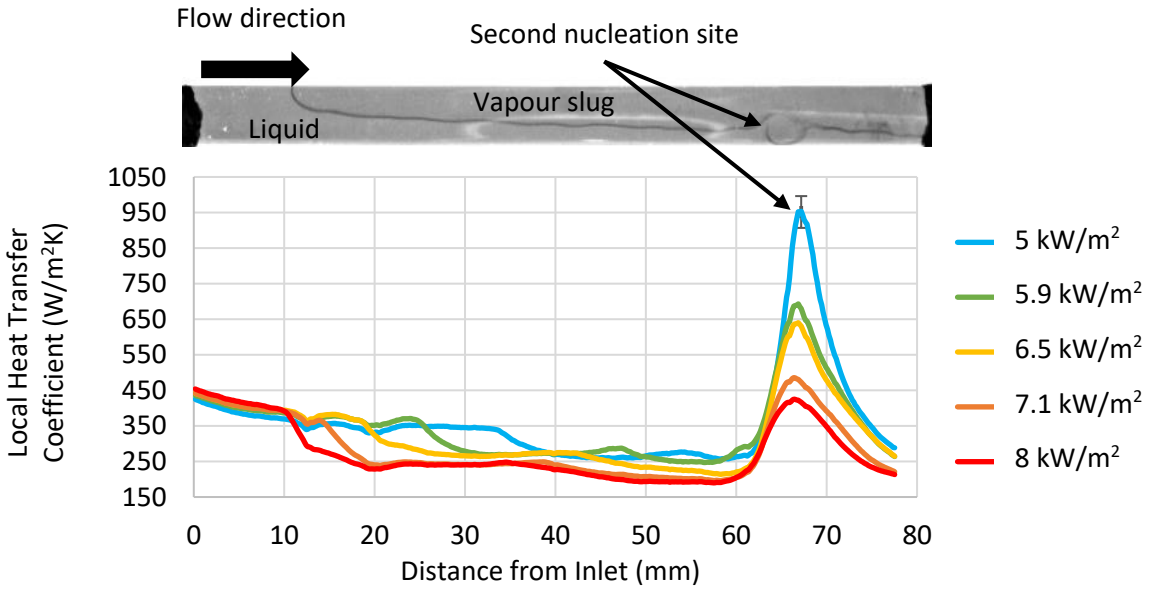

Figure 44: Local heat transfer coefficient at a rotation of θ = 30° with two nucleation sites at a mass flux of 20 kg/m²s

At the second nucleation site, an increase in the heat flux from 5 kW/m^2 to 8 kW/m^2 decreased the local maximum heat transfer coefficient produced from 942 W/m^{2}K to 410 W/m^{2}K. The lowest heat flux produced a heat transfer coefficient 130% higher than the highest heat flux, indicating forced convection dominated boiling. The forced convection behaviour was attributed to the large vapour quality resulting in a relatively shorter distance for the bubble to move before reaching the vapour slug. The shorter distance resulted in relatively minor secondary liquid motion from the surface. Forced convection dominated boiling was observed at all axial locations.

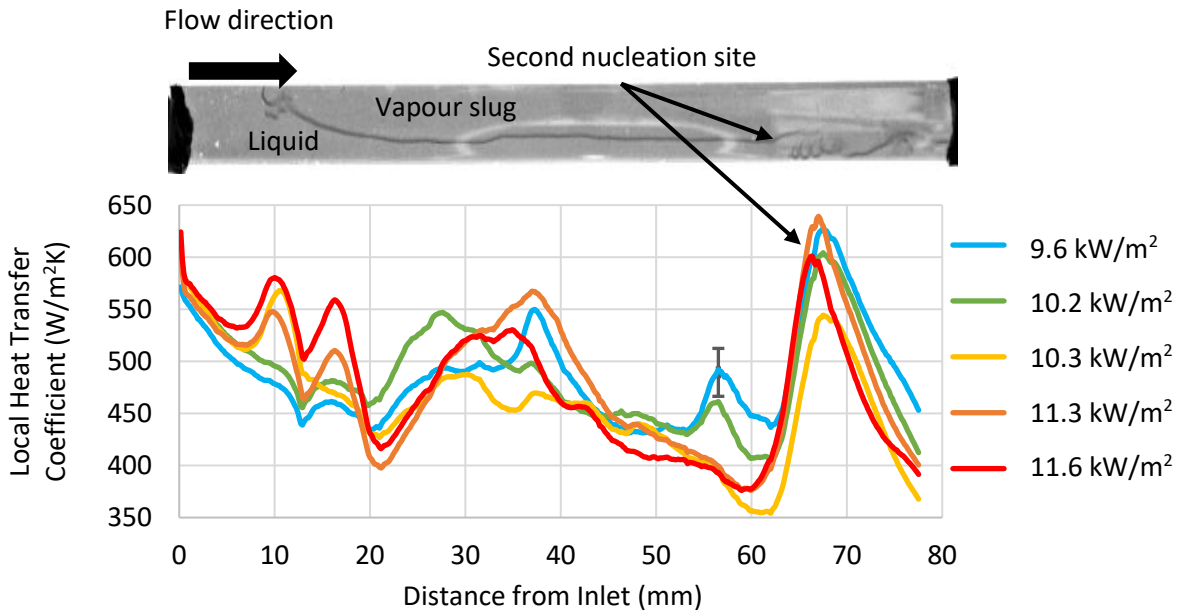

Figure 45: Local heat transfer coefficient at a rotation of θ = 30° with two nucleation sites at a mass flux of 40 kg/m^{2}s

The effect of heat flux was more challenging to identify at a mass flux of 40 kg/m^{2}s, with four regions producing different heat flux dependencies, as is shown in Figure 45. The first region was less than 20 mm from the inlet; here, a nucleation site was found with bubble growth and detachment. In this first region, nucleate boiling dominated, with an increase the heat transfer coefficient as heat flux increased. The second region was between 20 mm and 50 mm from inlet. No clear relationship was observed here between the heat transfer coefficient and heat flux. The lack of a relationship indicates that forced convection dominated the boiling.

The third region, between 50 mm and 63 mm from the inlet (before the second nucleation site), had the lowest heat flux (9.6 kW/m^2) produce the highest heat transfer coefficient. 9.6 kW/m^2 produced a heat transfer coefficient that was 28% higher than those of the heat fluxes 10.3 kW/m^2, 11.3 kW/m^2 and 11.6 kW/m^2. A heat flux dependence indicated forced convection as the dominant mechanism. In the final region, between 63 mm from the inlet and the outlet, the second nucleation site was found.

The heat transfer coefficients here were approximately the same at all heat fluxes, indicating forced convection dominated boiling.

The effect of a second nucleation on the heat transfer coefficient in this section has shown that ensuring unintentionally placed microstructures, such as contaminants, are removed from the channel is paramount. The heat transfer coefficient at a rotation of θ = 30°, and with a second nucleation site, was affected by an increase in heat flux. Forced convection was the dominant heat transfer mechanism at a mass flux of 10 kg/m^{2}s; the second nucleation only produced an increase in the heat transfer coefficient at the highest heat flux. Forced convection was the dominant boiling mechanism. This was evident in a decrease in the heat transfer coefficient both before the second nucleation site and at the second nucleation site, with an increase in heat flux at a mass flux of 20 kg/m^{2}s. A complicated relationship with both boiling mechanisms dominant in certain regions of the channel was found at a mass flux of 40 kg/m^{2}s. The θ = 30° case was generally dominated by forced convection boiling.

6.7 Pressure drop

Pressure drop was not the primary focus of this study. This study specifically investigated the effect of rotation, mass flux and heat flux on the heat transfer coefficient. A brief discussion on the total pressure drop is presented in this section.

The total pressure drop was a summation of many components, including frictional pressure drop, momentum pressure drop and hydrostatic head. In this experimental study, the system was horizontal for all tests. The pressure drop due to hydrostatic head was assumed to be negligible. The pressure drop reported, comprised mainly of frictional and momentum pressure drops.

The total pressure drop reported used the outlet as the reference. A positive total pressure drop indicated that the pressure at the outlet was higher than the pressure at the inlet. A negative pressure drop indicated that the pressure at the inlet was higher than the pressure at the outlet. The pressure measurements used were time averaged at the inlet and outlet and across experimental repetitions.

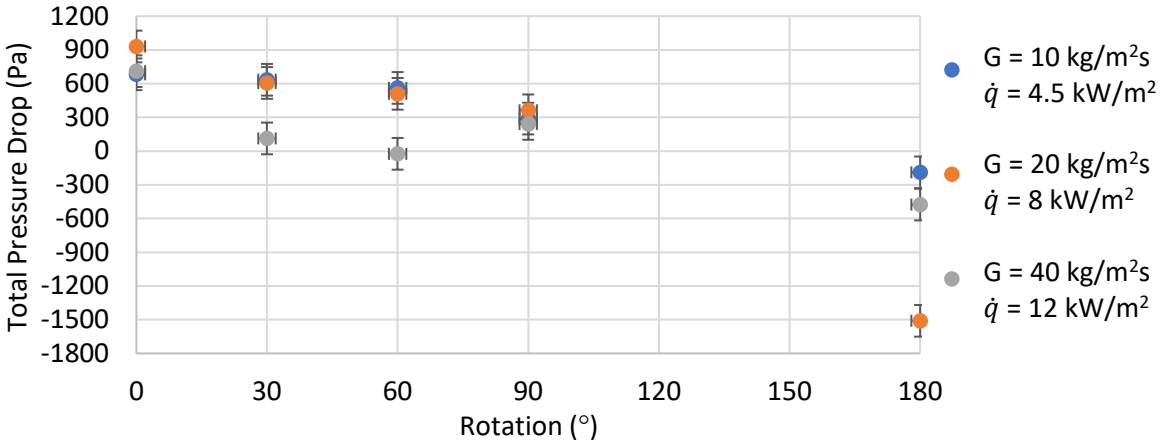

Figure 46: Total pressure drop at rotations of θ = 0°, 30°, 60°, 90° and 180°

From Figure 46, the total pressure drop is shown to be affected by rotation at the heat flux and mass flux combinations presented. Total pressure drop was found to decrease from a rotation of θ = 0° to 180° at mass fluxes of 10 kg/m^{2}s and 20 kg/m^{2}s. At a mass flux of 40 kg/m^{2}s, no clear effect of rotation was observed. The highest total pressure drop at most rotations – positive for 0°, 30°, 60°, 90° and negative for 180° – occurred at a mass flux of 20 kg/m^{2}s. These results indicated that a large positive total pressure drop was dominated by the momentum pressure drop, whereas a large negative total pressure drop was dominated by the frictional pressure drop.

The negative total pressure drops experienced in the θ = 180° case indicate that the frictional pressure drop was much larger at this rotation than at the other rotations. It is posited that in the other rotations, vapour was generally located far from the heated surface, producing larger vapour velocities, and increasing the momentum pressure drop. The vapour moved faster when it was farther from the heated surface, yielding a smaller drop in frictional pressure. By contrast, in the θ = 180° case the heated vapour was on the top surface, causing constant friction between the fast-moving vapour and the heated surface. It seems likely that flow instability might also play a role in this finding, with reverse flow and vapour motion towards the outlet. This would result in increased pressure at the inlet and decreased pressure at the outlet, producing large negative pressure drop readings. Pressure instability fell outside the scope of this study.

6.8 Chapter summary

In this chapter, validation of the experimental setup and data reduction method was shown to produce accurate results, which were congruent with literature. Heat transfer coefficients were calculated locally. The effect of rotation and heat flux were found to be significant due to their effects

on the location of bubble nucleation and growth and the presence of bubble detachment. The θ = 0° case produced the highest heat transfer coefficients at most combinations of mass flux and heat flux. The θ = 180° case was nucleate boiling dominated. The θ = 0°, 60° and 90° cases were dominated by both nucleate boiling and forced convection. The θ = 30° case was dominated by forced convection.

7. Conclusion

Experimental studies on the effect of gravitational orientation on flow-boiling in microchannels have shown that the largest difference in local heat transfer coefficient between top- and bottom-heated channel occurs on the section of the heated surface that experiences bubble nucleation and departure [44, 213].

Few studies have investigated rotational effects experimentally and none has been conducted in microchannels with one-sided heating with a high aspect ratio at intermediary rotations, which is relevant to non-stationary electronic components and equipment that do not have a fixed gravitational orientation. These influences have not yet been investigated specifically for FC-72, which is a suitable fluid for electronic cooling.

The purpose of this study was to increase this breadth of knowledge in the literature by producing heat transfer coefficient data for FC-72 in a single horizontal microchannel with a high aspect ratio, heated on one side at rotations between bottom and top heated. This data is necessary in electronic cooling applications where the orientation can be chosen e.g., server rooms or is not fixed, e.g., laptop computers as well as manned and unmanned aircraft.

The experimental facility used in this study was a modified version of the decommissioned experimental setup from the University of Edinburgh, allowing for rotational and inclination orientations to be altered. The once through system used flow boiling of FC-72 in a microchannel which had a visually transparent layer of Tantalum applied, facilitating single-sided heating to occur. Infrared thermography was used to measure temporal variations of the heated surface temperatures in the axial and transverse direction to be captured.

Heat transfer analysis of the rotational experiments is discussed in chapter 6. In this chapter the validation of the experiment setups and data reduction process is shown to produce accurate results with good agreement with literature. θ = 30°, 60° and 90° were found to have significant asymmetric surface temperature gradients which could result in warping of electronic components. θ = 0° and 180° had symmetric thermal gradients with a lower risk of electronic component warping due to thermal gradients than θ = 30°, 60° and 90°.The heat transfer coefficients were calculated locally with the effect of rotation and heat flux found to be significant due to their effects on the location of bubble nucleation, growth and presence of bubble detachment. θ = 0° was found to produce the highest heat

transfer coefficients at most mass flux and heat flux combinations. θ = 0° and 180° were nucleate boiling dominated with increases in heat flux producing increases in the heat transfer coefficient; also, an increase in the local vapour quality resulted in a decrease in the heat transfer coefficient. θ = 30°, 60° and 90° are forced convection dominated with a decrease in the heat transfer coefficient as heat flux increase and no clear nucleation site; also, it is observed that an increase in local vapour quality produces a decrease in the heat transfer coefficient. The optimal channel was found to be θ = 0° with the lowest cross-sectional temperature gradients and the highest heat transfer coefficient in all cases.

Bibliography

[1] S. Lee, V.S. Devahdhanush, I. Mudawar, Investigation of subcooled and saturated boiling heat transfer mechanisms, instabilities, and transient flow regime maps for large length-to-diameter ratio micro-channel heat sinks, International Journal of Heat and Mass Transfer, 123 (2018) 172-191.
[2] Y. Pi, J. Chen, M. Miao, Y. Jin, W. Wang, A fast and accurate temperature prediction method for microfluidic cooling with multiple distributed hotspots, International Journal of Heat and Mass Transfer, 127 (2018) 1223-1232.
[3] S. Sandler, B. Zajaczkowski, Z. Krolicki, Review on flow boiling of refrigerants R236fa and R245fa in mini and micro channels, International Journal of Heat and Mass Transfer, 126 (2018) 591-617.
[4] T. Van Oevelen, J.A. Weibel, S.V. Garimella, The effect of lateral thermal coupling between parallel microchannels on two-phase flow distribution, International Journal of Heat and Mass Transfer, 124 (2018) 769-781.
[5] K.P. Drummond, D. Back, M.D. Sinanis, D.B. Janes, D. Peroulis, J.A. Weibel, S.V. Garimella, A hierarchical manifold microchannel heat sink array for high-heat-flux two-phase cooling of electronics, International Journal of Heat and Mass Transfer, 117 (2018) 319-330.
[6] W. Li, K. Zhou, J. Li, Z. Feng, H. Zhu, Effects of heat flux, mass flux and two-phase inlet quality on flow boiling in a vertical superhydrophilic microchannel, International Journal of Heat and Mass Transfer, 119 (2018) 601-613.
[7] J. Lee, Y. Joo, S.J. Kim, Effects of the number of turns and the inclination angle on the operating limit of micro pulsating heat pipes, International Journal of Heat and Mass Transfer, 124 (2018) 1172-1180.
[8] D. Ansari, K.-Y. Kim, Hotspot thermal management using a microchannel-pinfin hybrid heat sink, International Journal of Thermal Sciences, 134 (2018) 27-39.
[9] D.B. Tuckerman, R.F.W. Pease, High-performance heat sinking for VLSI, IEEE Electron Device Letters, 2(5) (1981) 126-129.
[10] S.T. Kadam, R. Kumar, Twenty first century cooling solution: Microchannel heat sinks, International Journal of Thermal Sciences, 85 (2014) 73-92.
[11] A. Mohammed Adham, N. Mohd-Ghazali, R. Ahmad, Thermal and hydrodynamic analysis of microchannel heat sinks: A review, Renewable and Sustainable Energy Reviews, 21 (2013) 614-622.
[12] A. Phillips, MacLean's, (1988) 18-19.
[13] A. Husain, S.M. Kim, K.Y. Kim, Performance analysis and design optimization of micro-jet impingement heat sink, Heat and Mass Transfer/Waerme- und Stoffuebertragung, 49(11) (2013) 1613-1624.
[14] M. Asadi, G. Xie, B. Sunden, A review of heat transfer and pressure drop characteristics of single and two-phase microchannels, International Journal of Heat and Mass Transfer, 79 (2014) 34-53.
[15] R. Kiflemariam, C.X. Lin, Numerical simulation of integrated liquid cooling and thermoelectric generation for self-cooling of electronic devices, International Journal of Thermal Sciences, 94 (2015) 193-203.
[16] M.F. Al-Rjoub, A.K. Roy, S. Ganguli, R.K. Banerjee, Assessment of an active-cooling micro-channel heat sink device, using electro-osmotic flow, International Journal of Heat and Mass Transfer, 54(21-22) (2011) 4560-4569.
[17] J. Wu, J. Zhao, J. Lei, B. Liu, Effectiveness of nanofluid on improving the performance of microchannel heat sink, Applied Thermal Engineering, 101 (2016) 402-412.
[18] J. Wu, J. Wang, J. Chen, A heuristic algorithm for haplotype reconstruction from aligned weighted SNP fragments, International Journal of Bioinformatics Research and Applications, 9(1) (2013) 13-24.
[19] U. Akdag, S. Akcay, D. Demiral, Heat transfer enhancement with laminar pulsating nanofluid flow in a wavy channel, International Communications in Heat and Mass Transfer, 59 (2014) 17-23.

[20] M.S. Kamel, F. Lezsovits, A.M. Hussein, O. Mahian, S. Wongwises, Latest developments in boiling critical heat flux using nanofluids: A concise review, International Communications in Heat and Mass Transfer, 98 (2018) 59-66.
[21] L. Sauciuc, G. Chrysler, R. Mahajan, M. Szleper, Air-cooling extension - performance limits for processor cooling applications, in: Ninteenth Annual IEEE Semiconductor Thermal Measurement and Management Symposium, 2003., 2003, pp. 74-81.
[22] C. Bailey, Thermal Management Technologies for Electronic Packaging: Current Capabilities and Future Challenges for Modelling Tools, in: 2008 10th Electronics Packaging Technology Conference, 2008, pp. 527-532.
[23] C.S. Sharma, M.K. Tiwari, S. Zimmermann, T. Brunschwiler, G. Schlottig, B. Michel, D. Poulikakos, Energy efficient hotspot-targeted embedded liquid cooling of electronics, Applied Energy, 138 (2015) 414-422.
[24] J. Wei, Challenges in cooling design of CPU packages for high-performance servers, Heat Transfer Engineering, 29(2) (2008) 178-187.
[25] H. Zolfaghary Azizi, M. Naghashzadegan, V. Shokri, Comparison of Numerical Methods for Two-Fluid Model for Gas–Liquid Transient Flow Regime and Its Application in Slug Modeling Initiation, Iranian Journal of Science and Technology, Transactions of Mechanical Engineering, 43(4) (2019) 663-673.
[26] H.-W. Li, Y.-C. Wang, W.-P. Hong, B. Sun, Y.-L. Zhou, Analysis of parallel mini-channels' complex flow boiling and dryout dynamics based on the pressure drop signals, Experimental Thermal and Fluid Science, 110 (2020) 109944.
[27] A. Cioncolini, J.R. Thome, Void fraction prediction in annular two-phase flow, International Journal of Multiphase Flow, 43 (2012) 72-84.
[28] T. Hibiki, K. Mao, T. Ozaki, Development of void fraction-quality correlation for two-phase flow in horizontal and vertical tube bundles, Progress in Nuclear Energy, 97 (2017) 38-52.
[29] Z. Yang, Z. Dang, X. Yang, M. Ishii, J. Shan, Downward two phase flow experiment and general flow regime transition criteria for various pipe sizes, International Journal of Heat and Mass Transfer, 125 (2018) 179-189.
[30] T. Layssac, S. Lips, R. Revellin, Experimental study of flow boiling in an inclined mini-channel: Effect of inclination on flow pattern transitions and pressure drops, Experimental Thermal and Fluid Science, 98 (2018) 621-633.
[31] A. Iqbal, M. Pandey, A simple methodology to incorporate flashing and variation of thermophysical properties for flow boiling pressure drop in a microchannel, International Journal of Thermal Sciences, 132 (2018) 137-145.
[32] Y. Zhao, Q. Bi, Y. Yuan, H. Lv, Void fraction measurement in steam–water two-phase flow using the gamma ray attenuation under high pressure and high temperature evaporating conditions, Flow Measurement and Instrumentation, 49 (2016) 18-30.
[33] E. Nazemi, S.A.H. Feghhi, G.H. Roshani, R. Gholipour Peyvandi, S. Setayeshi, Precise Void Fraction Measurement in Two-phase Flows Independent of the Flow Regime Using Gamma-ray Attenuation, Nuclear Engineering and Technology, 48(1) (2016) 64-71.
[34] J. Li, W. Deng, G. Yan, Improving quick cooling performance of a R410A split air conditioner during startup by actively controlling refrigerant mass migration, Applied Thermal Engineering, 128 (2018) 141-150.
[35] A.C. van Eckeveld, E. Gotfredsen, J. Westerweel, C. Poelma, Annular two-phase flow in vertical smooth and corrugated pipes, International Journal of Multiphase Flow, 109 (2018) 150-163.
[36] T. Wen, H. Zhan, D. Zhang, Flow boiling heat transfer in mini channel with serrated fins: Experimental investigation and development of new correlation, International Journal of Heat and Mass Transfer, 128 (2019) 1081-1094.
[37] S. Raj, A. Shukla, M. Pathak, M.K. Khan, A novel stepped microchannel for performance enhancement in flow boiling, International Journal of Heat and Mass Transfer, 144 (2019) 118611.

[38] A.H. Al-Zaidi, M.M. Mahmoud, T.G. Karayiannis, Flow boiling of HFE-7100 in microchannels: Experimental study and comparison with correlations, International Journal of Heat and Mass Transfer, 140 (2019) 100-128.
[39] C.-M. Yang, P. Hrnjak, Effect of helical micro-fins on two-phase flow behavior of R410A evaporating in horizontal round tubes obtained through visualization, International Journal of Heat and Mass Transfer, 144 (2019) 118654.
[40] V.P. Carey, Liquid vapor phase change phenomena: an introduction to the thermophysics of vaporization and condensation processes in heat transfer equipment, CRC Press, 2018.
[41] M. Gui, W. Tian, D. Wu, R. Chen, G.H. Su, S. Qiu, Development of a three-field mechanistic model for dryout prediction in annular flow, Annals of Nuclear Energy, 135 (2020) 106978.
[42] X. Li, L. Jia, C. Dang, Z. An, Q. Huang, Visualization of R134a flow boiling in micro-channels to establish a novel bubbly-slug flow transition criterion, Experimental Thermal and Fluid Science, 91 (2018) 230-244.
[43] I.F. Okafor, J. Dirker, J.P. Meyer, Influence of non-uniform heat flux distributions on the secondary flow, convective heat transfer and friction factors for a parabolic trough solar collector type absorber tube, Renewable Energy, 108 (2017) 287-302.
[44] W. Li, Z. Chen, J. Li, K. Sheng, J. Zhu, Subcooled flow boiling on hydrophilic and super-hydrophilic surfaces in microchannel under different orientations, International Journal of Heat and Mass Transfer, 129 (2019) 635-649.
[45] J. Barber, K. Sefiane, D. Brutin, L. Tadrist, Hydrodynamics and heat transfer during flow boiling instabilities in a single microchannel, Applied Thermal Engineering, 29(7) (2009) 1299-1308.
[46] Z.-Q. Yang, G.-F. Chen, X.-R. Zhuang, Q.-L. Song, Z. Deng, J. Shen, M.-Q. Gong, A new flow pattern map for flow boiling of R1234ze(E) in a horizontal tube, International Journal of Multiphase Flow, 98 (2018) 24-35.
[47] Q. Song, G. Chen, Z. Yang, H. Wang, M. Gong, New adiabatic and condensation two-phase flow pattern maps of R14 in a horizontal tube, International Journal of Heat and Mass Transfer, 127 (2018) 910-924.
[48] J. Tan, J. Jing, H. Hu, X. You, Experimental study of the factors affecting the flow pattern transition in horizontal oil–water flow, Experimental Thermal and Fluid Science, 98 (2018) 534-545.
[49] J. Liu, J. Liu, R. Li, X. Xu, Experimental study on flow boiling characteristics in a high aspect ratio vertical rectangular mini-channel under low heat and mass flux, Experimental Thermal and Fluid Science, 98 (2018) 146-157.
[50] V. Kumar, Vikash, K.D.P. Nigam, Multiphase fluid flow and heat transfer characteristics in microchannels, Chemical Engineering Science, 169 (2017) 34-66.
[51] L. Liu, B. Bai, A mechanistic model for the prediction of swirling annular flow pattern transition, Chemical Engineering Science, 199 (2019) 405-416.
[52] F. Ronshin, E. Chinnov, Experimental characterization of two-phase flow patterns in a slit microchannel, Experimental Thermal and Fluid Science, 103 (2019) 262-273.
[53] V.S. Chalgeri, J.H. Jeong, Flow patterns of vertically upward and downward air-water two-phase flow in a narrow rectangular channel, International Journal of Heat and Mass Transfer, 128 (2019) 934-953.
[54] J. Barber, D. Brutin, K. Sefiane, L. Tadrist, Bubble confinement in flow boiling of FC-72 in a “rectangular” microchannel of high aspect ratio, Experimental Thermal and Fluid Science, 34(8) (2010) 1375-1388.
[55] Z. Bao, D. Fletcher, B. Haynes, Flow boiling heat transfer of Freon R11 and HCFC123 in narro passages, International Jounral of Heat and Mass Transfer, (43) (2000) 3347-3358.
[56] G. Lazarek, S. Black, Evaporative heat transfer, pressure drop and critical heat flux in a small vertical tube with R-113, International Journal of Heat Mass Transfer, 7(25) (1982) 945-960.
[57] S.G. Kandlikar, Fundamental issues related to flow boiling in minichannels and microchannels, Experimental Thermal and Fluid Science, 26(2) (2002) 389-407.

[58] H.J. Kim, L. Liebenberg, A.M. Jacobi, Flow visualization of two-phase R-245fa at low mass flux in a plate heat exchanger near the micro-macroscale transition, Science and Technology for the Built Environment, 25(10) (2019) 1292-1301.
[59] W. Li, Z. Wu, A general criterion for evaporative heat transfer in micro/mini-channels, International Journal of Heat and Mass Transfer, 53(9-10) (2010) 1967-1976.
[60] H. Jin Kim, L. Liebenberg, A.M. Jacobi, Convective Boiling of R-134a Near the Micro-Macroscale Transition Inside a Vertical Brazed Plate Heat Exchanger, Journal of Heat Transfer, 140(9) (2018).
[61] S.S. Mehendale, A.M. Jacobi, R.K. Shah, Fluid Flow and Heat Transfer at Micro- and Meso-Scales With Application to Heat Exchanger Design, Applied Mechanics Reviews, 53(7) (2000) 175-193.
[62] P.A. Kew, K. Cornwell, Correlations for the prediction of boiling heat transfer in small-diameter channels, Applied Thermal Engineering, 17(8) (1997) 705-715.
[63] C.L. Ong, J.R. Thome, Macro-to-microchannel transition in two-phase flow: Part 1 - Two-phase flow patterns and film thickness measurements, Experimental Thermal and Fluid Science, 35(1) (2011) 37-47.
[64] C.B. Tibiriçá, D.M. Rocha, I.L.S. Sueth, G. Bochio, G.K.K. Shimizu, M.C. Barbosa, S.d.S. Ferreira, A complete set of simple and optimized correlations for microchannel flow boiling and two-phase flow applications, Applied Thermal Engineering, 126 (2017) 774-795.
[65] J.M. Li, B.X. Wang, Size effect on two-phase regime for condensation in micro/mini tubes, Heat Transfer - Asian Research, 32(1) (2003) 65-71.
[66] L. Cheng, D. Mewes, Review of two-phase flow and flow boiling of mixtures in small and mini channels, International Journal of Multiphase Flow, 32(2) (2006) 183-207.
[67] M.M. Mahmoud, T.G. Karayiannis, Heat transfer correlation for flow boiling in small to micro tubes, International Journal of Heat and Mass Transfer, 66 (2013) 553-574.
[68] L. Cheng, G. Xia, Fundamental issues, mechanisms and models of flow boiling heat transfer in microscale channels, International Journal of Heat and Mass Transfer, 108 (2017) 97-127.
[69] D. Barnea, Y. Luninski, Y. Taitel, Flow pattern in horizontal and vertical two phase flow in small diameter pipes, The Canadian Journal of Chemical Engineering, 61(5) (1983) 617-620.
[70] N. Brauner, A. Ullmann, The Prediction of Flow Boiling Maps in Minichannels, 4th Japanese–European Two-Phase Flow Group Meeting, in, Kyoto, 2006.
[71] S. Saisorn, P. Wongpromma, S. Wongwises, The difference in flow pattern, heat transfer and pressure drop characteristics of mini-channel flow boiling in horizontal and vertical orientations, International Journal of Multiphase Flow, 101 (2018) 97-112.
[72] N. Brauner, D.M. Maron, Identification of the range of 'small diameters' conduits, regarding two-phase flow pattern transitions, International Communications in Heat and Mass Transfer, 19(1) (1992) 29-39.
[73] Z.Y. Bao, D.F. Fletcher, B.S. Haynes, An experimental study of gas–liquid flow in a narrow conduit, International Journal of Heat and Mass Transfer, 43(13) (2000) 2313-2324.
[74] D. Bogojevic, K. Sefiane, A.J. Walton, H. Lin, G. Cummins, D.B.R. Kenning, T.G. Karayiannis, Experimental investigation of non-uniform heating effect on flow boiling instabilities in a microchannel-based heat sink, International Journal of Thermal Sciences, 50(3) (2011) 309-324.
[75] T. Alam, P.S. Lee, C.R. Yap, L. Jin, Experimental investigation of local flow boiling heat transfer and pressure drop characteristics in microgap channel, International Journal of Multiphase Flow, 42 (2012) 164-174.
[76] P.-S. Lee, S.V. Garimella, Saturated flow boiling heat transfer and pressure drop in silicon microchannel arrays, International Journal of Heat and Mass Transfer, 51(3-4) (2008) 789-806.
[77] H. Pu, S. Li, M. Dong, S. Jiao, Y. Wang, Y. Shang, Convective heat transfer and flow resistance characteristics of supercritical pressure hydrocarbon fuel in a horizontal rectangular mini-channel, Experimental Thermal and Fluid Science, 108 (2019) 39-53.
[78] M. Law, P.-S. Lee, K. Balasubramanian, Experimental investigation of flow boiling heat transfer in novel oblique-finned microchannels, International Journal of Heat and Mass Transfer, 76 (2014) 419-431.

[79] D. Zhong, J. Sun, J.a. Meng, Z. Li, Experimental study of downward facing boiling on a structured hemispherical surface, Applied Thermal Engineering, 134 (2018) 594-602.
[80] T. Layssac, S. Lips, R. Revellin, Effect of inclination on heat transfer coefficient during flow boiling in a mini-channel, International Journal of Heat and Mass Transfer, 132 (2019) 508-518.
[81] S. Dall'Olio, M. Marengo, Boiling of R134a inside a glass minichannel. A new statistical approach of flow pattern characterization based on flow visualization, International Journal of Heat and Mass Transfer, 55(4) (2012) 1048-1065.
[82] Y.A. Çengel, A.J. Ghajar, Heat and mass transfer : fundamentals & applications, Fifth edition. ed., McGraw Hill Education, New York, NY, 2015.
[83] Y. Fan, Y. Li, Q. Wang, S. Yin, TIV and PIV based natural convection study over a square flat plate under stable stratification, International Journal of Heat and Mass Transfer, 140 (2019) 660-670.
[84] R.D. Clear, L. Gartland, F.C. Winkelmann, An empirical correlation for the outside convective air-film coefficient for horizontal roofs, Energy and Buildings, 35(8) (2003) 797-811.
[85] W.M. Lewandowski, M. Ryms, H. Denda, E. Klugmann-Radziemska, Possibility of thermal imaging use in studies of natural convection heat transfer on the example of an isothermal vertical plate, International Journal of Heat and Mass Transfer, 78 (2014) 1232-1242.
[86] R. Sun, G. Song, D. Zhang, J. Deng, G.H. Su, F.A. Kulacki, W. Tian, S. Qiu, Experimental study of single-phase flow and heat transfer in rectangular channels under uniform and non-uniform heating, Experimental Thermal and Fluid Science, 114 (2020) 110055.
[87] J.F. Cerón, J. Pérez-García, J.P. Solano, A. García, R. Herrero-Martín, A coupled numerical model for tube-on-sheet flat-plate solar liquid collectors. Analysis and validation of the heat transfer mechanisms, Applied Energy, 140 (2015) 275-287.
[88] O.S. Al-Yahia, Y.J. Lee, D. Jo, Effect of transverse power distribution on the ONB location in the subcooled boiling flow, Annals of Nuclear Energy, 100 (2017) 98-106.
[89] J.P. Abraham, E.M. Sparrow, W.J. Minkowycz, Internal-flow Nusselt numbers for the low-Reynolds-number end of the laminar-to-turbulent transition regime, International Journal of Heat and Mass Transfer, 54(1) (2011) 584-588.
[90] J. Dirker, J.P. Meyer, D.V. Garach, Inlet flow effects in micro-channels in the laminar and transitional regimes on single-phase heat transfer coefficients and friction factors, International Journal of Heat and Mass Transfer, 77 (2014) 612-626.
[91] M. Everts, J.P. Meyer, Laminar hydrodynamic and thermal entrance lengths for simultaneously hydrodynamically and thermally developing forced and mixed convective flows in horizontal tubes, Experimental Thermal and Fluid Science, 118 (2020) 110153.
[92] J.P. Meyer, M. Everts, Chapter Three - A review of the recent developments in laminar, transitional, quasi-turbulent and turbulent forced and mixed convective flow through horizontal tubes, in: E.M. Sparrow, J.P. Abraham, J.M. Gorman, W.J. Minkowycz (Eds.) Advances in Heat Transfer, Elsevier, 2019, pp. 131-205.
[93] F. Durst, S. Ray, B. Ünsal, O.A. Bayoumi, The development lengths of laminar pipe and channel flows, Journal of Fluids Engineering, Transactions of the ASME, 127(6) (2005) 1154-1160.
[94] R.K. Shah, A.L. London, Laminar flow forced convection in ducts: a source book for compact heat exchanger analytical data, Academic press, 2014.
[95] T.V. Nguyen, Laminar heat transfer for thermally developing flow in ducts, International Journal of Heat and Mass Transfer, 35(7) (1992) 1733-1741.
[96] M. Everts, S. Bhattacharyya, A.I. Bashir, J.P. Meyer, Heat transfer characteristics of assisting and opposing laminar flow through a vertical circular tube at low Reynolds numbers, Applied Thermal Engineering, 179 (2020) 115696.
[97] G. Wang, L. Hao, P. Cheng, An experimental and numerical study of forced convection in a microchannel with negligible axial heat conduction, International Journal of Heat and Mass Transfer, 52(3) (2009) 1070-1074.

[98] J.P. Abraham, E.M. Sparrow, J.C.K. Tong, Heat transfer in all pipe flow regimes: laminar, transitional/intermittent, and turbulent, International Journal of Heat and Mass Transfer, 52(3) (2009) 557-563.
[99] B. Mehta, S. Khandekar, Infra-red thermography of laminar heat transfer during early thermal development inside a square mini-channel, Experimental Thermal and Fluid Science, 42 (2012) 219-229.
[100] Z.H. Liang, Y. Wen, C. Gao, W.X. Tian, Y.W. Wu, G.H. Su, S.Z. Qiu, Experimental investigation on flow and heat transfer characteristics of single-phase flow with simulated neutronic feedback in narrow rectangular channel, Nuclear Engineering and Design, 248 (2012) 82-92.
[101] A. Abdollahi, S.E. Norris, R.N. Sharma, Fluid flow and heat transfer of liquid-liquid Taylor flow in square microchannels, Applied Thermal Engineering, 172 (2020) 115123.
[102] P.-S. Lee, S.V. Garimella, D. Liu, Investigation of heat transfer in rectangular microchannels, International Journal of Heat and Mass Transfer, 48(9) (2005) 1688-1704.
[103] P. Wibulswas, Laminar-flow heat-transfer in non-circular ducts, University of London, 1966.
[104] R.J. Philips, Microchannel heat sinks, Massachusetts Institute of Technology, (1987).
[105] P.-S. Lee, S.V. Garimella, Thermally developing flow and heat transfer in rectangular microchannels of different aspect ratios, International Journal of Heat and Mass Transfer, 49(17) (2006) 3060-3067.
[106] J.P. Hartnett, M. Kostic, Heat transfer to Newtonian and non-Newtonian fluids in rectangular ducts, in: Advances in heat transfer, Elsevier, 1989, pp. 247-356.
[107] L. Su, Z. Duan, B. He, H. Ma, X. Ning, G. Ding, Y. Cao, Heat transfer characteristics of thermally developing flow in rectangular microchannels with constant wall temperature, International Journal of Thermal Sciences, 155 (2020) 106412.
[108] S. Osman, M. Sharifpur, J.P. Meyer, Experimental investigation of convection heat transfer in the transition flow regime of aluminium oxide-water nanofluids in a rectangular channel, International Journal of Heat and Mass Transfer, 133 (2019) 895-902.
[109] Y.Q. Xie, J.Z. Yu, Z.H. Zhao, Experimental investigation of flow and heat transfer for the ethanol-water solution and FC-72 in rectangular microchannels, Heat and Mass Transfer, 41(8) (2005) 695-702.
[110] J.P. Meyer, M. Everts, N. Coetzee, K. Grote, M. Steyn, Heat transfer coefficients of laminar, transitional, quasi-turbulent and turbulent flow in circular tubes, International Communications in Heat and Mass Transfer, 105 (2019) 84-106.
[111] A.I. Bashir, M. Everts, R. Bennacer, J.P. Meyer, Single-phase forced convection heat transfer and pressure drop in circular tubes in the laminar and transitional flow regimes, Experimental Thermal and Fluid Science, 109 (2019) 109891.
[112] J.P. Meyer, A.I. Bashir, M. Everts, Single-phase mixed convective heat transfer and pressure drop in the laminar and transitional flow regimes in smooth inclined tubes heated at a constant heat flux, Experimental Thermal and Fluid Science, 109 (2019) 109890.
[113] C. Wang, J. Yu, S. Lin, An experimental study of convective boiling refigerants R-22 and R-410A, in: ASHRAE Transaction, Toronto, 1998, pp. 1144-1150.
[114] X. Li, L. Jia, L. Yin, Z. An, A revised correlation based on heat transfer model of slug flow in mini/micro-channels, Heat and Mass Transfer, 54(1) (2018) 25-36.
[115] Y. Zhang, R. Tian, X. Dai, D. Wang, Y. Ma, H. Li, L. Shi, Experimental study of R134a flow boiling in a horizontal tube for evaporator design under typical Organic Rankine Cycle pressures, International Journal of Heat and Fluid Flow, 71 (2018) 210-219.
[116] T.G. Karayiannis, M.M. Mahmoud, Flow boiling in microchannels: Fundamentals and applications, Applied Thermal Engineering, 115 (2017) 1372-1397.
[117] R. Charnay, R. Revellin, J. Bonjour, Flow boiling heat transfer in minichannels at high saturation temperatures: Part I – Experimental investigation and analysis of the heat transfer mechanisms, International Journal of Heat and Mass Transfer, 87 (2015) 636-652.

[118] Q. Lu, D. Chen, C. Li, X. He, Experimental investigation on flow boiling heat transfer in conventional and mini vertical channels, International Journal of Heat and Mass Transfer, 107 (2017) 225-243.
[119] N. Kattan, J.R. Thome, D. Favrat, Flow boiling in horizontal tubes: Part 2-new heat transfer data for five refrigerants, Journal of Heat Transfer, 120(1) (1998) 148-155.
[120] J.S. Jabardo, M. McLinden, R. Radermacher, D. Didion, A study of flow boiling heat transfer with refrigerant mixtures, Heat Mass Transfer, 9(32) (1989) 1751-1764.
[121] C.Y. Park, P.S. Hrnjak, CO2 and R410A flow boiling heat transfer, pressure drop, and flow pattern at low temperatures in a horizontal smooth tube, International Journal of Refrigeration, 30(1) (2007) 166-178.
[122] S. Saisorn, J. Kaew-On, S. Wongwises, Two-phase flow of R-134a refrigerant during flow boiling through a horizontal circular mini-channel, Experimental Thermal and Fluid Science, 35(6) (2011) 887-895.
[123] Q. Yang, B. Shu, J. Wang, Y. Guo, Experimental investigation on flow boiling heat transfer and flow patterns in a single micro-channel with large mass velocity, Experimental Thermal and Fluid Science, 91 (2018) 283-291.
[124] W. Huang, Z. Wu, P. Cheng, Heat and mass transfer characteristic of vertical falling film generator with annular structure for ammonia-water system, Journal of Renewable and Sustainable Energy, 11(6) (2019) 064701.
[125] D. Jige, N. Inoue, Boiling heat transfer, pressure drop, and flow pattern in a horizontal square minichannel, International Journal of Heat and Fluid Flow, 78 (2019) 108433.
[126] Y. Wang, J.-h. Shin, C. Woodcock, X. Yu, Y. Peles, Local, transient heat transfer measurements for flow boiling in a microchannel with a pin fin, International Journal of Heat and Mass Transfer, 134 (2019) 377-387.
[127] T.N. Tran, M.W. Wambsganss, D.M. France, Small circular and rectangular channel boiling with two refrigerants, International Journal of Multiphase Flow, 22(3) (1996) 485-498.
[128] S. Lin, P. Kew, K. Cornwell, Two-phase heat transfer to a refrigerant in a 1 mm diameter tubes, International Journal of Refrigeration, 1(24) (2001) 51-56.
[129] J.R. Thome, State-of-the-art overview of boiling and two-phase flows in microchannels, Heat transfer engineering, 27(9) (2006) 4-19.
[130] A. Greco, G.P. Vanoli, Flow boiling heat transfer with HFC mixtures in a smooth horizontal tube. Part I: Experimental investigations, Experimental Thermal and Fluid Science, 29(2) (2005) 189-198.
[131] X.F. Peng, H.Y. Hu, B.X. Wang, Boiling nucleation during liquid flow in microchannels, International Journal of Heat and Mass Transfer, 41(1) (1998) 101-106.
[132] S.J. Hong, X. Zheng, C.W. Park, Enhanced flow boiling heat transfer characteristics of R134a on graphene-Cu nanocomposite coating on copper substrate, International Communications in Heat and Mass Transfer, 108 (2019) 104343.
[133] P. Vasileiadou, K. Sefiane, T.G. Karayiannis, J.R.E. Christy, Flow boiling of ethanol/water binary mixture in a square mini-channel, Applied Thermal Engineering, 127 (2017) 1617-1626.
[134] G.A. Longo, S. Mancin, G. Righetti, C. Zilio, R1234yf and R1234ze(E) as environmentally friendly replacements of R134a: Assessing flow boiling on an experimental basis, International Journal of Refrigeration, 108 (2019) 336-346.
[135] G. Lillo, R. Mastrullo, A.W. Mauro, F. Pelella, L. Viscito, Experimental thermal and hydraulic characterization of R448A and comparison with R404A during flow boiling, Applied Thermal Engineering, 161 (2019) 114146.
[136] B. Jakubowska, D. Mikielewicz, M. Klugmann, Experimental study and comparison with predictive methods for flow boiling heat transfer coefficient of HFE7000, International Journal of Heat and Mass Transfer, 142 (2019) 118307.

[137] M. Amaranatha Raju, T.P. Ashok Babu, C. Ranganayakulu, Investigation of flow boiling heat transfer and pressure drop of R134a in a rectangular channel with wavy fin, International Journal of Thermal Sciences, 147 (2020) 106055.
[138] C.-M. Yang, P. Hrnjak, Visualization of two-phase flow of R410A in horizontal smooth and axial micro-finned tubes, International Journal of Heat and Mass Transfer, 138 (2019) 49-58.
[139] R. Mastrullo, A.W. Mauro, L. Viscito, Flow boiling of R452A: Heat transfer data, dry-out characteristics and a correlation, Experimental Thermal and Fluid Science, 105 (2019) 247-260.
[140] L. Pietro Maria Colombo, A. Lucchini, T. Nhan Phan, L. Molinaroli, A. Niro, Design and assessment of an experimental facility for the characterization of flow boiling of azeotropic refrigerants in horizontal tubes, Journal of Physics: Conference Series, 1224 (2019) 012037.
[141] B. Citarella, G. Lillo, R. Mastrullo, A.W. Mauro, L. Viscito, Experimental investigation on flow boiling heat transfer and pressure drop of refrigerants R32 and R290 in a stainless steel horizontal tube, Journal of Physics: Conference Series, 1224 (2019) 012041.
[142] 3M, 3M Fluorinert Electronic Liquid FC-72 TDS_FINAL.pdf, (2019).
[143] L. Zhang, Y. Wang, Z. Yu, Regulation of gas-liquid stratified flow boiling dynamic instabilities in horizontal tube: Effects of heat load distribution and wall thermal capacity, International Journal of Heat and Mass Transfer, 127 (2018) 426-436.
[144] T.A. Kingston, J.A. Weibel, S.V. Garimella, An experimental method for controlled generation and characterization of microchannel slug flow boiling, International Journal of Heat and Mass Transfer, 106 (2017) 619-628.
[145] T.A. Kingston, J.A. Weibel, S.V. Garimella, Quantitative Visualization of Vapor Bubble Growth in Diabatic Vapor-Liquid Microchannel Slug Flow, in: ASME 2015 International Technical Conference and Exhibition on Packaging and Integration of Electronic and Photonic Microsystems collocated with the ASME 2015 13th International Conference on Nanochannels, Microchannels, and Minichannels, 2015.
[146] O.S. Al-Yahia, T. Kim, D. Jo, Flow Instability (FI) for subcooled flow boiling through a narrow rectangular channel under transversely uniform and non-uniform heat flux, International Journal of Heat and Mass Transfer, 125 (2018) 116-128.
[147] G. Zhu, Q. Bi, J. Yan, Q. Yuan, H. Lv, H. Pan, Heat Transfer Charactersitics of Subcooled Water Flow Boiling in CIrcular Channels with Non-Uniform Heating Fluxes, in, The American Society of Mechanical Engineers, Charlotte, 2016.
[148] W. Li, Y. Lin, K. Zhou, J. Li, J. Zhu, Local heat transfer of saturated flow boiling in vertical narrow microchannel, International Journal of Thermal Sciences, 145 (2019) 105996.
[149] A. Radwan, S. Ookawara, M. Ahmed, Thermal management of concentrator photovoltaic systems using two-phase flow boiling in double-layer microchannel heat sinks, Applied Energy, 241 (2019) 404-419.
[150] R. Ajith Krishnan, K.R. Balasubramanian, S. Suresh, Experimental investigation of the effect of heat sink orientation on subcooled flow boiling performance in a rectangular microgap channel, International Journal of Heat and Mass Transfer, 120 (2018) 1341-1357.
[151] R. Ajith Krishnan, K.R. Balasubramanian, S. Suresh, The effect of heating area orientation on flow boiling performance in microchannels heat sink under subcooled condition, International Journal of Heat and Mass Transfer, 110 (2017) 276-293.
[152] C.R. Kharangate, L.E. O'Neill, I. Mudawar, Effects of two-phase inlet quality, mass velocity, flow orientation, and heating perimeter on flow boiling in a rectangular channel: Part 1 – Two-phase flow and heat transfer results, International Journal of Heat and Mass Transfer, 103 (2016) 1261-1279.
[153] M. Piasecka, B. Maciejewska, Heat transfer coefficient during flow boiling in a minichannel at variable spatial orientation, Experimental Thermal and Fluid Science, 68 (2015) 459-467.
[154] K. Strąk, M. Piasecka, B. Maciejewska, Spatial orientation as a factor in flow boiling heat transfer of cooling liquids in enhanced surface minichannels, International Journal of Heat and Mass Transfer, 117 (2018) 375-387.

[155] Q. Huang, L. Jia, C. Dang, L. Yang, Experimental Study on Flow Boiling of Deionized Water in a Horizontal Long Small Channel, Journal of Thermal Science, 27(2) (2018) 157-166.
[156] J.D. de Oliveira, J.C. Passos, J.B. Copetti, C.W.M. van der Geld, Flow boiling heat transfer of propane in 1.0 mm tube, Experimental Thermal and Fluid Science, 96 (2018) 243-256.
[157] G. Lillo, R. Mastrullo, A.W. Mauro, L. Viscito, Flow boiling heat transfer, dry-out vapor quality and pressure drop of propane (R290): Experiments and assessment of predictive methods, International Journal of Heat and Mass Transfer, 126 (2018) 1236-1252.
[158] Y. Gao, S. Shao, B. Zhan, Y. Chen, C. Tian, Heat transfer and pressure drop characteristics of ammonia during flow boiling inside a horizontal small diameter tube, International Journal of Heat and Mass Transfer, 127 (2018) 981-996.
[159] S. Wang, H.-H. Chen, C.-L. Chen, Enhanced flow boiling in silicon nanowire-coated manifold microchannels, Applied Thermal Engineering, 148 (2019) 1043-1057.
[160] J. Barber, D. Brutin, K. Sefiane, J.L. Gardarein, L. Tadrist, Unsteady-state fluctuations analysis during bubble growth in a “rectangular” microchannel, International Journal of Heat and Mass Transfer, 54(23-24) (2011) 4784-4795.
[161] S. Korniliou, C. Mackenzie-Dover, J.R.E. Christy, S. Harmand, A.J. Walton, K. Sefiane, Two-dimensional heat transfer coefficients with simultaneous flow visualisations during two-phase flow boiling in a PDMS microchannel, Applied Thermal Engineering, 130 (2018) 624-636.
[162] Y. Wang, K. Sefiane, Effects of heat flux, vapour quality, channel hydraulic diameter on flow boiling heat transfer in variable aspect ratio micro-channels using transparent heating, International Journal of Heat and Mass Transfer, 55(9-10) (2012) 2235-2243.
[163] Y. Wang, K. Sefiane, S. Harmand, Flow boiling in high-aspect ratio mini- and micro-channels with FC-72 and ethanol: Experimental results and heat transfer correlation assessments, Experimental Thermal and Fluid Science, 36 (2012) 93-106.
[164] H. Wang, Z. Hu, H. Gu, Y. Luo, R. Tang, T. Chen, Heat transfer characteristic of water at near critical pressure in circumferentially non-uniformly heated vertical tubes, International Journal of Thermal Sciences, 54 (2012) 167-175.
[165] Y. Liu, W. Sun, W. Wu, S. Wang, Gas-liquid two-phase flow distribution in parallel micro-channels with different header and channels’ orientations, International Journal of Heat and Mass Transfer, 112 (2017) 767-778.
[166] M. Mameli, V. Manno, S. Filippeschi, M. Marengo, Thermal instability of a Closed Loop Pulsating Heat Pipe: Combined effect of orientation and filling ratio, Experimental Thermal and Fluid Science, 59 (2014) 222-229.
[167] D. Lokhat, A.K. Domah, K. Padayachee, A. Baboolal, D. Ramjugernath, Gas–liquid mass transfer in a falling film microreactor: Effect of reactor orientation on liquid-side mass transfer coefficient, Chemical Engineering Science, 155 (2016) 38-44.
[168] X. Mingchen, J. Li, D. Chao, P. Qi, The effect of heating direction on flow boiling heat transfer of R134a in Micro-channels, Thermal Science, 26(2) (2017) 166-147.
[169] H. Zhang, I. Mudawar, M.M. Hasan, Application of Flow Boiling for Thermal Management of Electronics in Microgravity and Reduced-Gravity Space Systems, IEEE Transactions on Components and Packaging Technologies, 32(2) (2009) 466-477.
[170] G.R. D M. Iceri, G Caruso, F M. Forino, L Saraceno, G Zummo, EXPERIMENTAL INVESTIGATION OF FLOW BOILING IN A 4.0 mm TUBE AT DIFFERENT GRAVITY CONDITIONS: 0g, 1g, AND 2g, International Heat Transfer Conference 16, (2018).
[171] F.L. Robinson, A. Bar-Cohen, Orientation Effects in Two-Phase Microgap Flow, in: ASME 2018 International Technical Conference and Exhibition on Packaging and Integration of Electronic and Photonic Microsystems, 2018.
[172] D. Paul, S. Singh, S. Mishra, Stability analysis of parallel channels in flow boiling system: Flow maldistribution and density wave oscillations, Chemical Engineering Science, 212 (2020) 115316.
[173] M. Ozawa, H. Umekawa, K. Mishima, T. Hibiki, Y. Saito, CHF in oscillatory flow boiling channels, Chemical Engineering Research and Design, 79(4) (2001) 389-401.

[174] T. Zhang, T. Tong, J.-Y. Chang, Y. Peles, R. Prasher, M.K. Jensen, J.T. Wen, P. Phelan, Ledinegg instability in microchannels, International Journal of Heat and Mass Transfer, 52(25-26) (2009) 5661-5674.
[175] J.A. Boure, A.E. Bergles, L.S. Tong, Review of two-phase flow instability, Nuclear Engineering and Design, 25(2) (1973) 165-192.
[176] J.S. Maulbetsch, P. Griffith, System-induced instabilities in forced convection flows with subcooled boiling, in: International Heat Transfer Conference Digital Library, Begel House Inc., 1966.
[177] Z. Jiang, Z. Ma, R. Yan, L. Zhang, W. Sun, S. Bu, L. Pan, Experimental study on the flow boiling oscillation characteristics in a rectangular multiple micro-channel, Experimental Thermal and Fluid Science, 109 (2019) 109902.
[178] P.K. Das, A.K. Das, 7 - Instability in Flow Boiling through Microchannels, in: S.K. Saha (Ed.) Microchannel Phase Change Transport Phenomena, Butterworth-Heinemann, 2016, pp. 257-286.
[179] H. Yüncü, O.T. Yildirim, S. Kakaç, Two-phase flow instabilities in a horizontal single boiling channel, Applied Scientific Research, 48(1) (1991) 83-104.
[180] W. Qu, I. Mudawar, Measurement and correlation of critical heat flux in two-phase micro-channel heat sinks, International Journal of Heat and Mass Transfer, 47(10) (2004) 2045-2059.
[181] D. Brutin, F. Topin, L. Tadrist, Experimental study of unsteady convective boiling in heated minichannels, International journal of heat and mass transfer, 46(16) (2003) 2957-2965.
[182] G.P. Celata, M. Cumo, D. Dossevi, R.T.M. Jilisen, S.K. Saha, G. Zummo, Visualisation of flow boiling heat transfer in a microtube, Heat and Mass Transfer, 47(8) (2011) 941.
[183] Y. Lv, G. Xia, L. Cheng, D. Ma, Experimental study on the pressure drop oscillation characteristics of the flow boiling instability with FC-72 in parallel rectangle microchannels, International Communications in Heat and Mass Transfer, 108 (2019) 104289.
[184] L. Zhang, E.N. Wang, K.E. Goodson, T.W. Kenny, Phase change phenomena in silicon microchannels, International journal of heat and mass transfer, 48(8) (2005) 1572-1582.
[185] X. Li, T. Hibiki, Frictional pressure drop correlation for two-phase flows in mini and micro multi-channels, Applied Thermal Engineering, 116 (2017) 316-328.
[186] R. Muwanga, I. Hassan, R. MacDonald, Characteristics of flow boiling oscillations in silicon microchannel heat sinks, Journal of Heat Transfer, 129(10) (2007) 1341-1351.
[187] C.A. Chen, T.F. Lin, W.-M. Yan, Time periodic saturated flow boiling heat transfer of R-134a in a narrow annular duct due to heat flux oscillation, International Journal of Heat and Mass Transfer, 106 (2017) 35-46.
[188] P. Balasubramanian, S.G. Kandlikar, Experimental study of flow patterns, pressure drop, and flow instabilities in parallel rectangular minichannels, Heat Transfer Engineering, 26(3) (2005) 20-27.
[189] Y. Ding, S. Kakaç, X.J. Chen, Dynamic instabilities of boiling two-phase flow in a single horizontal channel, Experimental Thermal and Fluid Science, 11(4) (1995) 327-342.
[190] J.D. Lee, S.W. Chen, C. Pan, Nonlinear dynamic analysis of parallel three uniformly heated channels with water at supercritical pressures, International Journal of Heat and Mass Transfer, 129 (2019) 903-919.
[191] A.M. Mishra, S. Singh, Non-linear stability analysis of uniformly heated parallel channels for different inclinations, Applied Thermal Engineering, 98 (2016) 1189-1200.
[192] Y. Kuang, W. Wang, J. Miao, H. Zhang, X.g. Yu, Non-linear analysis of nitrogen pressure drop instability in micro/mini-channels, International Journal of Heat and Mass Transfer, 147 (2020) 118953.
[193] S. Hong, C. Dang, E. Hihara, Experimental investigation on flow boiling in radial expanding minichannel heat sinks applied for low flow inertia condition, International Journal of Heat and Mass Transfer, 143 (2019) 118588.
[194] K.H. Chang, C. Pan, Two-phase flow instability for boiling in a microchannel heat sink, International Journal of Heat and Mass Transfer, 50(11) (2007) 2078-2088.

[195] T. Chen, S.V. Garimella, Local heat transfer distribution and effect of instabilities during flow boiling in a silicon microchannel heat sink, International Journal of Heat and Mass Transfer, 54(15) (2011) 3179-3190.
[196] S. Korniliou, C. Mackenzie-Dover, S. Harmand, G. Duursma, J.R.E. Christy, J.G. Terry, A.J. Walton, K. Sefiane, Local wall temperature mapping during flow boiling in a transparent microchannel, International Journal of Thermal Sciences, 135 (2019) 344-361.
[197] R.P. Madding, Emissivity measurement and temperature correction accuracy considerations, in: AeroSense '99, SPIE, 1999, pp. 9.
[198] L.T. Clausing, Emissivity: Understanding the difference between apparent and actual infrared temperatures, (2007).
[199] C.H. Hoang, S. Rangarajan, S. Khalili, B. Ramakrisnan, V. Radmard, Y. Hadad, S. Schiffres, B. Sammakia, Hybrid microchannel/multi-jet two-phase heat sink: A benchmark and geometry optimization study of commercial product, International Journal of Heat and Mass Transfer, 169 (2021) 120920.
[200] M.-G. Kang, Effects of water subcooling on heat transfer in vertical annuli, International Journal of Heat and Mass Transfer, 49(23) (2006) 4372-4385.
[201] Y.Y. Hsieh, L.J. Chiang, T.F. Lin, Subcooled flow boiling heat transfer of R-134a and the associated bubble characteristics in a vertical plate heat exchanger, International Journal of Heat and Mass Transfer, 45(9) (2002) 1791-1806.
[202] V.Y.S. Lee, T.G. Karayiannis, Effect of inlet subcooling on flow boiling in microchannels, Applied Thermal Engineering, 181 (2020) 115966.
[203] R. Prattipati, S. Pendyala, B.V.S.S.S. Prasad, Void fraction in helical coils during flow boiling with inlet subcooling, International Journal of Heat and Mass Transfer, 168 (2021) 120904.
[204] Y. Wang, K. Sefiane, R. Bennacer, Pressure Drop and Two Phase Flow During Boiling of FC-72 in a High Aspect Ratio Micro-Channel, (49361) (2010) 727-734.
[205] K.S. D. Bogojevica, A.J. Walton, H. Lin, G. Cummins, Two-phase flow instabilities in a silicon microchannels heat sink, International Journal of Heat and Fluid Flow, (30) (2009) 854–867.
[206] G. Hetsroni, A. Mosyak, Z. Segal, E. Pogrebnyak, Two-phase flow patterns in parallel micro-channels, International Journal of Multiphase Flow, 29(3) (2003) 341-360.
[207] J. Xu, X. Yu, W. Jin, Porous-wall microchannels generate high frequency “eye-blinking” interface oscillation, yielding ultra-stable wall temperatures, International Journal of Heat and Mass Transfer, 101 (2016) 341-353.
[208] G. Hetsroni, A. Mosyak, Z. Segal, G. Ziskind, A uniform temperature heat sink for cooling of electronic devices, International Journal of Heat and Mass Transfer, 45(16) (2002) 3275-3286.
[209] H.Y. Wu, P. Cheng, Visualization and measurements of periodic boiling in silicon microchannels, International Journal of Heat and Mass Transfer, 46(14) (2003) 2603-2614.
[210] G. Wang, P. Cheng, A.E. Bergles, Effects of inlet/outlet configurations on flow boiling instability in parallel microchannels, International Journal of Heat and Mass Transfer, 51(9) (2008) 2267-2281.
[211] D. Deng, L. Zeng, W. Sun, G. Pi, Y. Yang, Experimental study of flow boiling performance of open-ring pin fin microchannels, International Journal of Heat and Mass Transfer, 167 (2021) 120829.
[212] R.J. Moffat, Describing the uncertainties in experimental results, Experimental Thermal and Fluid Science, 1(1) (1988) 3-17.
[213] L.-C. Hsu, S.-W. Cion, K.-W. Lin, C.-C. Wang, An experimental study of inclination on the boiling heat transfer characteristics of a micro-channel heat sink using HFE-7100, International Communications in Heat and Mass Transfer, 62 (2015) 13-17.
[214] P.F.D. Dunn, Michael P, Measurement and Data Analysis for Engineering and Science, Fourth Edition (2018).

Appendix A: Data interpretation code

The code use to interpret the local heat transfer coefficients; local vapour quality; local fluid temperature, heat flux and many other parameters was calculated using a MATLAB code. This code is presented below.

```
clear all
close all
clc

tic
%% produce infrared matrix of surface

for t = 1:3
    single_phase = 0;
    voltage_input_V = 98.2;
    Ampere_input_mA = 71.4;
    volumetric_flow_rate_m3s = 107.1;
    heated_length_mm = 79;
    str_base = 'E:\R\tests\inclined\bh_inc\bl\107\100V\';
    %temppers_start = input('start time or temppers_start in 00:00:00.00
format: in '' ');
    temppers_start = '00:45:43.07';
    %IR_start = input('start time of IR in 00:00:00.00 format in '' :');
    %IR_start = '00:33:41.83';
    new_IR = 0;

    if t ==1
        IR_start = '00:45:54.12';
        output = 'output_1\';
        num = '1\';
    elseif t ==2
        IR_start = '00:47:12.39';
        output = 'output_2\';
        num = '2\';
    elseif t ==3
        IR_start = '00:48:29.77';
        output = 'output_3\';
        num = '3\';
    end
    str = strcat(str_base,num);
    str_output = strcat(str_base,output);
    folder_name = uigetdir(str);

    % str = 'D:\monster\120\hl\107\40V\1\';
    % str_output = 'D:\monster\bh\bl\214\60V\output_1\';

    heat_loss_a_p = 0;
    heat_loss_b_p = 0;
    heat_loss_a_l = 0.0392;
    heat_loss_c_l = -0.0662;

    if new_IR == 0
        x_l = 95;
        x_r = 575;
        d_len = x_r-x_l;

        y_l_u = 267;
        y_l_l = 297;
        y_r_u = 267;
        y_r_l = 297;
```

Figure 47: Data interpretation code page 1

```
d_y = (y_r_l-y_r_u);
m_u = -1*(y_l_u-y_r_u)/d_len;
m_l = -1*(y_l_l-y_r_l)/d_len;

for p = 1:d_len
    y_u(p) = m_u*(p-1)+y_l_u;
    if round(y_u(p))<y_u(p)
        y_u(p) = round(y_u(p))+1;
    else
        y_u(p) = round(y_u(p));
    end
    y_l(p) = m_l*(p-1)+y_l_l;
    if round(y_l(p))>y_l(p)
        y_l(p) = round(y_l(p))-1;
    else
        y_l(p) = round(y_l(p));
    end
end
y_u(1);
y_u(end);
y_l(1);
y_l(end);

for y = 1:d_y
    for x = 1:(d_len)
        x_position_temp(y,x) = x+x_l-1;
        y_posiition_temp(y,x) = y_u(x)+y;
    end
end

%name of the file that will be produced by the code
save_file_name = 'IRAVE.csv';
%place to start looking, remember to add \ after last word/number
%str = input('directory where to start looking for destination file:

%choose folder by clicking on it

% create a structured array with all the information form the various

% files that are produced by the infrared camera
files=dir(fullfile(folder_name,'*.mat'));
%files=dir(fullfile(folder_name,'Snap*.mat'));

count = 0;

for i = 1:length(files)
    %determine the average surface temperature between the widths
nd
    %finish and put it in a matrix

    %create location by joining the two strings
    full_location = strjoin({str,files(i).name});
    %remove space between two joined strings
    full_location = regexprep(full_location,' ','');
```

Figure 48: Data interpretation code page 2

```
            %load the .mat file of interest
            load(full_location);

            if i == 1
                [x,y] = size(Frame);
                temp_matrix = zeros(d_y,d_len);
            end

            for k = 1:(d_y)
                for l =1:(d_len)
                    temp_matrix(k,l) =
Frame(y_posiition_temp(k,l),x_position_temp(k,l))+temp_matrix(k,l);
                end
            end
            count = count +1;
            %max surface temp value transiently
            max_surface_temp_value_trans(i) = max(max(Frame));
            delta_surface_time = 60/length(files);
            surface_temp_time(i) = delta_surface_time*i;

            %max surface temp locataion transiently
            [Fx,Fy] = size(temp_matrix);

            max_Frame_temp = max(max(temp_matrix));
            for j = 1:Fx
                location_num = 0;
                for k = 1:Fy
                    if max_Frame_temp == temp_matrix(j,k)
                        location_num = location_num +1;
                        location_max_surf_temp(i,location_num) =
(j/Fx)*heated_length_mm;
                    end
                end
            end

        end

        adj_temp = temp_matrix/count;

        %create desitnation file to which the values are saved (entered by
prompt
        %at top of code
        full_file_name = strjoin({str,save_file_name});
        full_file_name = regexprep(full_file_name, ' ','');

        %save to Excel .xls format file
        csvwrite(full_file_name,adj_temp);

%         adj_temp
%         beep
%         pause

    end

    %%
```

Figure 49: Data interpretation code page 3

```
    %setting up standard experimental setup

    % full_matrix has all the various values required for the heat transfer
    % computation. First coloumn is the time matrix. Second and thrid coloum
    % are the inlet and outlet temperature respectively. Fourth coloumn is
the
    % average temperature in the channel assuming a linear increase in
    % temperature through channel CHANGE THIS WHEN USING FC-72. Fifth column
is
    % the average surface tempeature measured by the infrared camera. this
code
    % does not yet save the heat transfer coefficients in an output file

    %this code produces graphs of inlet/outlet pressure and transient heat
    %trasnfer coefficient. It also produces mass flow rate, max expected temp
    %change, actual temp change, mass flux, average heat transfer
coefficient,
    %heat flux

    %get the time step size and frequency of the equipment
    display('standard settings')

    delta_t_temp_pressure = 0.01;
    channel_depth_mm = 0.5;
    channel_width_mm = 5;
    length_of_experiment_s = 60;
    h_fg_Jkg = 88000;

    %%
    %add input numbers
    %standard_experiment = input('is this a standard experiment 0 = yes; 1=
no: ');
    standard_experiment = 0;
    if standard_experiment == 1
        delta_t_temp_pressure = input('What was the period (1/f) for temp and
pressure: ');
        channel_depth_mm = input('Depth of channel in mm: ');
        channel_width_mm = input('Width of channel in mm: ');
        length_of_experiment_s = input('length of time of experiment in s:
');
        h_fg_Jkg = input('normally 88000J/kg: ');
    end

    %input heat
    qinput_W = voltage_input_V*(Ampere_input_mA/1000); %W

    %mass flux to mass flow rate
    volumetric_flow_rate_m3s = volumetric_flow_rate_m3s/3600; %ml/s
    volumetric_flow_rate_m3s = volumetric_flow_rate_m3s/1000; %L/s
    volumetric_flow_rate_m3s = volumetric_flow_rate_m3s/1000; %m3/s
    cross_sectional_area_m2 = channel_depth_mm*channel_width_mm/1000/1000;
%m2
    channel_length_m = heated_length_mm/1000; %m

    %%
```

Figure 50: Data interpretation code page 4

```
%find temperature and pressure data
%place to start looking,
str_temppres = strcat(str,'temppres.lvm');

%create file directory
file_destination = str_temppres;
file_destination = regexprep(file_destination,' ','');
X1=dlmread(file_destination); %load

%create a resonable name for the data
Data = X1;

%split time, temp and pressure
time = X1(:,1);
temp_C = X1(:,[2,3]);
atm_temp_C = X1(:,4);

% Creating of full matrix from thermocouples
%time column
No_total_devisions = time(end)/(delta_t_temp_pressure);
t_initial = delta_t_temp_pressure;

t1 = IR_start;
t2 = temppers_start;

t_IR = datevec(t1);
t_temp = datevec(t2);

delta_t = 100*(etime(t_IR,t_temp));
delta_t_end = delta_t+(length_of_experiment_s*100);

pres_kPa = X1(delta_t:delta_t_end,[6,7]);

time_ave_matrix(1,1) = mean(temp_C(delta_t:delta_t_end,1));
time_ave_matrix(1,2) = mean(temp_C(delta_t:delta_t_end,2));
time_ave_matrix(1,3) = mean(atm_temp_C(delta_t:delta_t_end,1));

%bluk fluid temperature for FC-72
cpl_JkgC_bulk=
1014+(1.544*((time_ave_matrix(1,1)+time_ave_matrix(1,2))/2)); %barber
%p_FC72_kgm3_sat = 1740-
(2.61*((time_ave_matrix(1,1)+time_ave_matrix(1,2))/2)); %barber
p_FC72_kgm3_sp = 1740-(2.61*time_ave_matrix(1,1)); %barber
p_FC72_kgm3_sat = 13.2;
delta_2_sat_C = time_ave_matrix(1,2)-time_ave_matrix(1,1);
mass_flow_rate_kgs = volumetric_flow_rate_m3s*p_FC72_kgm3_sp; %kg/s

%%
%find surface tempearture matrix originally exported at the beginning of
%this code
%import surface tempreature matrix

str_IR = strcat(str,'IRAVE.csv');
surface_temp_values = csvread(str_IR);
```

Figure 51: Data interpretation code page 5

```
    [ys,xs] = size(surface_temp_values);

    %IR averaged in vertical direction
    IR_ave_y = zeros(1,xs);
    Delta_T_max_min_cross = zeros(1,xs);
    for i = 1:xs
        for j = 1:ys
            IR_ave_y(1,i) = surface_temp_values(j,i)+IR_ave_y(1,i);
            Delta_T_max_min_cross(1,i) = max(surface_temp_values(:,i))-
min(surface_temp_values(:,i));
        end
    end

    incre_ys = channel_width_mm/ys;
    y_position(1) = incre_ys/2;
    for i = 2:ys
        y_position(i) = y_position(i-1)+incre_ys;
    end

    %average heat transfer coefficient
    IR_ave_y = IR_ave_y/ys;
    IR_ave_y_x = mean(IR_ave_y);
    [IR_y,IR_x] = size(IR_ave_y);
    heat_absorbed_single_phase = mass_flow_rate_kgs*(time_ave_matrix(1,2)-
time_ave_matrix(1,1))*cpl_JkgC_bulk;

    act_temp = IR_ave_y;

    for i = 1:length(IR_ave_y)
        if i<10
            IR_ave_y(i) = IR_ave_y(i);
        elseif i>=10 && i<(length(IR_ave_y)-10)
            IR_ave_y(i) = (sum(IR_ave_y(i-5:(i+5))))/11;
        end
    end

    %%
    %heat loss from heat loss curved defined interms of surface temperature
    % axis indicates local heat transfer coeffiacient along the flow
direction
    % access 2 axis indicates local average heat transfer coefficient

    if single_phase == 1
        display(' ')
        display('heat calibration')
        display('input W')
        display(qinput_W)
        display('absorbed W')
        display(heat_absorbed_single_phase)
        display('atmospheric temp')
        display(time_ave_matrix(1,3))
        display('surface temp')
        display(mean(mean(surface_temp_values)))
        display('average outlet tempature')
```

Figure 52: Data interpretation code page 6

```
        display(((mean(temp_C(:,2))-mean(temp_C(:,1)))/2)+mean(temp_C(:,1)))
        stop
    end

        qinput_W_local = qinput_W/(xs);
        T_local(1) = time_ave_matrix(1,1);
        q_absorb(1) = 0;
        q_cum = 0;
        j=1;
        cpl_JkgC_bulk(1) = 1014+(1.544*(time_ave_matrix(1,1)));
        cpl_JkgC_local(1) = 1014+(1.544*(time_ave_matrix(1,1)));
        p_FC72_kgm3_sp(1) = 1740-(2.61*time_ave_matrix(1,1));
        mass_flow_rate_kgs_bulk(1) =
volumetric_flow_rate_m3s*p_FC72_kgm3_sp(1);
        for i = 1:IR_x
            if i>1 && q_cum<=heat_absorbed_single_phase
                cpl_JkgC_local(i-1) = 1014+(1.544*T_local(i-1));
                T_local(i) = T_local(i-1)+((q_absorb(i-1))/(cpl_JkgC_local(i-
1)*mass_flow_rate_kgs_bulk(i-1)));
            else
                T_local(i) = time_ave_matrix(1,2);
            end
            if i ==1
                T_local(i) = time_ave_matrix(1,1);
            end
            if T_local(i) >= time_ave_matrix(1,2)
                T_local(i) = time_ave_matrix(1,2);
            end
            D_T_atm(i) = IR_ave_y(1,i)-time_ave_matrix(1,3);
            q_loss(i) =
((heat_loss_a_p*(D_T_atm(i)^heat_loss_b_p))/(xs))+(((heat_loss_a_l*D_T_atm(i)
)+heat_loss_c_l)/xs);
            q_absorb(i) = qinput_W_local-q_loss(i);
            q_cum = (q_cum + q_absorb(i));
            D_T_ht(i) = IR_ave_y(1,i)-T_local(i);
            h_local(i) =
q_absorb(i)/(D_T_ht(i)*(channel_width_mm*heated_length_mm/1000/1000/IR_x));
            x_position_local(i) = (i/IR_x)*heated_length_mm;

            p_FC72_kgm3_bulk(i) = 1740-(2.61*T_local(i));
            mass_flow_rate_kgs_bulk(i) =
volumetric_flow_rate_m3s*p_FC72_kgm3_bulk(i);

            x_local(i) =  (q_cum-
heat_absorbed_single_phase)/(mass_flow_rate_kgs_bulk(i)*h_fg_Jkg);
            k_local(i) = 0.06-0.00011*T_local(i);
            Nu_local(i) =
h_local(i)*((4*(channel_width_mm/1000)*(channel_depth_mm/1000))/(2*((channel_
width_mm/1000)+(channel_depth_mm/1000))))/k_local(i);

            u(i) =
mass_flow_rate_kgs_bulk(i)/((channel_width_mm/1000)*(channel_depth_mm/1000)*p
_FC72_kgm3_bulk(i));
            Ri_local(i) =
(9.81*(1/((IR_ave_y(1,i)+T_local(i))/2))*(IR_ave_y(1,i)-
```

Figure 53: Data interpretation code page 7

```
T_local(i))*(2*(channel_width_mm/1000)*(channel_depth_mm/1000)))/(((channel_w
idth_mm/1000)+(channel_depth_mm/1000))*(u(i)^2));

            if T_local(i) == time_ave_matrix(1,2)
                h_local_tp(j) = h_local(i);
                q_abs_tp_x(j) = q_absorb(i);
                T_loc_tp(j) = IR_ave_y(1,i);
                x_local(i) =  (q_cum-
heat_absorbed_single_phase)/(mass_flow_rate_kgs_bulk(i)*h_fg_Jkg);

                if j == 1
                   x_start = x_position_local(i);
                end
                j = j+1;
            end

            k_local(i) = 0.06-0.00011*T_local(i);
            Nu_local(i) =
h_local(i)*((4*(channel_width_mm/1000)*(channel_depth_mm/1000))/(2*((channel_
width_mm/1000)+(channel_depth_mm/1000))))/k_local(i);

            if T_local(i)==time_ave_matrix(1,2)
                h_ave_sum_tp = sum(h_local_tp)/length(h_local_tp);
                h_ave = sum(q_abs_tp_x)/((mean(T_loc_tp)-
time_ave_matrix(1,2))*((2*(channel_width_mm+channel_depth_mm))*(heated_length
_mm-x_start)/1000/1000));
                heat_flux_absorbed_tp =
sum(q_absorb)/((channel_width_mm*(heated_length_mm-x_start)/1000/1000));
            end
        end

    time_ave_matrix(1,4) = mean(mean(surface_temp_values));

    %constants for heat transfer coefficent
    mass_flux = mass_flow_rate_kgs/cross_sectional_area_m2; %kg/m2s

    %creating of matricies for temperature and plotting
    for i = 1:((1/delta_t_temp_pressure)*length_of_experiment_s)
        time_plotting(1,i) = 0.01*i;
        pressure_in(i,1) = pres_kPa(i,1);
        pressure_out(i,1) = pres_kPa(i,2);
        D_pressure(i,1) = pressure_in(i,1)-pressure_out(i,1);
    end

    actual_temp_change_mean = time_ave_matrix(1,2)-time_ave_matrix(1,1);
    heat_flux_applied =
qinput_W/(channel_width_mm*heated_length_mm/1000/1000);
    heat_flux_absorbed =
sum(q_absorb)/(channel_width_mm*heated_length_mm/1000/1000);

    x_exit = (sum(q_absorb)-
heat_absorbed_single_phase)/(mass_flow_rate_kgs(end)*h_fg_Jkg);

    pixel_size = (heated_length_mm*channel_width_mm)/(xs*ys);
    beep
```

Figure 54: Data interpretation code page 8

```
%%
%graphing of important values
%

str_save_file_1 = strcat(str_output,'qloss_DTatm_qabsorb.jpg');
str_save_file_2 = strcat(str_output,'Tlocal_IRavey_DTht_hlocal.jpg');
str_save_file_3 = strcat(str_output,'P_inlet.jpg');
str_save_file_4 = strcat(str_output,'P_outlet.jpg');
str_save_file_5 = strcat(str_output,'Delta_P.jpg');
str_save_file_6 = strcat(str_output,'x_position.csv');
str_save_file_7 = strcat(str_output,'wall_temp_delta.csv');
str_save_file_8 = strcat(str_output,'h_local.csv');
str_save_file_9 = strcat(str_output,'Delta_P.csv');
str_save_file_10 = strcat(str_output,'h_local_vs_distance.jpg');
str_save_file_11 = strcat(str_output,'cross_section_deltaT.jpg');
str_save_file_12 = strcat(str_output,'local_quality.csv');
str_save_file_13 = strcat(str_output,'hlocalvsquality.jpg');
str_save_file_14 = strcat(str_output,'Tlocalvsquality.jpg');
str_save_file_15 = strcat(str_output,'heatlosscheck.jpg');
str_save_file_16 = strcat(str_output,'max_surface_temp_change.jpg');
str_save_file_17 = strcat(str_output,'pressure_in.csv');
str_save_file_18 = strcat(str_output,'pressure_out.csv');
str_save_file_19 = strcat(str_output,'max_surface_temp_value_trans.csv');
str_save_file_20 = strcat(str_output,'location_max_surface_temp.jpg');
str_save_file_21 = strcat(str_output,'location_max_surface_temp.csv');
str_save_file_22 = strcat(str_output,'Nu_local.jpg');
str_save_file_23 = strcat(str_output,'Ri_local.jpg');
str_save_file_24 = strcat(str_output,'Nu_local.csv');
str_save_file_25 = strcat(str_output,'Ri_local.csv');

csvwrite(str_save_file_6,x_position_local)
csvwrite(str_save_file_7,Delta_T_max_min_cross)
csvwrite(str_save_file_8,h_local)
csvwrite(str_save_file_9,D_pressure)
csvwrite(str_save_file_12,x_local)
csvwrite(str_save_file_17,pressure_in)
csvwrite(str_save_file_18,pressure_out)
csvwrite(str_save_file_19,max_surface_temp_value_trans)

h = figure(1);
hold on
subplot(2,2,1)
plot(x_position_local,q_loss)
grid on
title('Wattage loss')
xlabel('Time since start of experiment (s)')
ylabel('Power lost in W')
subplot(2,2,2)
plot(x_position_local,D_T_atm)
grid on
title('Temperature difference wall and atm')
xlabel('Time since start of experiment (s)')
ylabel('Wall-atm')
subplot(2,2,3)
plot(x_position_local,q_absorb)
grid on
```

Figure 55: Data interpretation code page 9

```
title('absorbed wattage')
xlabel('Time since start of experiment (s)')
ylabel('absorb W')
grid on
saveas(h,str_save_file_1)
hold off

h=figure(2);
hold on
subplot(2,2,1)
plot(x_position_local,T_local)
grid on
title('T local')
xlabel('distance down the channel in mm')
ylabel('T local C')
subplot(2,2,2)
plot(x_position_local,IR_ave_y)
grid on
title('IR temp')
xlabel('distance down the channel in mm')
ylabel('IR temp in C')
subplot(2,2,3)
plot(x_position_local,D_T_ht)
grid on
title('DT')
xlabel('distance down the channel in mm')
ylabel('DT in C')
subplot(2,2,4)
plot(x_position_local,h_local)
title('h local')
xlabel('distance down the channel in mm')
ylabel('h local W/m2K')
grid on
saveas(h,str_save_file_2)
hold off

h = figure(3);
hold on
title('Transient Pressure Inlet Data')
xlabel('Time since start of experiment (s)')
ylabel('Pressure change in kPa')
plot(time_plotting,pressure_in)
grid on
saveas(h,str_save_file_3)
hold off

mean_in = mean(pressure_in);
location_press_peak_in = find(pressure_in>=(mean_in+2));

peak_in = [];
for i = 1:length(location_press_peak_in)
   peak_in(i) = pressure_in(location_press_peak_in(i))-mean_in;
end

if length(peak_in)>0
    max_in = max(peak_in);
```

Figure 56: Data interpretation code page 10

```
        mean_peak_in = mean(peak_in);
    end

    mean_out = mean(pressure_out);
    location_press_peak_out = find(pressure_out>=(mean_out+2));

    peak_out = [];
    for i = 1:length(location_press_peak_out)
       peak_out(i) = pressure_out(location_press_peak_out(i))-mean_out;
    end

    if length(peak_out)>0
        max_out = max(peak_out);
        mean_peak_out = mean(peak_out);
    end

    h = figure(4);
    hold on
    title('Transient Pressure Outlet Data')
    xlabel('Time since start of experiment (s)')
    ylabel('Pressure change in kPa')
    plot(time_plotting,pressure_out)
    grid on
    saveas(h,str_save_file_4)
    hold off

    h = figure(5);
    hold on
    title('Transient Pressure Drop Data')
    xlabel('Time since start of experiment (s)')
    ylabel('Pressure change in kPa')
    plot(time_plotting,D_pressure)
    grid on
    grid on
    saveas(h,str_save_file_5)
    hold off

    h = figure(7);
    hold on
    plot(x_position_local,h_local,'.')
    grid on
    title('Heat transfer coefficient at axial positions downstream of the
inlet')
    xlabel('Distance from channel inlet in mm')
    ylabel('Local heat transfer coefficient W/m2K')
    saveas(h,str_save_file_10)
    hold off

    h = figure(8);
    hold on
    plot(x_position_local,Delta_T_max_min_cross,'.')
    grid on
    title('Delta T in a cross section')
    xlabel('Distance from channel inlet in mm')
    ylabel('max minus min temp in C')
```

Figure 57: Data interpretation code page 11

```
    saveas(h,str_save_file_11)
    hold off

    h = figure(9);
    hold on
    plot(x_local,h_local,'.')
    grid on
    title('Heat transfer coefficient at various qualities')
    xlabel('quality')
    ylabel('local heat transfer coefficient (W/mK)')
    saveas(h,str_save_file_13)
    hold off

    h = figure(10);
    hold on
    plot(x_local,T_local,'.')
    title('Local temperature vs quality check')
    xlabel('quality')
    ylabel('Local temperaturein °C')
    grid on
    saveas(h,str_save_file_14)
    hold off

    for i = 1:100
        loss_check(i) =
heat_loss_a_p*(i^heat_loss_b_p)+(heat_loss_a_l*i)+heat_loss_c_l;
        temp_check(i) = i;
    end

    h = figure(11);
    hold on
    plot(temp_check,loss_check,'.')
    title('Heat loss vs termpature curve check')
    xlabel('Delta T')
    ylabel('heat loss W')
    grid on
    saveas(h,str_save_file_15)
    hold off

    h = figure(12);
    hold on
    plot(surface_temp_time,max_surface_temp_value_trans,'.')
    title('Maximum surface temperature variability')
    ylabel('Max surface temp °C')
    xlabel('time in s')
    grid on
    saveas(h,str_save_file_16)
    hold off

    h = figure(13);
    hold on
    title('Location of max surface temp measurement')
    xlabel('time in s')
    ylabel('location of max temp in mm from inlet')
    saveas(h,str_save_file_20)
    plot(surface_temp_time(1,:),location_max_surf_temp(:,1),'b.')
```

Figure 58: Data interpretation code page 12

```
hold off

h = figure(14);
hold on
title('Nusselt Number vs quality')
xlabel('quality')
ylabel('Nusselt number local')
saveas(h,str_save_file_22)
plot(x_local,Nu_local,'b.')
hold off

h = figure(15);
hold on
title('Richardson Number vs quality')
xlabel('quality')
ylabel('Richardson number local')
saveas(h,str_save_file_23)
plot(x_local,Ri_local,'b.')
hold off

csvwrite(str_save_file_24,Nu_local)
csvwrite(str_save_file_25,Ri_local)
csvwrite(str_save_file_21,location_max_surf_temp)

display(' ')
display(' ')
display(' ')
display(' ')
display('important output values')
display('2 phase local heat transfer')
display(mean(h_local_tp))
display('2 phase average h average in cross section')
display(heat_flux_absorbed_tp)
display('DT_max')
display(max(Delta_T_max_min_cross))

if ~isempty(peak_out)
    display('Number of peaks out')
    display(length(peak_out))
    display('Peak pressure out')
    display(max_out)
    display('Mean preassure peak above average')
    display(mean_peak_out)
end

if length(peak_in)>0
    display('Number of peaks in')
    display(length(peak_in))
    display('Peak pressure in')
    display(max_in)
    display('Mean preassure peak above average')
    display(mean_peak_in)
end
%
display('heat flux applied')
display(heat_flux_applied)
```

Figure 59: Data interpretation code page 13

```
    display('effective heat flux')
    display(heat_flux_absorbed)
    time_ave_matrix(1,2)

    str
%     pause
%     close all
    if t ==1
        clear all
        close all
        clc
    elseif t ==2
        clear all
        close all
        clc
    end

    beep

end
beep
toc
heat_flux_absorbed
```

Figure 60: Data interpretation code page 14

Appendix B: Averaging infrared temperature values over time

The surface temperature needs to be averaged across time due to the sampling rate of the infrared camera being lower than the DAQ this is done by first getting the temperature gradient in time between the two instances.

$$\frac{\Delta T}{\Delta t} = \frac{\bar{\bar{T}}_{s,h,n+1} - \bar{\bar{T}}_{s,h,n}}{2} \tag{1}$$

This temperature gradient in time, $\frac{\Delta T}{\Delta t}$, is the subtraction of the average surface temperature at the end of the time interval minus the average surface temperature at the start of the time interval divided by 2.

The number of instances the DAQ took a set of measurements between each infrared image is determined by dividing the frequency of the infrared camera with the frequency of the DAQ. This yield the number of increments. Between each measurement.

$$N_{inc} = \frac{f_{inf}}{f_{DAQ}} \tag{2}$$

N_{inc} is the number of increments, f_{inf}, is the frequency of the infrared camera and f_{DAQ} is the frequency of the data acquisition system. This is used to find how much of the temperature gradient had been covered at the point where the next DAQ temperature measurement was taken.

$$\frac{\Delta T}{\Delta t N_{inc}} = \frac{\Delta T}{\Delta \mathrm{t}} \cdot \frac{1}{N_{inc}} \tag{3}$$

The portion of the gradient that had been covered in each increment is determined using equation (3) with $\frac{\Delta T}{\Delta t N_{inc}}$ representing the temperature change in one increment. The temperature at an increment i+1 is the sum of the temperature at the current increment and the change in the temperature for each increment as shown in equation (4).

$$\bar{\bar{T}}_{s,h,n,i+1} = \bar{\bar{T}}_{s,h,n,i} + i \cdot \frac{\Delta T}{\Delta t N_{inc}} \tag{4}$$

Appendix C: Uncertainty propagation

Uncertainty in a measured quantity was due to many different sources depending on the value being measured. Generally, the sources of uncertainty are generalised to be either biased errors or random errors. In this study the biased errors have been minimised and assumed to be zero in many cases.

Random errors in the study lead to an uncertainty in the measurement and cannot be completely nulled. This random uncertainty is represented either as σ which is the relative uncertainty represented with a % or as ϵ which is the absolute error and has the same units as the measurement.

The relative uncertainty is a value that scales with the measured value which is useful when representing quantities that are a function of many parameters, for example heat transfer coefficient. Absolute uncertainty is useful when the uncertainty of a variable is constant and does not scale, for example infrared temperature measurements which have a fixed uncertainty irrespective of the temperatures being measured.

This study had several different variables that had components that were the sum or subtraction of two or more parameters; products or quotient of two or more parameters or a combination of sum, subtraction, product or quotient.

When a variable is a function of two summed or subtracted parameters the relative uncertainties are summed using the root squared sum method. This case requires that the uncertainties used be the absolute uncertainty of parameters.

$$f(x,y) = x + y \tag{5}$$

$$\epsilon_f = \sqrt{\epsilon_x^2 + \epsilon_y^2} \tag{6}$$

Equation (5) shows that the variable, $f(x,y)$, is a function of both x and y and that the two parameters are summed. The absolute uncertainty of the function, ϵ_f, is represented as the root squared sum of the absolute uncertainties, ϵ_x and ϵ_y, as shown in equation (). However, this absolute uncertainty is often not what is of interest requiring the conversion between the absolute and relative uncertainty.

$$\sigma_f = \frac{\epsilon_f}{f(x,y)} \tag{7}$$

In equation (7) the relative uncertainty of the function, σ_f, is calculated from the absolute uncertainty by dividing the absolute uncertainty with the expected value of the function $f(x, y)$. The reported relative uncertainties are for the largest uncertainties.

When a variable is a product of two parameters the uncertainty is not defined using the absolute uncertainties but rather their relative uncertainties. The same method is used as before when combing the uncertainties by taking the root squared sum of the relative uncertainty.

$$f(x, y) = xy \tag{8}$$

$$\sigma_f = \sqrt{\sigma_x^2 + \sigma_y^2} \tag{9}$$

Equation (8) shows that the function f is defined by the product of parameter x and y. The relative uncertainty of f, σ_f, is the root squared sum of the relative uncertainties of both parameters shown in equation (9).

When defining the saturation temperature of FC-72 the temperature is a function of a logarithmic expression. This results in the determining of the uncertainty of the function f with its parameters inside a logarithmic function as shown in equation (10).

$$f(x) = \log(x) \tag{10}$$

$$\sigma_f = \sigma_x \log_{10}(e) \tag{11}$$

In equation (11) the relative uncertainty of the function f is simply the product of the log of e and the relative uncertainty of the parameter. This produces a relative uncertainty for the function.

Often more than one of these methods are required when determining the uncertainty of a variable or parameter. This results in the uncertainty being calculated in several different ways to get the single output uncertainty.

Appendix D: Error propagation

In this appendix the error propagation for various measured and output parameters will be shown. The first section will involve the measured quantities with their minimum and maximum, absolute, and relative uncertainties. The equations from Appendix C will be used extensively in this section and are referred to in each case.

Current and voltage

Current (I) and voltage (U) were measured using MASTECH® MS8239 multimeters which had uncertainties of 1%+10 for the current (mA) and 0.5%+2 digits for the voltage (V). The first portion of the absolute uncertainty ϵ_I was the error due to the 1% of the measured value taken at the reading that would result in the minimum value. The second component of the absolute uncertainty ϵ_I was from the two decimal places of each reading (0.01) and the 10-digit error. The current had a typical reading with two decimal places and ranged from around 43.00 mA to 83.00 mA. The relative uncertainty of current is determined using the total uncertainties from the percentage error and the digits associated error:

$$\sigma_{I,max} = \frac{\epsilon_I}{I} = \frac{(43 \cdot 0.01) + (0.01 * 10)}{43} = \pm 1.23\% \quad (12)$$

$$\sigma_{I,min} = \frac{\epsilon_I}{I} = \frac{(83 \cdot 0.01) + (0.01 * 10)}{83} = \pm 1.12\% \quad (13)$$

The maximum relative uncertainty was calculated to be $\pm$1.23% at 43 mA and the minimum was calculated to be $\pm$1.12% at 83 mA. The minimum absolute uncertainty was $\pm$0.53 mA from the 43 mA reading and the maximum absolute uncertainty was $\pm$0.93 mA from the 83 mA reading.

Voltage readings ranged from 70 V to 135 V with uncertainty calculated as 0.5 of the measured value and 2 digits added of the last decimal place which was tens for the voltage reading. The maximum and minimum relative uncertainties are shown in equation 14 and 15.

$$\sigma_{U,max} = \frac{\epsilon_U}{U} = \frac{(70 \cdot 0.005) + (0.1 * 2)}{70} = \pm 0.79\% \quad (14)$$

$$\sigma_{U,min} = \frac{\epsilon_U}{U} = \frac{(150 \cdot 0.005) + (0.1 * 2)}{150} = \pm 0.63\% \quad (15)$$

The maximum relative uncertainties was ±0.79% from the 70 V reading and the minimum relative uncertainty was ±0.63% from 150 V reading. The absolute uncertainties were ±0.55 V from the 70 V reading and ±0.15V from the 150 V reading.

Thermocouples

Absolute uncertainties from the temperature measurements were determined from the calibration was ± 0.14°C. The temperature of the fluid at the inlet and outlet was fixed for all experiments at 19.5°C at the inlet and 56.25°C at the outlet. The resulting relative uncertainty was ±0.71% at the inlet and ±0.25% at the outlet. The atmospheric temperature measurement had an absolute uncertainty of ± 0.14°C and was approximately 24°C for all experiments with a corresponding relative uncertainty of ± 0.58%.

Infrared Temperature

The infrared camera's maximum absolute uncertainty was that specified by the supplier at ±2°C. Typical surface temperature measurements during two-phase experiments ranged from 40°C to 150°C with corresponding relative uncertainties of ±5% and ±1.3%. The single-phase measured temperatures ranged from 20°C to 70°C with corresponding relative uncertainties of ±10% and ±2.9%.

Channel geometry

The channel's geometry was measured using a Vernier calliper which had an absolute uncertainty of ± 0.02 mm. Typical geometric sizes of the channel were: a width of 5 mm, height of 0.5 mm and heated length of 80 mm. The corresponding relative uncertainties were ± 0.4% for the width, ± 4% for the height and ± 0.025 % for the heated length.

In the rest of this section the relative uncertainty of the calculated outputs are shown.

Heated surface area

The heated area was the product of the heated length (± 0.025 %) and width (± 0.4%) of the channel. This resulted in a relative uncertainty of ±0.4%. Calculated using equation 9 from Appendix C.

Cross-sectional area

The cross-sectional area was the product of the width (± 0.4%) and the height (± 4%) of the channel which had an uncertainty of ±4.02%. Calculated using equation 9 from Appendix C.

Environmental temperature difference

The environmental temperature was the difference in temperature between the heated surface and the environment. The infrared camera's relative uncertainties were between $\pm$ 5% and $\pm$ 1.3% and the absolute uncertainty was $\pm$ 2°C for the two-phase experiments with a maximum of $\pm$10% from the single-phase experiments. The environmental temperature difference had an absolute uncertainty of ± 0.14°C and a relative uncertainty of ± 0.58%. The absolute uncertainty of the environmental temperature difference was calculated using equation 6 and was ± 2.005°C. The relative uncertainty was calculated using equation 9 and was calculated to be between ± 5.03% and ± 1.4% for the two-phase experiments and up to 10.02% in the single-phase experiments.

Absorbed heat

The amount of heat absorbed by the fluid was calculated as an energy balance between the applied heat and the heat lost to the environment. As is shown below:

$$\dot{Q} = \dot{Q}_{ap} - \dot{Q}_{loss} \tag{16}$$

The amount of heat applied ($\dot{Q}_{ap}$) was a function of the voltage and current measurements while the amount of heat lost ($\dot{Q}_{loss}$) was a function of the temperature difference between the heated surface and the environment and correlation from the single-phase testing. Starting with the amount of heat applied, it was calculated using the following formula:

$$\dot{Q}_{ap} = U \cdot I \tag{17}$$

The relative uncertainty of the voltage ranged from $\pm$ 0.76% to $\pm$ 0.63% and the current ranged from $\pm$ 1.23% to $\pm$ 1.12%. The relative uncertainty for the applied heat was calculated using equation 9 and ranged from $\pm$ 1.45% and $\pm$ 1.29%.

The amount of heat lost to the environment was calculated form a power function fitted to experimental single-phase data. The power function had a typical form of:

$$\dot{Q}_{loss} = a(\Delta T)^b \tag{18}$$

"a" and "b" are coefficients, and the environmental temperature difference. Typical coefficient values were 0.0193 for a and 1.2766 for b. The heat loss equation was only used for the two-phase experiment and as a result only the heat loss in the two-phase region were calculated. The relative uncertainties of the environmental temperature in the two-phase region ranged from $\pm$ 5.03% to $\pm$ 1.4%. calculating the relative uncertainty of the heat loss required the use of the following two equations from Dunn [214]:

$$\sigma_{\dot{Q}_{loss}} = a \cdot \left(\sqrt{(b \cdot \sigma_{\Delta T})^2}\right) \tag{19}$$

$$\dot{Q}_{loss} = 0.0193(\Delta T)^{1.2766} \tag{20}$$

The heat loss uncertainty was calculated to range from $\pm$ 0.15% to $\pm$ 0.03%. The R^2 of the fitted curve was at most 0.9788 which a possible error of up to 2.12%. This needs to also be considered and was incorporated using equation 9 to produce an actual relative uncertainty from $\pm$ 2.13% and $\pm$ 2.12%.

The resulting amount of heat absorbed in the two-phase region incorporated relative uncertainties of the amount of heat absorbed ($\pm$ 1.45% and $\pm$ 1.29%) and the amount of heat lost ($\pm$ 2.13% and $\pm$ 2.12%). The relative uncertainty of the amount of heat absorbed was calculated using equation 9 to range from $\pm$ 2.58% to $\pm$ 2.48%.

Heat Flux

The heat flux was calculated using the absorbed heat and the surface area:

$$\dot{q} = \frac{\dot{Q}}{A} \tag{21}$$

The relative uncertainty of the absorbed heated ranged from $\pm$ 2.58% to $\pm$ 2.48% and the heated surface area was fixed at $\pm$ 0.4%. The relative error of the heat flux ranged from $\pm$ 2.6% to 2.5%.

Mass flow rate

The mass flow rate was calculated as follows:

$$\dot{m} = \dot{V}\rho \tag{22}$$

In the equation above the Volumetric flow rate was fixed and specified by the syringe pump which had an uncertainty of 1%. The density was calculated using an equation from the manufacture 3M:

$$\rho = 1700 - 2.61T \tag{23}$$

The mass flow rate was calculated at the inlet and was assumed to be constant throughout the channel. The temperature at the inlet had an uncertainty of $\pm$ 0.71% with a coefficient of 2.61. This meant that uncertainty was determined using the coefficient and the temperature's uncertainty which was calculated to be $\pm$ 1.85%. From these calculations the mass flow rate had a fixed uncertainty of $\pm$ 2.1%.

Single-phase fluid temperature

Single-phase fluid temperature were calculated using the following equation:

$$T_{b,z} = T_{in} + \frac{\dot{q}Wz}{\dot{m}c_p} \tag{24}$$

Where the temperature in each cell was based on the temperature entering the cell and the amount of heat absorbed by the fluid. The amount of heat absorbed by the fluid was based on the absorbed heat flux, distance across which heat was absorbed, the mass flow rate and the heat capacity of FC-72. The heat capacity was calculated using an equation form 3M:

$$c_{P,l} = 1010 + 1.554T \tag{25}$$

The relative uncertainty of the inlet temperature conditions was $\pm$ 0.71% with the specific heat's relative uncertainty calculated to be $\pm$ 1.1%.

The uncertainty of the amount of heat absorbed in each control volume was based on the relative uncertainty of each of the 4 components and calculated using an extended form of equation 9. The uncertainties for the heat flux ranged from $\pm$ 2.6% to 2.5%, for the width was fixed at $\pm$ 0.4% and for the mass flow rate was $\pm$ 2.1%. The relative uncertainty of the amount of heat absorbed was between $\pm$ 3.54% and $\pm$ 3.47%.

The temperature at the inlet to the two-phase region was based on the inlet thermocouples measurements which were an absolute uncertainty of $\pm$ 0.14°C and relative uncertainty of $\pm$ 0.71%. This relative uncertainty of the local fluid temperature in the single-phase region was thus based on amount of heat absorbed up to that point and the inlet fluid temperature measured by the inlet thermocouple. This resulted in a local fluid temperature relative uncertainty between $\pm$ 3.6% and $\pm$ 3.54%.

Two-phase fluid temperature

The temperature of the fluid in the two-phase region was the same as that measured at the outlet. This meant an absolute uncertainty of $\pm$ 0.14°C and a relative uncertainty at the saturation temperature 56.25°C of $\pm$ 0.2%.

Interfacial wall to fluid temperature difference

The difference in temperature between the fluid was calculated as follows:

$$\Delta T = T_{s,z} - T_z \tag{26}$$

and the heated wall had different uncertainties in the single-phase and two-phase region. The wall temperature uncertainty ranged from $\pm$ 5% to $\pm$ 1.3%. The fluids temperature uncertainty in the single-phase region was between $\pm$ 3.6% and $\pm$ 3.54% and fixed at $\pm$ 0.25% in the two-phase region.

The interfacial temperature difference uncertainty in the single-phase region ranged from $\pm$ 6.2% to 3.8%. In the two-phase region the interfacial temperature difference ranged from $\pm$ 5% to 1.32%.

Heat transfer coefficient

The heat transfer coefficient was calculated as follows:

$$\alpha_z = \frac{\dot{q}_z}{(T_{s,z} - T_z)} \tag{27}$$

The relative uncertainty of the absorbed heat flux ranged from $\pm$ 2.6% to 2.5% and the temperature difference between the heated wall the fluid's temperature ranged from $\pm$ 6.2% to 1.32%. The resulting uncertainty of the heat transfer coefficient was from between $\pm$ 6.7% to $\pm$ 2.8%.

Vapour quality

The local vapour quality at the inlet was calculated using the following equation:

$$\chi_{z=0} = -\frac{\dot{m}c_p(T_{sat} - T_{in})}{\dot{m}h_{fg}} \tag{28}$$

Uncertainties of the specific heat was fixed at $\pm$ 1.1%, the saturation temperature was $\pm$ 0.25% and the inlet temperature was 0.71%. The uncertainty was calculated using equation 6 and 9. The resulting uncertainty of the inlet vapour quality was 1.33%. The local vapour quality was measured using the following equation

$$\chi_z = \chi_{z-\Delta l} + \frac{\dot{Q}_{net,z}}{\dot{m}h_{fg}} \tag{29}$$

In this equation the amount of heat absorbed, and mass flow rate are used to determine the amount of heat absorbed up to that point. The relative uncertainty of the absorbed heat ranged from $\pm$ 1.45% and $\pm$ 1.29%. Using an expanded form of equation 9 the resulting uncertainty of the local vapour quality ranged from $\pm$ 2.25% to 2.15%.

Mass flux

Mass flux was calculated using the following equation:

$$\dot{G} = \dot{m}/A_c \tag{30}$$

The uncertainty of the mass flow rate was$\pm$ 2.1% and the cross-sectional area was $\pm$ 4.02%. The resulting relative uncertainty was 4.5%